1985

Image processing of hydrogen bubble flow visualization for determination of turbulence statistics and bursting characteristics /

Lih-Ju Lu
Lehigh University

IMAGE PROCESSING OF HYDROGEN BUBBLE FLOW VISUALIZATION FOR DETERMINATON OF TURBULENCE STATISTICS AND BURSTING CHARACTERISTICS

by

LIH-JU LU

A Thesis

Presented to the Graduate Committee

of Lehigh University

In Candidacy for the Degree of

Master of Science

in

Mechanical Engineering

This thesis is accepted and approved in partial fulfillment of the requirements for the Degree of Master of Science.

8 May 1985
(date)

Charles R. Smith
professor in charge

F. Erdogan
chairman of department

ACKNOWLEDGEMENTS

My association with Dr. C.R. Smith has been very rewarding in terms of education content. Throughout this time, Dr. C.R. Smith has advised and assisted me in this research effort. I am grateful to Dr. Smith for his patience and extend to him my sincere thanks.

Many thanks go to all the members of the Mechanical Engineering and Mechanics Department who have helped me in many ways.

Finanical support from the U.S. Air Force Office of Scientific Reserach is gratefully acknowleged.

I would like to thank my family and friends for their support and encouragement during times when I had been discouraged. Words alone cannot express my appreciation.

TABLE OF CONTENTS

(Table of Contents - cont.)

LIST OF FIGURES

(List of Figures - cont.)

(List of Figures - cont.)

(List of Figures - cont.)

(List of Figures - cont.)

NOMENCLATURE

C_d : Drag coefficent of Cylinder

Cf : Skin friction coefficient = $\sqrt{\tau_w / 0.5 \rho U_\infty^2}$

d : Diameter of the hydrogen bubble wire

f : Bursting frequency

f^+ : Nondimensional bursting frequency = $\nu / U_\tau^2 t = f\nu / U_\tau^2$

k : $Var(t,T)/Urms^2$

Re_d : Reynolds number based on diameter = dU_∞ / ν

Re_x : Reynolds number based on streamwise distance from leading edge of plate = XU_∞ / ν

Re_θ : Reynolds number based on momentum thickness = $\theta U_\infty / \nu$

t : time (sec)

Δt : time interval (sec)

t^+ : Nondimensional time = tU_τ^2 / ν

u : Instantaneous value of velocity in streamwise direction

u' : Instantaneous value of velocity fluctuation in the streamwise direction

$\overline{U}$: Mean velocity in streamwise direction

$\overline{U}^+$: Nondimensional Mean velocity in streamwise direction

Urms: Root mean-square of the streamwise velocity fluctuation

U_∞ : Free stream velocity

U_τ : Friction velocity = $\sqrt{\tau_w / \rho}$

v : Normal velocity

w : Spanwise velocity

X : Streamwise coordinate

X^+ : Nondimensional streamwise coordinate = XU_τ/ν

Y : Normal coordinate

Y^+ : Nondimensional normal coordinate = YU_τ/ν

Greek

δ : Boundary layer thickness

δ^* : Displacement thickness

θ : Momentum thickness

ν : Kinematic viscosity

τ_w : Wall shear stress

ABSTRACT

Quantitative and qualitative analyses of flow over a flat plate in turbulent boundary layer are studied by applying the image-processing methods to flow visualization picturres. A technique of image-processing is described which employs automated analysis of hydrogen-bubble flow visualization pictures to identify the locations of hydrogen-bubble time-lines, from which are established local, instantaneous velocity profile information. Hydrogen bubble flow visualization sequences are recorded using a high-speed video system and then digitized, stored, and evaluated by a VAX 11/780 computer. Employing special smoothing and gradient detection algorithms, individual bubble-lines are computer identified, which allows local velocity profiles to be constructed using time-of-flight techniques. It is demonstrated how this technique may be used to (1) determine local velocity behavior as a function of postion and time, (2) evaluate time-averaged turbulence properties, (3) correlate probe-type turbulent burst detection techniques with the corresponding visualization data, and (4) relate visually detected side-view bursting behavior with instantaneous turbulence statistics.

1. INTRODUCTION

1.1 General Introduction

Through the combined use of computer and video systems, recent years have seen increasing work on image-processing techniques for applications in biology, physics, and chemistry etc.. The objective of image-processing techniques, encompassing computer science and mathematics, is to enhance the visual appearance of an image or covert the image to a form which is suitable for machine analysis. In the present study, a technique of image-processing hydrogen-bubble flow visualization is established and employed for the study of the behavior of turbulent boundary layers.

Past investigations of turbulent flow have been carried out using conventional forms of flow visualization, hot-wire anemometry, laser-doppler anemometry, or occasionally a combination of two or more of these methods. However, it has been recently established that turbulence seems to be composed of a collection of flow "structures" which create the chaotic appearance of turbulence. A particular need in the study of these complicated flow structures is the determination of the connection between a visualized "structure" and quantitative measurements. This determination necessitates the measurement of instantaneous flow-field behavior, which has generally proven very difficult. Normally, a rake of probes has been used in a flow visualized with an appropriate medium, and attempts

have been made to correlate the multiple-probe measurements with the visualized flow. Dye injection, tracer particles, smoke injection, smoke wires, and hydrogen bubbles are just some of the flow visualization techniques which have been used. However, the connection between the visual image and the probe data is still somewhat subjective (since the location of the probes in the plane of the image is not clearly defined). In addition, the insertion of multiple probes in a flow has a potentially disturbing effect on the flow field being measured, limiting the number of probes which can be used.

1.1.1 Quantitative Flow Visualization

Potentially, the use of appropriate visualizaton mediums and techniques can provide quantitative information that is vastly more extensive than that available from even large arrays of anemometry probes. In the past, the extraction of quantitative information from flow visualization pictures was done manually, such that data were very laborious to obtain or were of limited accuracy, since they were generally based on subjective evaluation of the location of the visualization medium within a picture (see Kim et al. 1971, Grass 1971, and the semi-automated computer technique of Smith and Paxson 1983). With the continued development of computer image-processing techniques, it is now feasible to obtain information by a quantitative treatment of visualization pictures.

Recently, laser-pulse techniques and tracer techniques, which utilize small particles (perspex, air bubbles, hydrogen bubbles, coloured dye, or fluorescent dye for hydraulic experiments, and smoke or sprays for aerodynamic experiments) have been used in conjunction with image-processing techniques to allow quantitative analysis of visualized flow behavior. Once a visual picture has been obtained, it is digitized into a computer system for image-processing and quantitative analysis. Identification of contours or particle locations within the picture are determined by applying various detection methods such as image enhancement, edge detection algorithms, etc.. Using the resultant quantitative data, certain physical properties can be established, analyzed, and recreated, often using three-dimensional display techniques. For instance, Balint et al. (1983) have used a laser and a set of rotating mirrors to visualize a turbulent jet seeded with particles and smoke. By using particle contour analysis, the mean concentration field, RMS field, and skewness field of the free jet flow were reconstructed in a three-dimensional, gray-level display.

Similar quantitative visualization studies of jet sprays have been performed by Shimizu et al. (1983), where a pulse laser was employed for the simultaneous recording of both a hologram and a forward-backward light-scattering photograph for analysis of the droplet size and volume density distribuation of jet sprays. Another image-processing study of a turbulent jet by Brandt (1983),

employed a laser sheet to illuminate a fluorescent dye; an edge detection technique based on discrimination of the spatial derivative between pixels of the image was then used to develop an isometric projection of the temporal derivative of the evolving turbulent jet.

A study of turbulent boundary layer structure by Wallace et al. (1983) employed smoke as the visualization medium, with illumination generated using a laser-sheet/rotating-mirror system. Digital image enhancement was employed in this study to accentuate the various aspects of the flow structure. A more complicated application of particle tracing using image-processing techniques in a three-dimensional mean flow has been developed by Chang and Tatterson (1983) by use of two-view recording of the discharge fluid flow in an agitated vessels. They utilized the parallel information in the two-view simltaneous pictures to recreate details of the three-dimensional flow regime.

Thus, the use of image-processing of a visualized flow field can be used to develop flow-field property data which is either difficult or often impossible to measure using conventional means. The present technique explores the potential application of digital image processing and appropriate software to provide a rather accurate and efficient procedure for quantitative analysis and invesigation of a turbulent flow field.

The quantiative analysis of flow visualization pictures using the hydrogen bubble technique has been performed by Kim et al. (1971), Grass (1971), Cornelius (1977), and Smith and Paxson (1983). Kim et al. and Grass manually extracted data from flow visualization pictures by direct measurement. However, these methods are of limited accuracy and result in very slow data acquisition. The first application of an automated image-processing technique to such visualization data was done by Cornelius et al. (1977). They employed a small computer integrated with a digitizer to convert the image to a digital array. They then applied a threshold cut-off method to establish position profiles for the hydrogen bubble lines; differencing these identified profiles yielded time-of-flight velocities. The Cornelius study revealed the potential of automated image-processing for successfully evaluating velocity data from hydrogen bubble time-line visualization. The results of the Cornelius study indicated a good comparsion of mean velocity and turbuence instensity profiles with comparable profiles measured with hot-film anemometry. However, the Cornelius study did not consider corrections for the flow defect behind the hydrogen bubble wire, and did not have the capacity to extensively explore the quantitative and qualitative implications of the data obtained.

Smith and Paxson (1983) developed a semi-automatied computer technique for evaluation of dual-view hydrogen bubble pictures which allowed the reconstruction of the three-dimensional time-dependent

motion of single bubble time-lines. They used a data tablet to manually digitize the local time-line location in two orthogonal perspective views from a time sequence of videographic prints; the digitized data was then computer reconstructed to yield the three-dimensional location of the time-line. Using the time-line data, time-of-flight techniques allowed the determination of quasi-instantaneous u and v Lagrangian velocity pairs, providing a new method for studying regional flow behavior.

1.2 The Flow Structure and Bursting Phenomena of Turbulent Boundary Layers

1.2.1 Qualitative Flow Visualization

The first studies of the flow structure in the wall region were done visually in such classic studies as Kline et al. (1967), Corino and Brodkey (1969), and Kim et al. (1971). These studies indicated that a turbulence sustaining process termed "bursting" occurs near the wall-fluid interface; this process involves some kind of interaction between a "low-speed streak" flow structure, occurring very near the wall, and the outer region of the boundary layer. This process appears as a gradual streak "lift-up" and subsequent oscillation, followed by a sudden break-down or "bursting" and ejection of the low-speed fluid from the surface.

Kline et al. (1967) and Kim et al. (1971) have commented on the

striking violence of the bursting process. Their observations suggest that streamwise vorticity present near the surface causes the low-speed streak to lift-up and move away from wall until a critical point is reached where a local instability develops. This instability evolves into a streak oscillation, with the oscillating streak then breaking-up and ejecting from the surface region. Kline et al. speculate that this bursting process is the dominant process of momentum transfer between the inner and outer region of turbulent boundary layers. Kim et al. (1971) demonstrated that the turbulence production process adjacent to a solid surface is a quasi-periodic phenomenon which results in the short, energetic production of turbulent energy during bursting.

Corino and Brodkey (1969) suggested that bursts are somehow related to the pertubation of a region of decelerated flow near the wall by a passing disturbance in the outerflow field. They observed a sequence of coherent events, consisting of an ejection of fluid from the decelerated region in conjunction with a sweeping motion, with this process repeating randomly in space and time. Their results indicate that the angle of fluid ejection during break-up or bursting varies between 1.5^{o} and 21^{o} with an average of 8.5^{o}, and the development of maximum turbulence production occurs in the region of $5 < Y^{+} < 15$. They further suggest that the most of the characterstic ejections of wall region fluid develop in the region $0 < Y^{+} < 30$.

The work of Offen and Kline (1975) suggests that the instability of a low-speed streak lift-up develops due to an inflection of the local velocity profile. Such an inflectional profile, developing along the interface between a decelerated streak and high-speed wall region, is speculated to be the result of a local adverse pressure gradient, which causes the streaks to locally decelerate and lift-up.

A model of hairpin vortex (i.e. horseshose vortex or U-shaped loop) development and stretching has been described and suggested by by several researchers as a flow structure developing during the development of bursting behavior. Hinze (1975) suggests that hairpin vortices are generated due to a breakdown caused by a local adverse pressure gradient created at the interface between high-speed outer flow and low-speed inner layers. The breakdown generates an inflectional profile that is suggested by Smith (1984) to result in a series of vortex roll-ups leading to the formation of a sequence of nested hairpin vortices. Recently, Acarlar and Smith (1984) have synthesized a model of the turbulence production cycle which is intimately related to hairpin vortex formation (see figure 1.1). They suggest that a local deceleration creates an inflectional profile at the interface between a decelerated streak and high-speed wall-region fluid (also suggested by Offen and Kline 1975). The strong inflection develops a local instability which grows by a process of three-dimensional vorticity concentration and

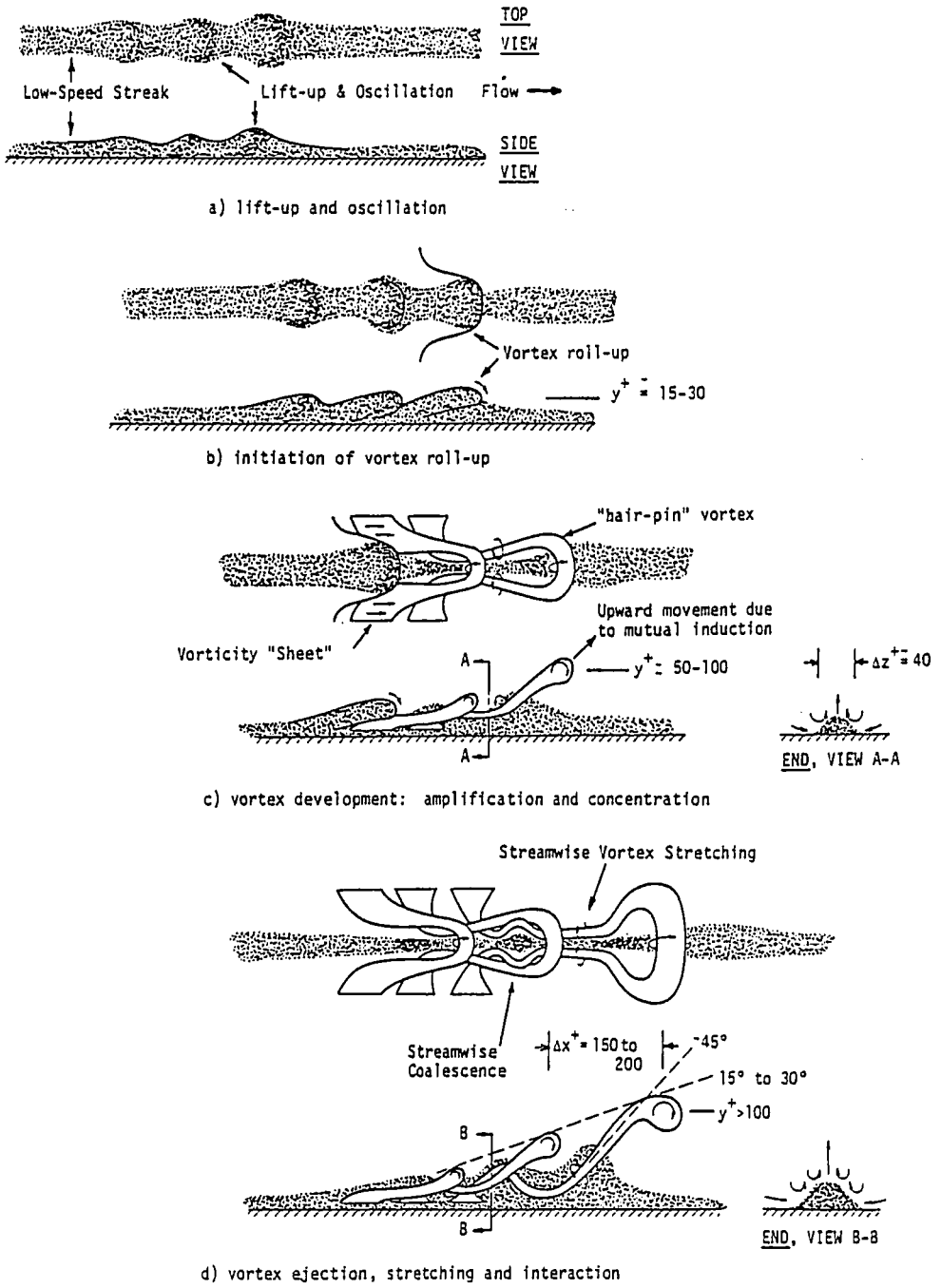

Figure 1.1. Illustration of the breakdown and formation of hair-pin vortices during a streak "bursting" process. Low-speed "streak" regions indicated by shading.

stretching, resulting in a vortex roll-up over the top and sides of the streak. In their model, they suggest the development of secondary vortices which result from the local pressure gradients and lift-up effects caused by the heads and stretched legs of the original hairpin vortices. Ultimately, it is suggested that the initial and secondary hairpins undergo substantial three-dimensional interaction and agglomeration which result in more complex and chaotic structures which undergo rapid ejection away from the wall (i.e. which is interpreted as the bursting behavior).

1.2.2 Quantitative analysis of hot-film measurements

In an attempt to quantify the characteristics of the turbulent bursting process, several investigators have attempted to develop techniques which allow the detection of bursting behavior via probe velocity measurements. Rao et al. (1971) employed a threshold detection technique applied to band-pass-filtered hot-wire signals to determine the frequency of occurrence of large-scale velocity excursions; these excursions were assumed to be associated with the turbulent "bursts". Their quantitative results of $U_\tau^2 T/\nu = 0.65 Re_\theta^{0.73}$ and $U_\infty T/\delta^* = 32$ indicated that the mean frequency ($f^+ = \nu/U_\tau^2 T$) of the burst-type velocity excursions scaled with outer flow variables. Similar results of $U_\tau^2 T/\nu = 0.65 Re_\theta^{0.75}$ and $U_\infty T/\delta = 5$ were obtained by Laufer and Narayanan (1971), indicating that the mean frequency of occurrence is approximately equal to the frequency of passage of the bulges on the outer interface between turbulent

and non-turbulent fluid.

The variable-interval time-average (VITA) technique, developed by Blackwelder and Kaplan (1972), attempts to determine the bursting frequency using a variable averaging interval (T) and threshold (k) (see equation (10) of section 3.3). For this technique, the burst event is defined by the amplitude of the non-dimensional variance (see caption of figure 3.9(a)) over a specified threshold level. This burst detection method, termed the VITA technique, was further developed by Blackwelder and Kaplan (1976), using probe rake measurements which allow simultaneous examination of the instantaneous velocity at several locations. Based on the VITA technique Blackwelder and Kaplan (1976) suggest that the non-dimensional burst frequency ($f\nu/U_\tau^2$) is approximately 0.13 (using a threshold of k = 1.2 with a non-dimensional time interval of $TU_\tau^2/\nu = 10$) near the wall ($Y^+ < 100$), but appears to increase in the outer regions of the boundary layer.

Extensions of the VITA technique by Johansson and Alfredsson (1982) treat accelerating and decelerating burst events separately, yielding different characteristic results, particularly for low detection thresholds. The ensemble-averaged behavior they detect with the VITA technique is similar for all Reynolds numbers studied (Re_h = 13800, 34600 and 48900, and $T^+ = 10$), and results of the skewness and flatness factors also appear quite similar as well.

Blackwelder and Haritonidis (1983) have concluded that the bursting frequency scales with the wall parameters, and is independent of Reynolds number. The near-wall bursting frequency, $f^+ = f\nu/U_\tau^2$, was found to be approximately constant at 0.0035 over the Reynolds number range examined ($10^3 < Re_\theta < 10^4$). They also suggest that the bursting phenomenon is universal for boundary layers, pipes, and channel flow.

1.3 Digital Image Processing

1.3.1 Basic Concept of Image Processing

Basically, digital image processing utilizes two special input/output devices, an image digitizer and an image display device, in conjunction with a computer to allow numerical processing of images. Before it can be processed, the image must be converted to a numerical array within the computer memory. This conversion process is called digitization. During digitizing, the image is devided into an array of small regions (i.e. picture elements) or pixels. At each pixel location, the image brightness is sampled and quantized by the digitizer. The digitizer generates an integer at each pixel location representing the intensity (brightness) of the image at that point. When this has been done for all pixels, the image is represented by a rectangular array of integers stored within the computer memory. Each pixel has an integer value (i.e. a gray level) and a location (or address). This array of digital data

can then be subjected to computer processing and analysis.

1.3.2 Linear Filtering or Smoothing for Image Enhancement

Filtering is a technique of modifying image gray levels to enhance the appearence of objects. The technique of convolution filtering or smoothing was applied in the present study to remove picture noise and make the detection of edges much more accurate. Figure 1.2 illustrates the use of convolution for smoothing a noisy function f(x). A rectangular pulse g(x) is the impulse reponse of the smoothing filter. As the convolution proceeds, the rectangular pulse moves from left to right, producing h(x), which is a local average f(x) over a unit width interval at every point. In other words, for a certain point x', the function f(x') is replaced by the summation of f(x)*g(x) for the range $x'-1/2 < x < x'+1/2$. The process of local averaging has the effect of suppressing high-frequency variations while preserving the basic shape of the input function. This application is typical of the use of a filter with a unit positive impulse response to smooth noisy data.

1.3.3 Edge Detection

The boundaries of objects in an image tend to show up as intensity discontinuities. From an image processing point of view, the critical aspect of edge detection is how one designs an edge operator to detect the boundaries of the object. Several mathematical operators for edge detection have been developed to

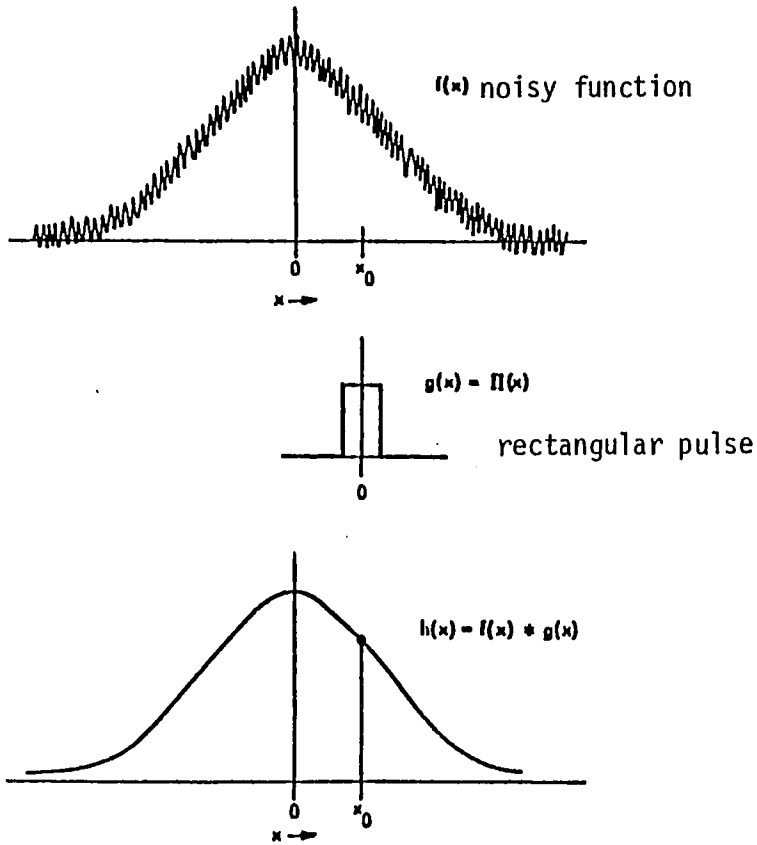

Figure 1.2: Smoothing a noisy function

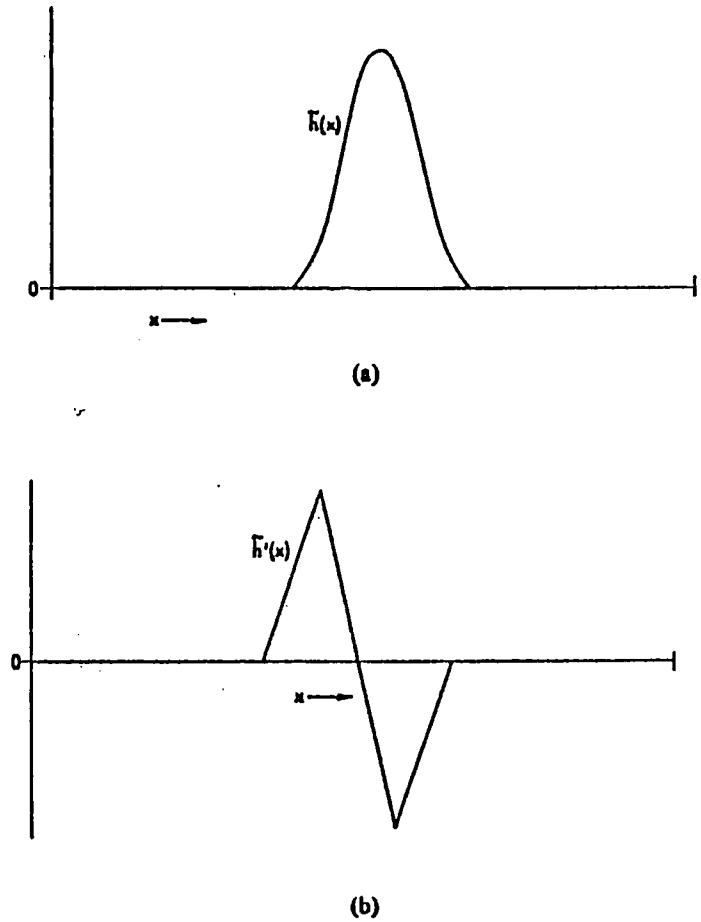

Figure 1.3: (a) Impulse response $\tilde{h}(x)$
(b) Derivative of $\tilde{h}(x)$.

search for the presence of a local edge in an image (see Rosenfeld and Kak 1976, Hall 1979, Ballard and Brown 1982, or other image-processing references). In the present study, a derivative/zero-crossing edge detection procedure has been used to locate the contours of hydrogen bubble-lines. The bubble intensity distribution can be represented as a series of impulse responses (because the hydrogen bubbles are generated a periodic sequence of pulses). After filtering out high-frequency noise, the distribution is similar to that shown in figure 1.3(a). The first derivative ($\tilde{h}'(x)$) of the impulse distribution $\tilde{h}(x)$ (see figures 1.3(a) and (b)), is used to locate the point of maximun intensity, which is the point at which the derivative, $\tilde{h}'(x)$, crosses the zero axis. Using digital convolution allows this zero-crossing edge-detection procedure to be executed very efficiently.

1.4 Present Study

The evaluation of the effectiveness of a burst detection scheme for detection of the classic, visually identified burst sequence of Kim et al. (1971) requires that one be able to directly correlate the output of the velocity-based detection scheme with visually detected burst events. To provide this capability, the present study applies state-of-the-art digital image-processing techniques to evaluate hydrogen-bubble time-line visualization as employed previously by Schraub et al. (1965), Kline et al. (1967), Kim et al. (1971), Grass (1971), Cornelius (1977), etc.. The use of image

processing methods allows the detailed determination and examination of the quantitative statistics and characteristics of turbulent boundary layer flows. The digital data obtained from such visualization images are subject to visual irregularities, and the use of image-processing methods described in the previous section allows the accurate extraction of velocity data from the bubble pictures. Digitization and processing of the video images, in conjunction with image operation techniques (such as linear filtering and an edge detection algorithm), can yield quantitative results that are the equivalent to having instantaneous velocity data simultaneously over a spatial region. The present technique provides a mechanism both for determination of time-averaged turbulence properties from visual data and for correlation of both visual and probe-type burst detection schemes. Numerical manipulation of the initial velocity profile data can then yield further information on the local distribution, turbulence intensity, skewness, flatness, first and second derivatives of velocity, VITA, and local acceleation; this information can then be directly correlated with visually detected bursting behavior and associated with the types of visually observed coherent structures within the flowfield.

2. EXPERIMENTAL APPARATUS and DATA REDUCTION METHODS

2.1 Introduction

Flow visualization experiments were performed and video tape recorded in the open water channel flow facility in the Fluid Dynamics Reserach Laboratory of Lehigh University, using the hydrogen-bubble technique to generate time-line visualization of turbulent boundary layer behavior. To determine quantitative velocity profile data from the hydrogen bubble time-line patterns, individual gray-level video frames are converted to digital intensity arrays using a Colorado Video model 270A video digitizer which is interfaced directly between a video recorder and a VAX 11/780 computer. The application of image processing techniques, including numerical filtering and smoothing of the images, allows the determination of local velocity behavior by time-of-flight techniques.

2.2 Experimental Apparatus

2.2.1 Test Channel and Plate

The flow facility used in the present study is shown in figure 2.1 and 2.2; the details of the facility are described by Metzler (1980) and Cerra (1983). The facility is a free-surface, plexiglass water channel with a 5 m working section, 0.9 m wide by 0.36 m deep. The test surface was a 2.5 m plexiglass flat plate, 6.35 mm thick

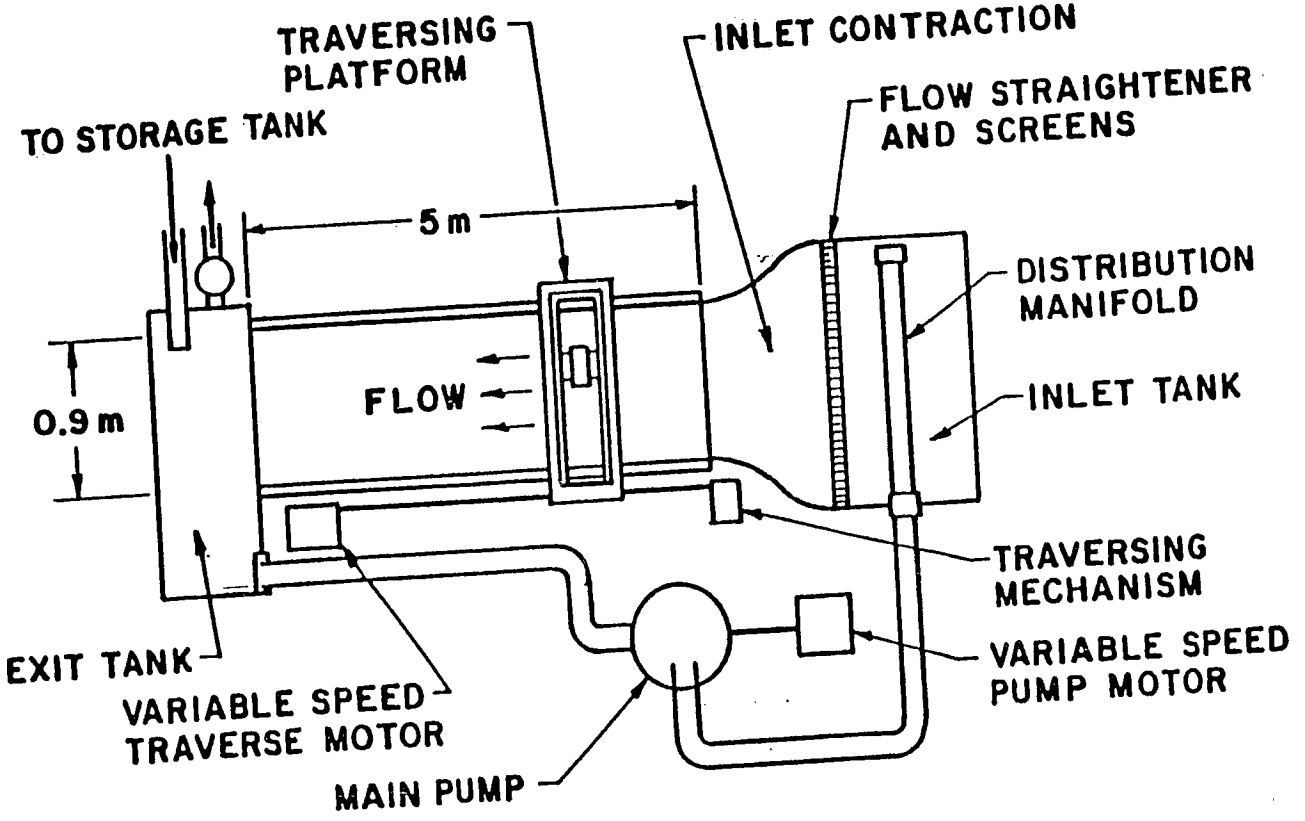

Figure 2.1. Schematic representation of Lehigh University free-surface water channel.

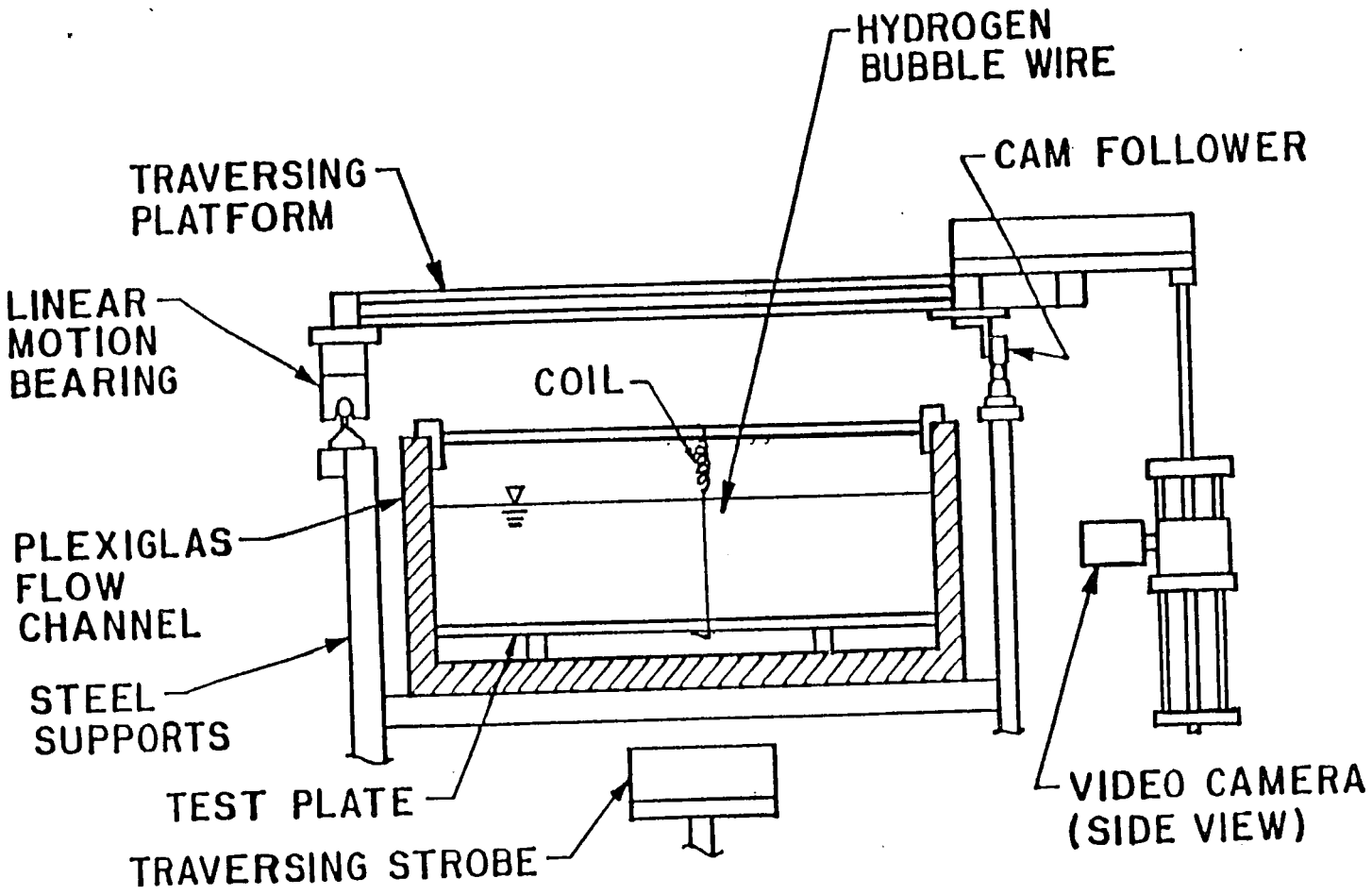

Figure 2.2. End-view schematic representation of camera and lighting positions as viewed from upstream.

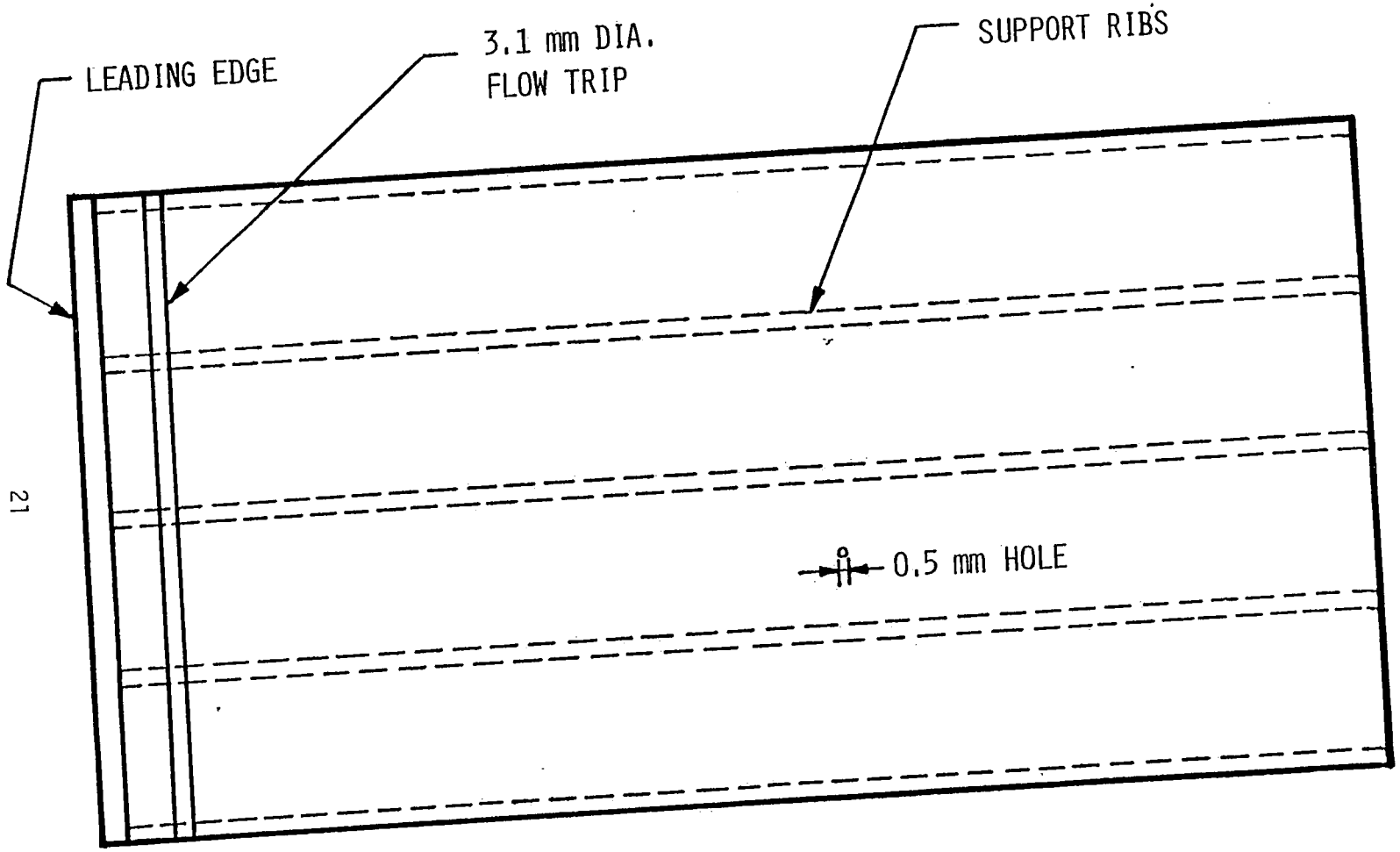

Figure 2.3. Schematic diagram of test plate.

with a 6:1 half-ellipse leading edge, located 10 cm above the channel floor (see figure 2.3). To assure a consistent transition location, a trip constructed of 5 rows of staged polystyrene beads (3 mm to 2 mm in diameter) was located 5 cm from the leading edge. See Johansen and Smith (1983) for details of the trip construction and flow verification.

2.2.2 Hydrogen Bubble Technique

Flow visualization of the turbulent boundary layer was done using the hydrogen-bubble method as described by Clutter et al. (1961) and Schraub et al. (1965). A 0.02 mm diameter platinum wire was oriented normal to the plate and passed through a 0.5 mm hole in the plate which was sealed on the opposing side. The other end of wire was soldered to a coiled copper wire which acted as both a conductor for the bubble-wire circuit and as a tension agent to keep the wire taut. This arrangement allowed the bubble-wire to visualize the entire boundary layer all the way to the surface of the plate. The platinum wire served as the cathode in the bubble-wire circuit; a 0.6 cm diameter graphite rod, located downstream of the wire, served as the anode. The bubbles generated by the wire are of the order of one-half the wire diameter, which renders the buoyancy effects negligible over the region of interest (see Schraub et al. 1965). A specially designed bubble-pulse generator is used to generate hydrogen bubble time-lines (see Metzler 1980). The bubble-pulse generator can provide controlled square-wave voltage pulses at

frequencies ranging from 0.2 to 340 Hz. For the present study, bubble lines were produced at a frequency of 30 Hz, with their generation phase-locked to the framing rate of the video viewing system using a special synchronization circuit in the pulse generator. An eletrolyte of sodium sulfate (0.15 g Na_2SO_3 / liter of water) was added to the channel water to enhance bubble generation. This results in the production of denser bubble lines, which provide better clarity and contrast for the visual data.

2.2.3 Video System

The hydrogen bubble time-lines were viewed and recorded by using an INSTAR high-speed video viewing and recording system manufactured by the Video Logic Corporation (see Smith 1982). The video system incorportes synchronized strobe lights to provide 120 frames/sec, with an effective shutter speed time of 10^{-5} sec. This short exposure time effectively freezes the bubble-line pattern such that high-contrast sequences of discrete pictures may be obtained. This particular video system produces pictures using a raster of 250 horizontal scan lines in direct overlay format.

In the present study, the video camera was mounted as shown in figure 2.2, providing side-views of the vertical hydrogen bubble-wire. The output from the camera can be viewed on-line with the high-resolution TV monitor and simultaneously recorded on a one-inch video tape recorder. Once a visualization sequence is recorded, it

may be replayed in real-time, flicker-free slow motion (forward or reverse), or in sequential, single-frame stop action for detailed data analysis. Individual stop-action frames can be taken directly from the video screen using conventional photography or via a videographic copier which interfaces with the video recorder.

2.3 Image-Processing

2.3.1 Digitization system

To determine quantitative velocity profile data from the hydrogen bubble time-line patterns, image processing techniques have been employed via a digitization system, shown schemstically in figure 2.4. The system converts individual video frames to 215*165 digital intensity arrays using a Colorado Video model 270A video digitizer (see figure 2.5) which is interfaced directly between the video recorder and a VAX 11/780 computer by means of four input-output cables.

The CVI Model 270A Video Digitizer provides the capability of extracting data in digital form from standard video signals. Independent X and Y digital inputs allow complete control over the location of the picture elements that are to be encoded. The digitizer also incorporates a video display output which allows the user to directly observe the scene being processed and to monitor the encoding process on a standard television monitor. Location of

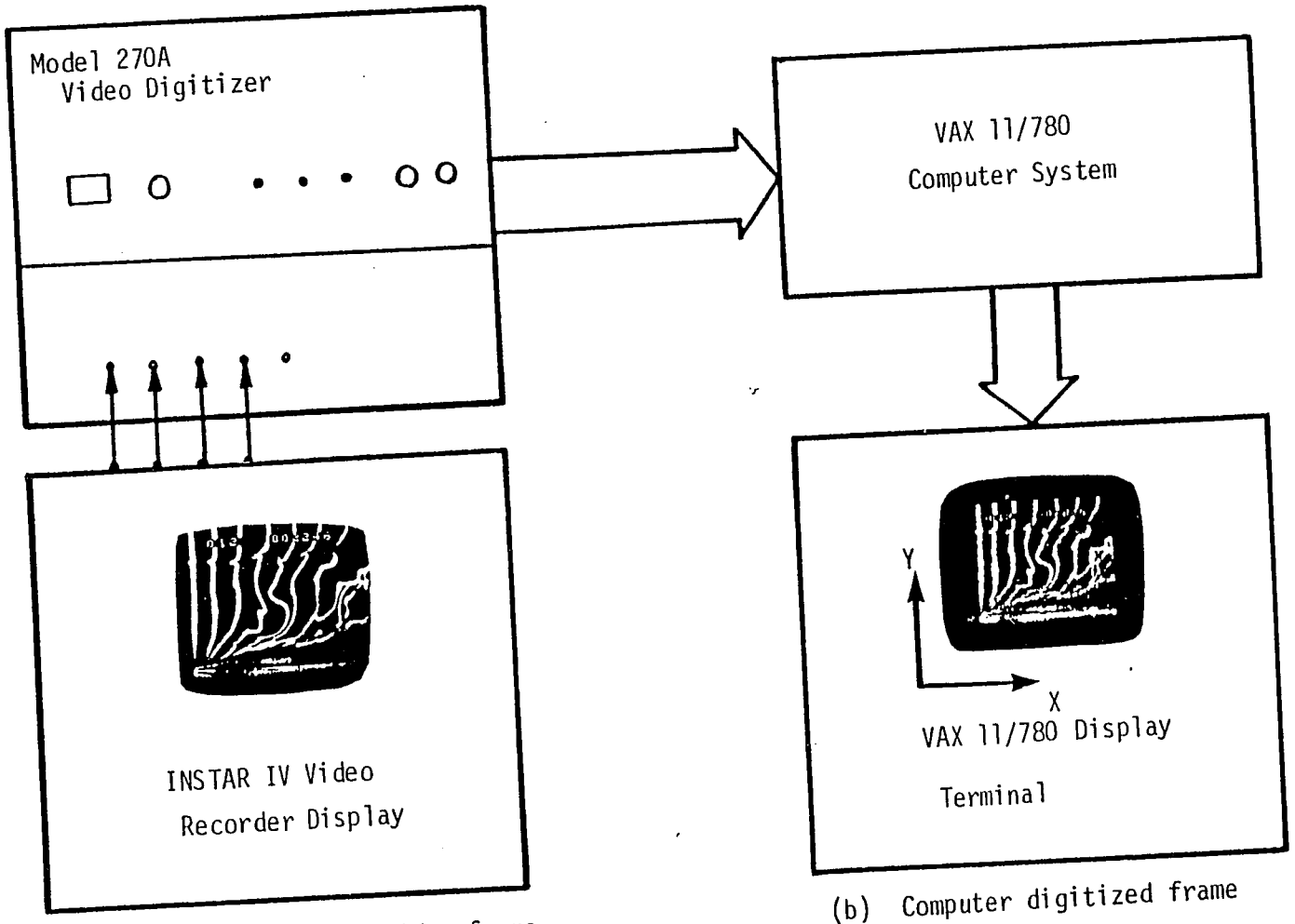

Figure 2.4. Schematic diagram of digitization process.

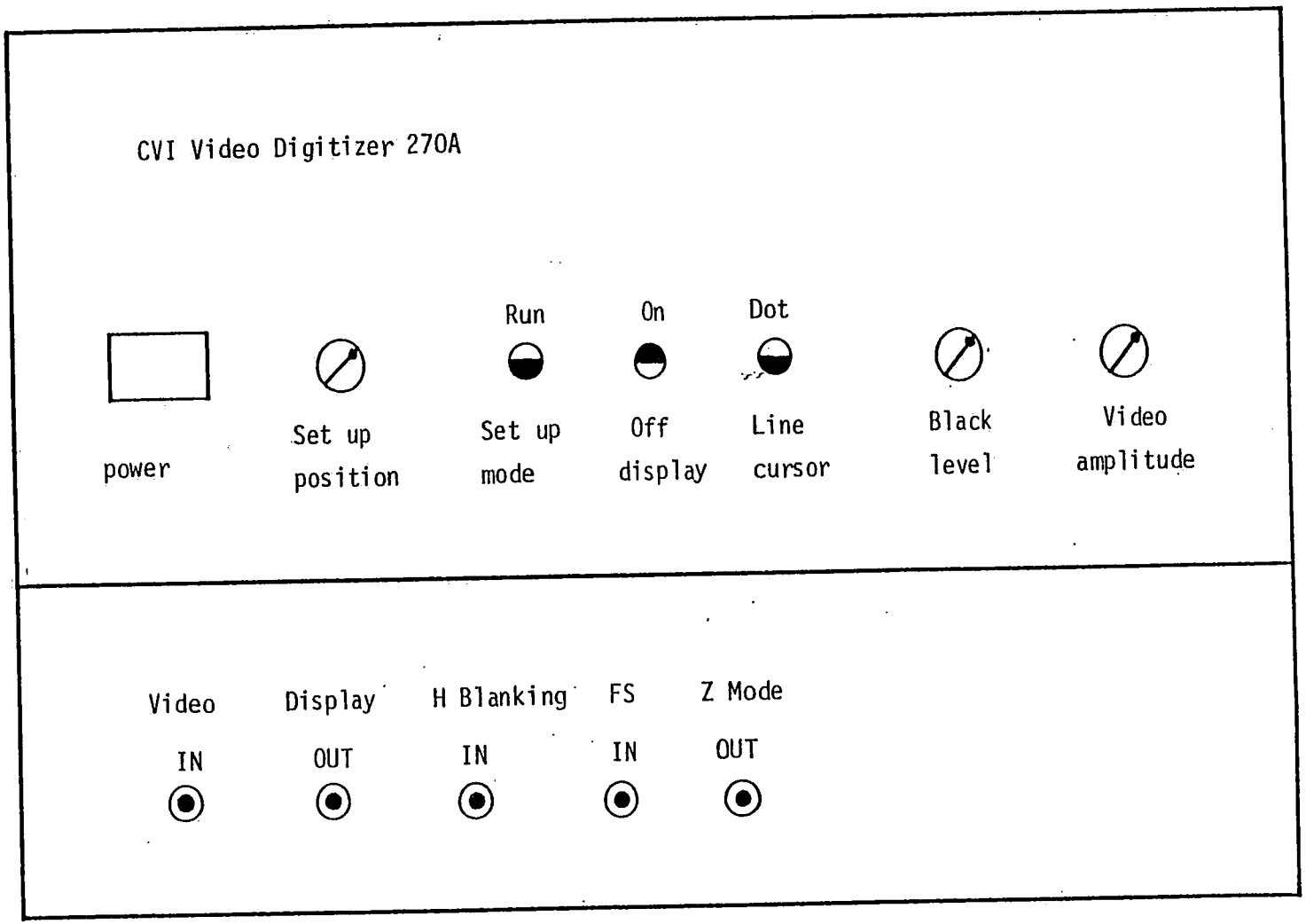

Figure 2.5. Schematic of front panel of CVI model 270A video digitizer.

the point being encoded is indicated on the display monitor by a vertical cursor; a waveform indicating the brightness profile along the cursor location is displayed at the side of the monitor screen. This feature, together with a set-up mode, allows quick and accurate setting of the grayscale levels without use of auxiliary equipment.

2.3.2 Digitization Procedure

To set-up for the video scene digitization process, four coaxial data lines from the video recorder (video signal, the monitor video input, a field select signal, and a blanking signal) are connected to the video digitizer; the digitizer is hard wired to the VAX 11/780 computer directly through a DEC unibus system. With the video in the stop-frame mode on a particular scene of interest, the digitizer is switched to the "set-up" mode, and the brightness level and the gray-scale levels are adjusted to set the range of digital values to cover the the gray-level extremes of the picture or picture sequence to be digitized; the digitizer digitizes each picture over a range of 256 gray levels.

Once set-up is completed, the digitizer is switched to the "run" mode, the frame to be digitized is fixed via a stop-action button on the video system, and the picture is digitized via a computer prompting of the digitizer (see Appendix A for the detailed procedure). A special computer prompting and data storage program written in a MACRO-machine language allows the computer to

communicate with and prompt the digitizer during picture digitization.

Each picture is converted to a 215*165 digital intensity array and stored to disk by the computer. The total time required to digitize a video frame, assign a file-name, off-load the file to disk, and advance to the next data frame is about 20 seconds. The present sequence of 1012 frames of data took approximately 7 to 8 hours to completely digitize and store. Figure 2.7(b) shows a black-and-white photograph taken from a pseudo color re-display of the digitized image of the video frame.

2.3.3 Image-Processing technique

To allow quantitative evaluation of the time-line patterns, each individual digital array was recalled and scanned to establish the location of the first three bubble time-lines. Since the digitized picture retains an inherent degree of noise due primarily to irregularities in both the bubble and lighting uniformity of the time lines (a typical scan-line of image intensity vs. x is shown in figure 2.6(a)), the digital arrays were subjected to a series of image enhancement techniques in order to clarify and identify the bubble-line profiles. To remove extraneous picture noise not related to the bubble-line patterns, linear filters, which were introduced in section 1.3.2, were applied to the picture pixel arrays to produce a band-pass filtered picture. The picture was

filtered twice, and the difference between the two resulting filtered images was determined to yield a band-pass filtered picture, leaving only the major characteristics of interest in the original picture (i.e. the bubble-line contours).

Figure 2.6(b) shows the result of this band-pass filter process for the difference between a 3-pixel filter and 5-pixel filter. The result of this filter is a series of impulse-type peaks reflective of the bubble-line contours only. Note that the maximum amplitude of the 3-pixel filter will always exceed the 5 pixel filter (at the peak bubble-line interesties) but the minimum intensity (between bubble-lines) is higher for the 5-pixel filter. Since the peak intensity region was of primary interest, only the positive difference between the 3-pixel and 5-pixel filter was retained in the band-pass picture; negative differences were set to zero. The resulting band-pass filtered picture was then digitally differentiated with respect to x (refer to section 1.3.3), and the location of the peak intensity for each bubble line was established by the points of zero-crossing in the differentiated intensity gradient. Each detailed step and the result of the line indentification process are shown in figure 2.6(b) for the single scan line shown in figure 2.6(a).

All the image processing techniques described above were based on the following mathematical manipulations. The linear smoothing

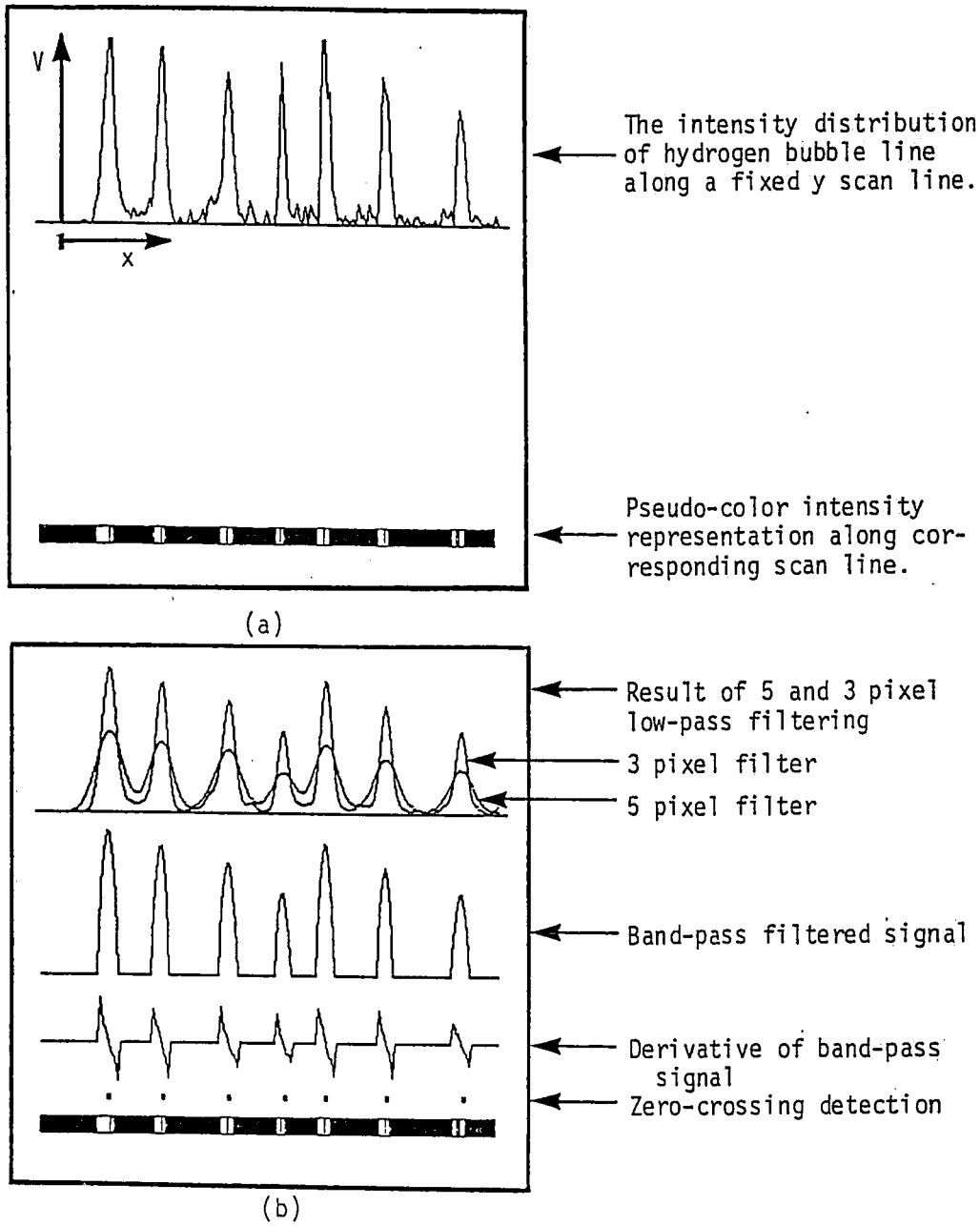

Figure 2.6. Display of the method of detection of hydrogen bubble-line locations from digitized data. Intensity (voltage) vs. position signal for single horizontal sweep (fixed y, variable x) of digitized picture shown in figure 2.5. a) original signal b) filtered and differentiated form of signal shown in a).

or filtering is formulated as :

$$OUT(t) = \frac{1}{T}\int_{t-T/2}^{t+T/2} IN(s)\,ds \qquad (1)$$

where, IN(t) is the input signal, OUT(t) is the filtered output signal, and T represents the sampling window (ie. number of pixels in the averaging window). Based on the above filtering process, the band-pass filter is established as

$$OUTbp(t) = \begin{cases} OUT_1(t) & OUT_1(t) > OUT_2(t) \\ 0 & \text{otherwise} \end{cases}$$

where,

$$OUT_1(t) = \frac{1}{T_1}\int_{t-T_1/2}^{t+T_1/2} IN(s)\,ds \qquad (A)$$

$$OUT_2(t) = \frac{1}{T_2}\int_{t-T_2/2}^{t+T_2/2} IN(s)\,ds \qquad (B)$$

and T_1 and T_2 are the pixel sampling window width. The low-pass filter of step (A) removes the high-frequency picture noise. The low-pass filter of step (B), using a wider sampling window T_2 than that of T_1, provides a more mute background picture. Comparing $OUT_2(t)$ and $OUT_1(t)$, accentuates the picture changes, which are reflected by the intensity distribuation of $OUT_{bp}(t)$. Such a band-pass filter reduces both the ambiguous noise and the broader background variations, making the edge detection process much more accurate.

Using the band-pass filtered picture, the subsequent step is to

identify the location of the hydrogen bubble-lines. A derivaive/zero-crossing edge detection method is used and formulated by the following process. First the derivative of $OUT_{bp}(t)$ is established numerically,

$$OUT_d(t) = d(OUT_{bp}(t))/dt = (OUT_{bp}(t) - OUT_{bp}(t-1))/\Delta t$$

Then the location of zero-crossing, $OUT_{z-c}(t_i)$, is established by the following algorithm

$$OUT_{z-c}(t_i) = \begin{cases} 1 & OUT_d(t_i) = 0 \text{ and } OUT_d(t_i+1)*OUT_d(t_i-1) < 0 \\ 0 & \text{otherwise} \end{cases}$$

The zero-crossing positions in the OUT_d distribution (see figure 2.6) are established as the points lying just between the postive and negative value. When no point lies on (or very near the gradient axis), the point nearest (either postive or negative) the zero gradient axis is taken as the point of zero crossing.

The result of the above procedure is a series of X and Y points indicating the computer indentified locations of a sequence of time-lines. Figure 2.7(c) illustrates the computer identified time-lines for the original video picture (shown in figure 2.7(a)). Since the bubble generation process and lighting introduce further irregularities in the Y direction, which appear in the computer identified time-lines of figure 2.7(c), a second digital smoothing filter is applied to assure that each bubble time line reflects a

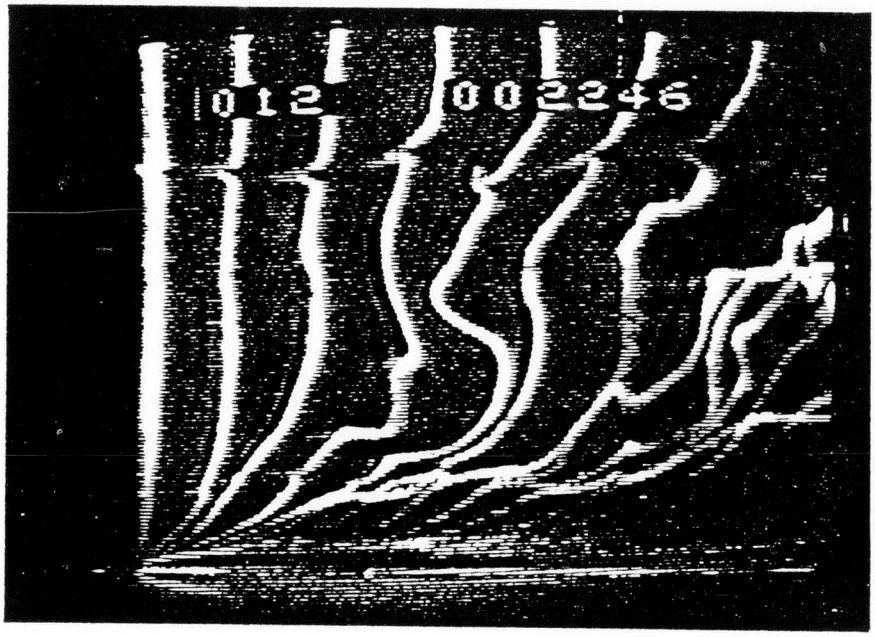

(a)

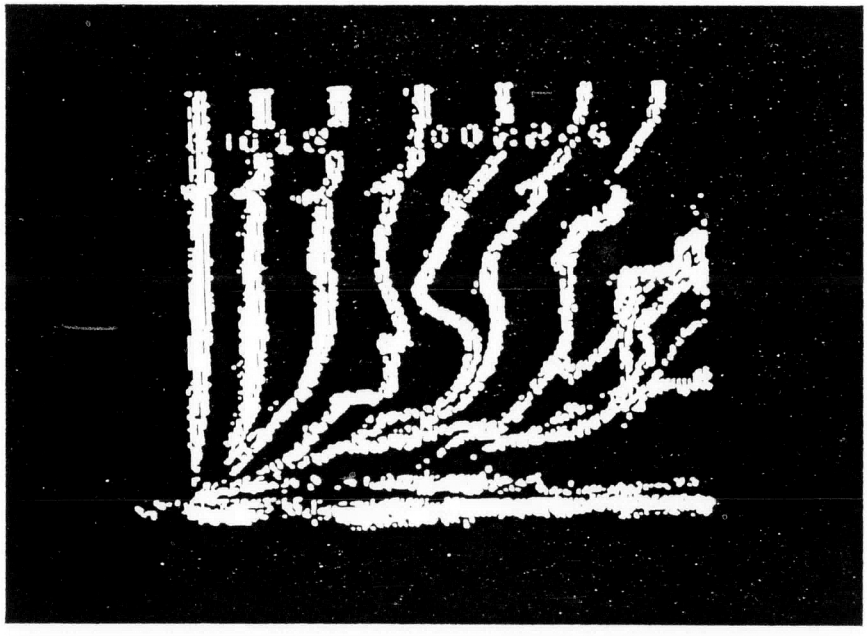

(b)

Figure 2.7 (a) Original video frame
(b) Redisplay of digital frame

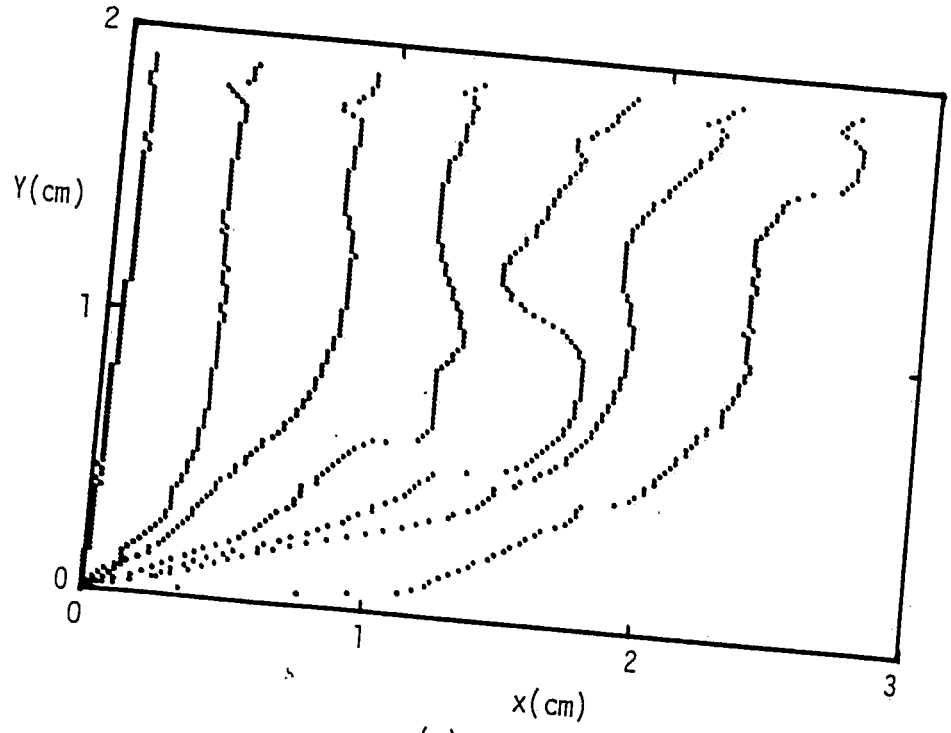

(c)

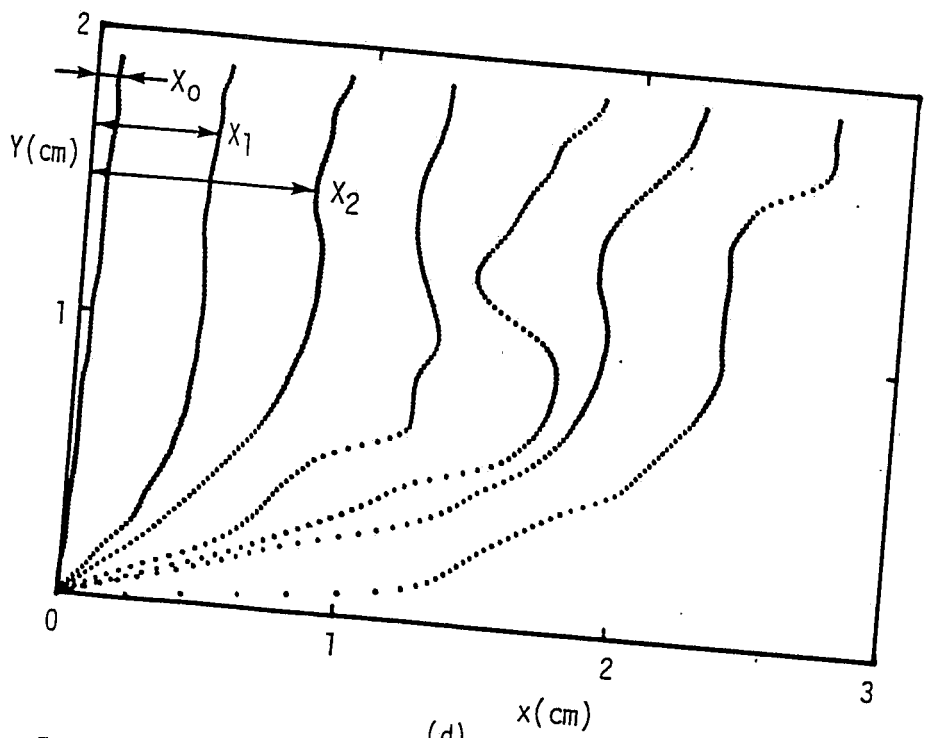

(d)

Figure 2.7 (c) Computer Identified Time-lines

(d) Filtered Time-lines

smooth, continuous curve. The result of this filter on the orginal identified time-lines is shown in figure 2.7(d). A comparison of figure 2.7(a) and 2.7(d) indicates that the computer identified time-lines appear to be accurate reflections of the original bubble time-lines.

2.4 Velocity Determination

For each time-line picture, the local velocity was established for 115 data points in the vertical direction using time-of-flight techniques as outlined in Schraub et al. (1965). The local velocities indicated by the locations of lines one and two are defined by time-of-flight as (refer to figure 2.7(d)):

$$U_1(t,y) = [\, X_1(t,y) - X_o(t,y) \,] / \Delta t$$

$$U_2(t,y) = [\, X_2(t,y) - X_o(t,y) \,] / (\, 2\Delta t \,) \qquad (2)$$

where,

$U_1(t,y)$: local velocity of the first bubble-line, averaged over time interval Δt

$U_2(t,y)$: local velocity of the second bubble-line, averaged over time interval $2\Delta t$

(Note that the bubble-line velocities of U_1 and U_2 are same as 'Ubub' expression later of this section.)

and,

$X_o(t,y)$: the horizontal location of the reference bubble-line

$X_1(t,y)$: the horizontal location of the first bubble-line

$X_2(t,y)$: the horizontal location of the second bubble-line

Δt : the bubble-pulse period (1/30 sec) (i.e. time interval between sequential bubble-line generation)

t : time

y : vertical coordinate, referenced to test surface.

A bubble-pulse rate of 30 Hz was used to optimize the number of data frames per second, yet provide adequate time for sufficient movement of the bubble-lines between data frames. Since the differential between two sequential time lines is taken as the manifestation of the local velocity, the time differential between the two time-lines must be adequate to minimize the uncertainty in the differential measurement, yet short enough to yield reasonable frequency response. 30 Hz was felt to be the optimal rate for the present conditions, yielding uncertainties in instantaneous, local velocities of typically ± 4.7% at Y^+ = 100 (see Appendix B), although higher uncertainties of up to ± 30% occur very near the wall where the velocity is low.

To assure that each bubble-line velocity profile refects the velocity over essentially the same Eulerian region, the pulse generator synchronization circuit is set to initiate the generation of each new bubble time-line approximate 1 msec prior to the subsequent strobe flash (which causes the data-frame exposure). This procedure assures that each new bubble line is in the same phase of

generation when a data frame is exposed. This assures that the differential between the two bubble lines nearest the generating wire always transcends essentially the same region in proximity to the bubble wire.

It has been shown by Davis and Fox (1966), Grass (1971), and Abernathy et al. (1977) that the bubbles generated in the wake of a hydrogen bubble wire move more slowly than the local fluid velocity due to the wake defect effects of the wire. The theoretical equation for the velocity distribution in the far-field, two-dimensional laminar wake behind a circular cylinder without considering the bubble generation, is given as (see for example, Schlichting 1978) :

$$\frac{U_\infty - U}{U_\infty} = \frac{C_d}{4\pi}\sqrt{\frac{U_\infty d}{\epsilon_o}}\left(\frac{x}{d}\right)^{-0.5}\exp\left(\frac{-y\,U_\infty}{4\epsilon_o x}\right)^2 \qquad (3)$$

where,

U : wake velocity

U_∞ : free stream velocity

x : downstream distance from the cylinder

d : diameter of circular cylinder

C_d : drag coefficent of cylinder

y : direction normal to the cylinder surface

ϵ_o : virtual kenematic viscosity.

According to the study of Grass (1971) and Abernathy et al.

(1977), the magnitude of this effect can be generally represented by an equation [simplied from the full laminar wake soluation of equation (3)] of the form

$$\frac{U_{act} - U_{bub}}{U_{act}} = C \left(X/d \right)^{-n} \qquad (4)$$

where,

X : downstream distance of hydrogen bubbles from the generating wire

d : diameter of hydrogen bubble-wire

U_{bub} : bubble velocity (i.e. $U_{bub} = X/\Delta t$)

U_{act} : true fluid velocity

C , n : empirical constants for which n depends on both the local Reynolds number and the wire drag coefficient (see equation (3))

Fitting the empirical constants to hot-film anemometry measurements, Grass suggests a wake correction curve of C = 3.62 and n = 0.729 for $40 < x/d < 200$ and $Re_d = 3.3$ (Reynolds number based on the diameter of hydrogen bubble-wire). Subsequently, Abernathy et al. (1977), employing empirical data obtained using a Laser-Doppler anemometer, suggests a center-line velocity defect correlation of C = 1.3 and n = 0.5 for $3 < Re_d < 40$. For the center line velocity defect of equation (3) (i.e. at y = 0), both equations (3) and (4)

are coincident with n = 0.5. Since the present results were for 0.2 < Re_d < 3.2 (note that Red = 0.2 is obtained in the region very near the wall and Re_d = 3.2 occurs in the outer region of measurement) and 8 < x/d < 270, this is comparable with the bubble velocity defect data of Abernathy et al. (1977) for 2.8 < Re_d < 7.1. Data taken in our present flow facility using a bubble-wire towed at constant speeds through the quiescent channel compared with the bubble velocity data record suggests that C = 1.7 provides a reasonable fit of the data.

Using equation (4) with C = 1.7 and n = 0.5, the bubble-line velocity data was computer corrected to yield local fluid velocity, averaged over the bubble-pulse period. Note that very near the wall (Y^+ < 4 to 5) reflected light from the wall made it very difficult to discriminate the bubble-line location; in addition, the low relative velocity within this region required excessive defect corrections. To provide an appropriate representation of the velocity behavior within this sublayer region, linear behavior was assumed from the velocity determined at Y^+ = 4 ~ 5 to the zero-slip condition at the surface [an assumption which appears to be substantiated by recent results of Falco et al. (1985)].

Clearly, the corrected velocity is not a true instantaneous value since it entails essentially a Taylor approximation (i.e. assuming that the corrected Lagranian time-line velocity reflects

the local Eulerian velocity). However, this assumption would seem to be reasonable because of the limited transit distance between bubble time-lines and the relatively short averaging time. The accuracy of this assumption is also borne up by the close comparison of the time-averaged, boundary-layer velocity statistics with accepted probe measurements, as shown in the following results and discussion chapter.

Making the assumption that the differential in horizontal distance reflects the true x-direction velocity is also an approximation since the bubble lines will move and deform in response to all three velocity components. The assumption is that for small differential distances between bubble lines the much smaller magnitudes of the v and w velocity components relative to u will have a negligible influence on bubble-line deformation [see Schraub et al. 1965]; in essence the present technique is similar to the measurement of boundary layer characteristics using a single-element hot-film anemometer. Again comparison with accepted boundary-layer statistics appears to support the above assumption (see Chapter 3).

3. RESULTS and DISCUSION

3.1 Velocity Profiles

Using the image processing technique described in Chapter 2, 1012 velocity profiles were obtained for a video sequence of over 33 seconds ($t^+ = 2300$) (30 profiles / second; see section 2.2.2). The first 10 seconds (300 velocity profiles) of this sequence are shown in figure 3.1. An indicated in the figure, these profiles span a range of $0 < Y^+ < 155$ and $0 < t^+ < 700$, based on inner layer variables ($Y^+ = yU_\tau/\nu$, $t^+ = tU_\tau^2/\nu$). Each profile is established by 115 pixel points in the Y direction. Since the local velocities depend upon differences in discrete pixel locations (see equation (2) of section 2.4), this creates uncertainties in the instantaneous profile from $\pm$ 4.7% at $Y^+ = 100$ to $\pm$ 30% very near the wall.

3.2 Time-Average Statistics

Profiles of time-average velocity, turbulence intensity, skewness, and flatness for the entire digitized sequence are shown in figures 3.2 to 3.6. Data obtained using both the first and second bubble-lines (refer to equation (2) in section 2.4) are shown; previously published results are shown for comparsion. The figures are presented using both a linear scale, which better illustrates the behavior of the outer region, and a semi-logarithmic scale, which emphasizes the characteristics of the inner region. Note that the uncertainties of the data vary due to the different averaging

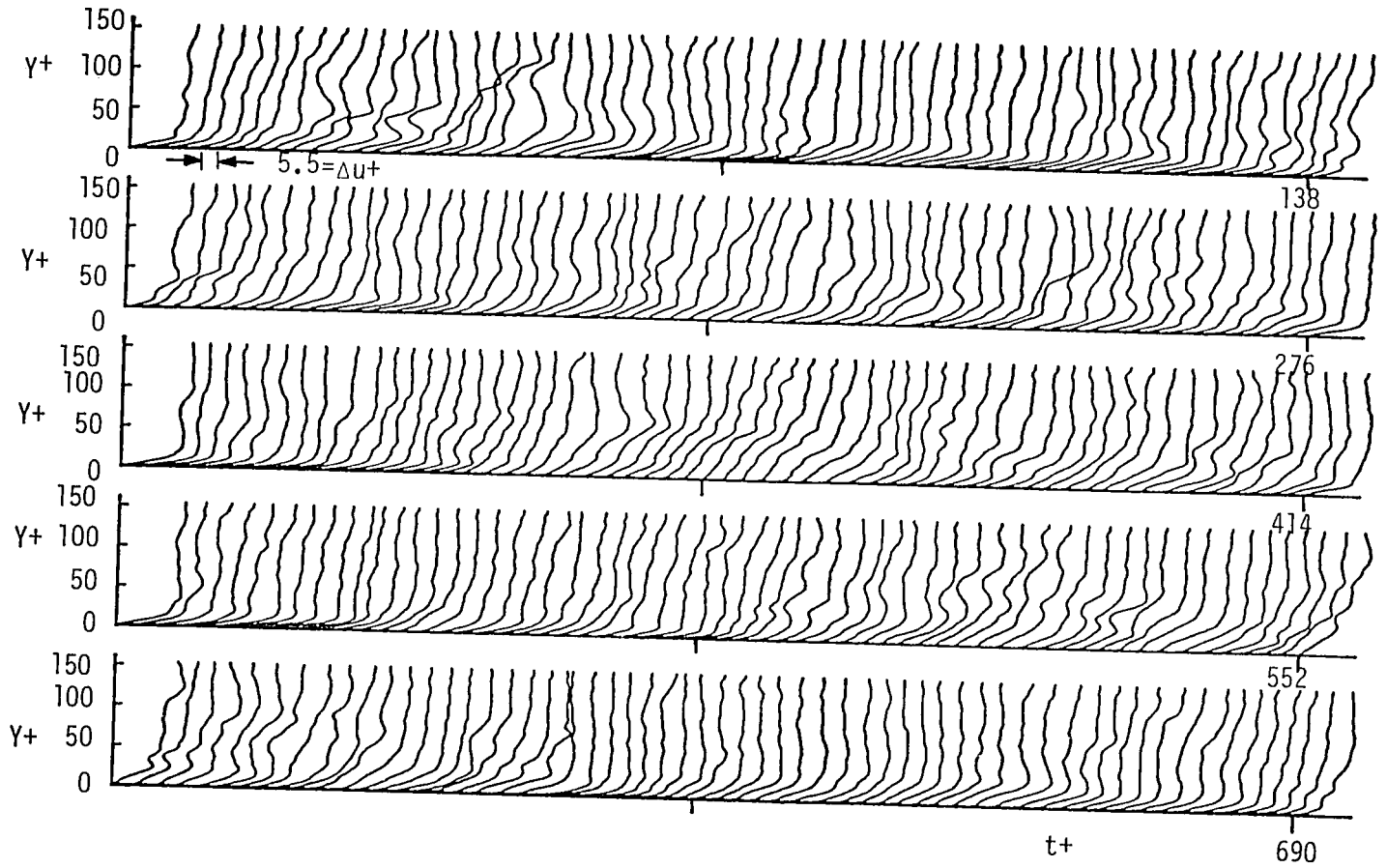

Figure 3.1 Sequence of instantaneous velocity profiles determined from image processed hydrogen bubble flow visualization. Each profile is $\Delta t^+=2.3$ apart; times are from the start of sequence, and each profile is offset by $\Delta u^+=5.5$.

equations (see Kline and McClintock 1953); typically, uncertainties in the vicinity of $Y^+ = 100$ are ± 0.21%, ± 3%, ± 7%, ± 18% for mean velocity, turbulence intensity, skewness, and flatness factors respectively (see Appendix B). The uncertainties generally increase with proximity to the wall due to corresponding increases in the uncertainty of the instantaneous velocities.

The Reynolds number based on momentum thickness for the present study was Ree = 1120. For a low Reynolds number turbulent boundary layer, this implies a proximity to transition. However, the law-of-the-wall is essentially independent of Reynolds number, as was suggested by Coles (1956, 1962). Purtell et al. (1981) have also demonstrated that the law-of-the-wall characterization does not vary with Reynolds number (although the applicable range will change with increasing Reynolds number). These studies suggest that the present results should behave logarithmically, and that the shear velocity, U_τ, can be determined by fitting the mean velocities to the accepted empirical law-of-the-wall curve. The mean velocities are determined using the time-average equation,

$$\bar{U}(y) = \frac{1}{T}\int_0^T u(t,y)\, dt. \qquad (5)$$

The form of the law-of-the-wall equation used is

$$U^+ = 2.44 \ln Y^+ + 4.9 , \qquad (6)$$

as suggested by Clauser (1956),

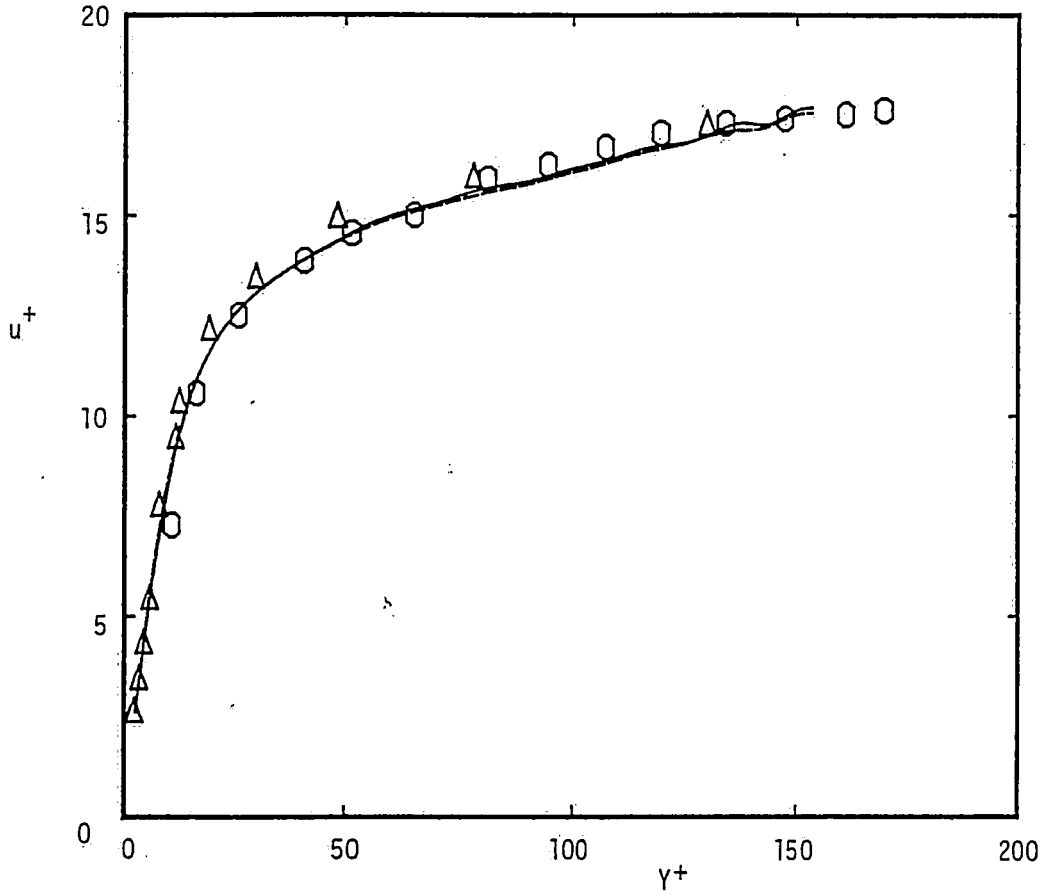

Figure 3.2. Mean velocity profile, linear scale: ——, first bubble-line data; ---, second bubble-line data. Re_θ=1120. O , Grass (1971)[bubble-line data], Re_h=6740; Δ, Johansson and Alfredsson (1982), Re_h=13800.

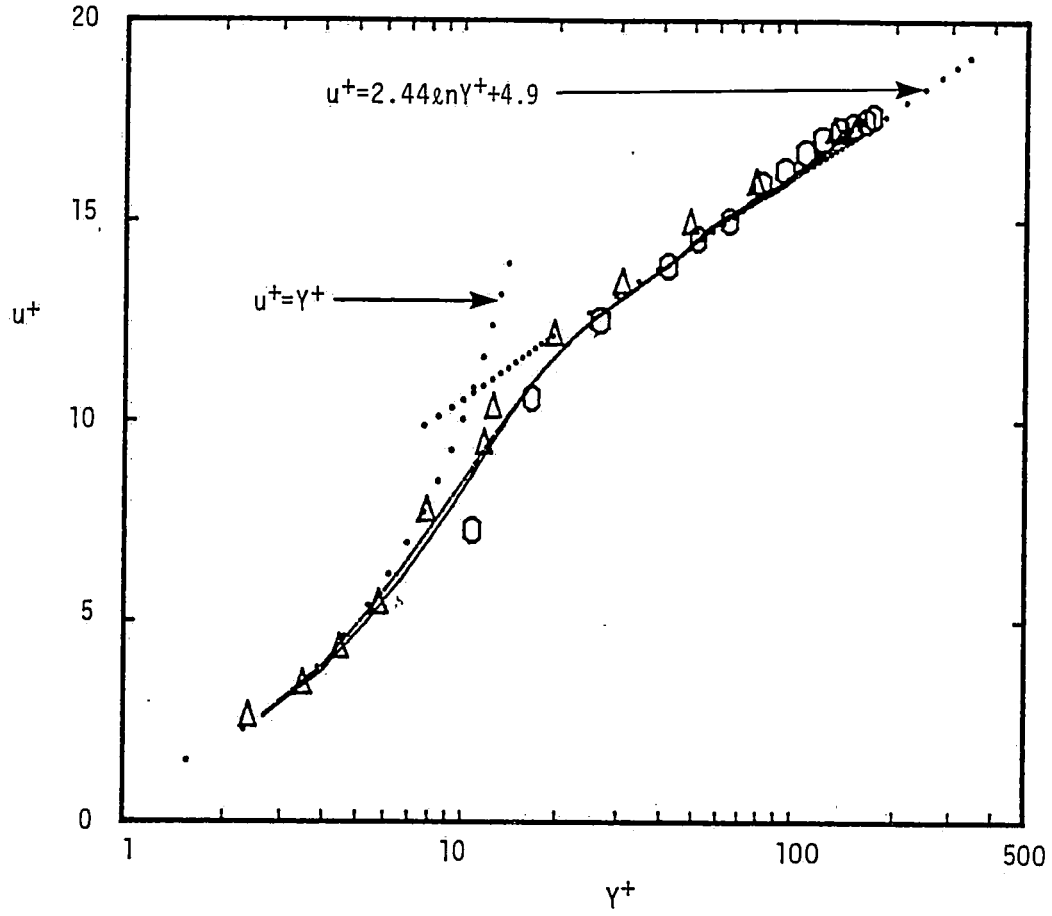

Figure 3.3. Law-of-the-wall plot of mean velocity. Same legend as figure 3.2.

where, $Y^+ = yU_\tau/\nu$ and $U^+ = U(y) / U_\tau$.

The fitting process uses a method of least squares regression analysis, with the U_τ value determined by fitting the present data to the law-of-the-wall equation. The value of the shear velocity, U_τ, was determined using a computer optimized fitting routine to be 0.0273 ft/sec for both bubble-line data records; this corresponds to a skin friction coefficient [$C_f = 2\,(U_\tau/U_\infty)^2$ for $U_\infty = 0.6$ ft/sec] of 0.0041. Note that in the region $Y^+ < 4$, the bubble data was quantified as close to the surface as the computer identification process would accurately allow; beyond this point, a linear profile was fit from the last identified data point to zero velocity at the surface (see discussion in section 2.4). Note that this approximation demonstrates a good fit with accepted very near-wall behavior. In the region $Y^+ > 30$, the present data are extremely close to the law-of-the-wall equation, as well as the Grass bubble-line data (1971) and the probe data of Johansson and Alfredsson (1982) (see figures 3.2 and 3.3). The comparison of average velocity profile data with these previous results appears particularly good, indicating that the determination of quantitative data from the bubble-line time-of-flight data appears to work quite well.

The turbulence statistics of intensity, skewness, and flatness

are established as follows :

Second Moment

$$\overline{U'(y)^2} = \frac{1}{T}\int_0^T (u(t,y) - \bar{U}(y))^2 \, dt \qquad (7)$$

(turbulence intensity; root mean-square)

$$Urms(y) = \left(\overline{U'(y)^2} \right)^{1/2}$$

Third Moment

$$\overline{U'(y)^3} = \frac{1}{T}\int_0^T (u(t,y) - \bar{U}(y))^3 \, dt \qquad (8)$$

(Skewness, normalized on Urms)

$$S(y) = \overline{U'(y)^3} \,/\, Urms(y)^3$$

Fourth Moment

$$\overline{U'(y)^4} = \frac{1}{T}\int_0^T (u(t,y) - \bar{U}(y))^4 \, dt \qquad (9)$$

(Flatness, normalized on Urms)

$$F(y) = \overline{U'(y)^4} \,/\, Urms(y)^4$$

In figures 3.4(a) and 3.4(b), comparative turbulence intensity data from Laufer (1954), Klebanoff (1956), Kim (1971), Grass (1971), and Johansson and Alfredsson (1982) are shown in conjuction with the present results. The comparsion of the data for both the first and second bubble-lines appears generally consistent, with the data from the first bubble line generally 5 to 10% higher than the second line data. This discrepancy may be due to the difference in the time-of-flight interval for the two bubble-lines, which modifies both the

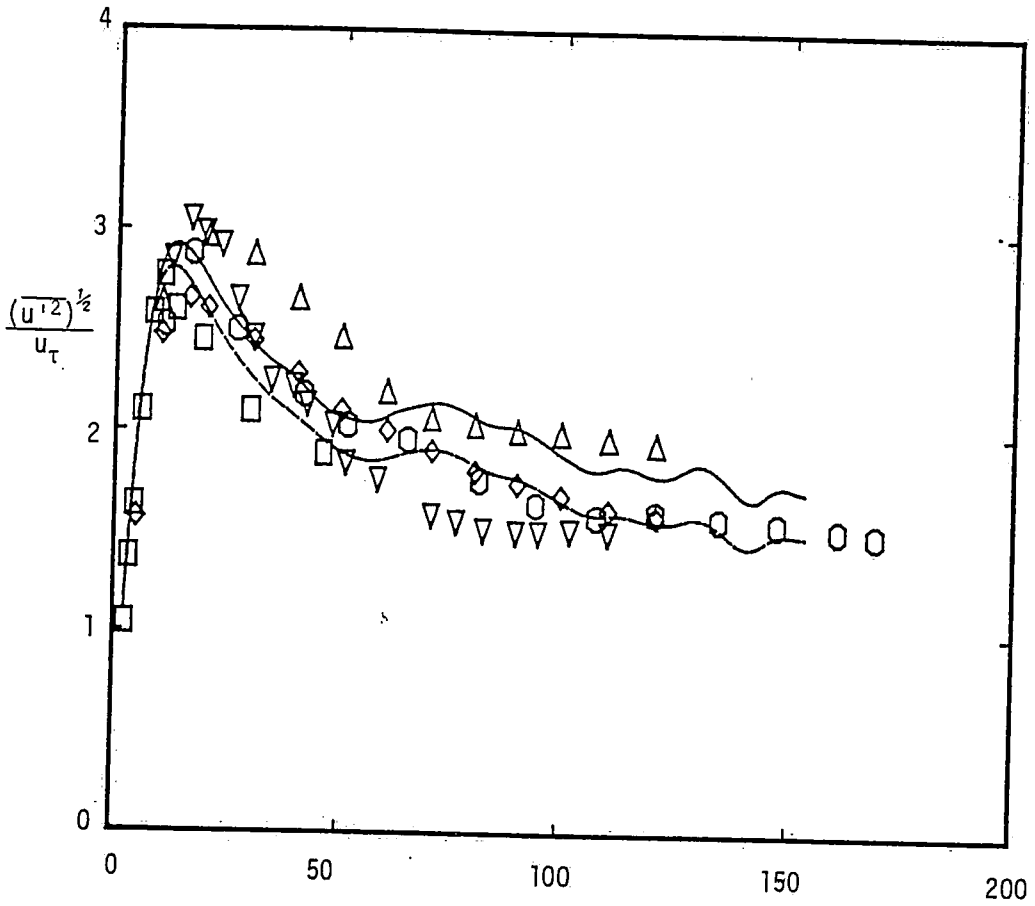

Figure 3.4(a) Turbulence intensity profile, linear scale: ——, first bubble-line data; ---, second bubble-line data. Re_θ=1120. ◇, Laufer (1954), $Re_D=5\times10^4$; Δ, Klebanoff (1956), $Re_x=4.2\times10^6$; ▽, Kim et al. (1971)[bubble-line data], Re_θ=666; ○, Grass (1971) [bubble-line data], Re_h=6740; □, Johansson and Alfredsson (1982), Re_h=13800.

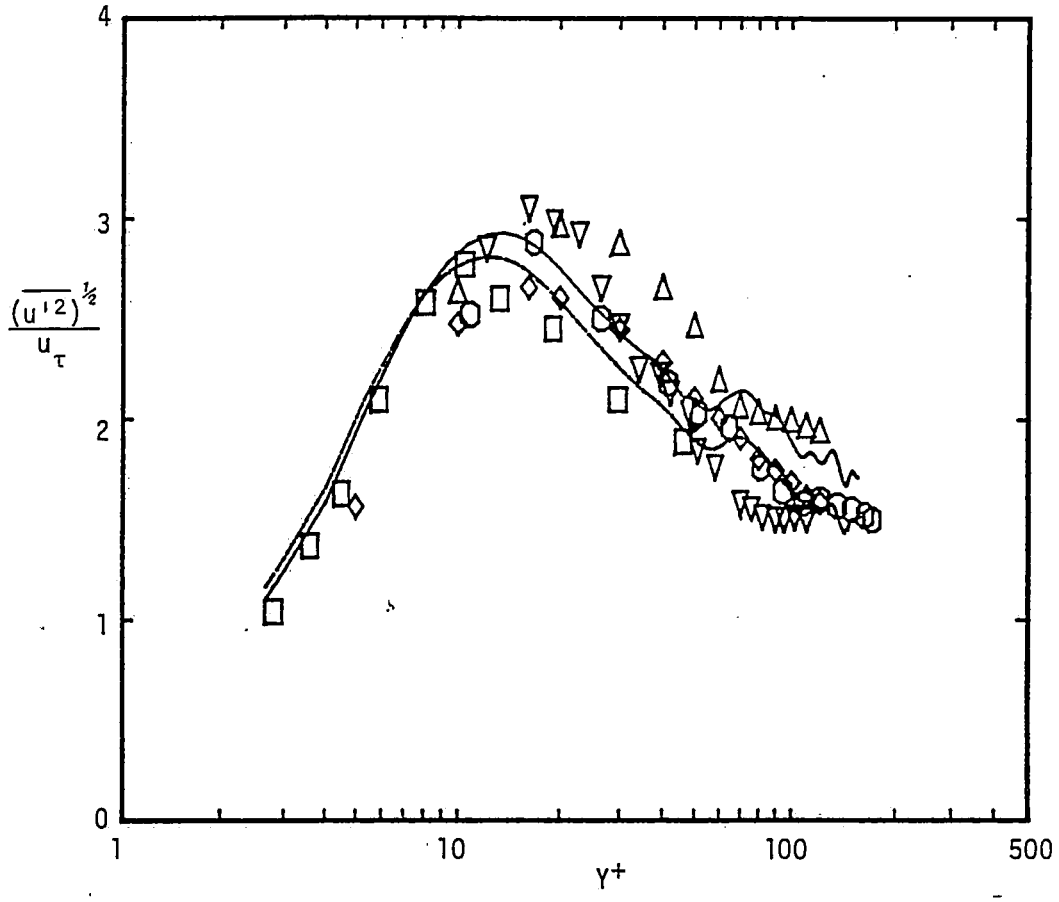

Figure 3.4(b) Turbulence intensity profile, semi-log plot.

frequency response and the uncertainty of the respective data sets.

The time-of-flight interval (i.e. the time interval between the bubble line and the bubble wire) of the first bubble-line is one-half the interval of the second bubble-line; thus, the frequency response of the velocity derived from displacement of the first bubble-line is higher than the frequency response using the second bubble-line. This difference in response characteristics should yield lower turbulence intensity values for the lower response data (i.e. second bubble-line), as is indicated. A second factor affecting the turbulence statistics is the difference in the uncertainty of the bubble velocity for the two data sets, since a smaller time-of-flight displacement results in a higher uncertainty (i.e. for an identical uncertainty in Δt, a lower value of Δx results in a higher uncertainty in u). Clearly, the uncertainty in u will be lower for the second bubble-line than for the first bubble-line due to Δx differences of a factor of two. These uncertainity and frequency response effects do not appear to substantially bias the first moment of mean velocity for either bubble-line data set. However, for the second, third, or fourth velocity moments the effects of uncertainties, particularly frequency response effects, appear to create both deviations and irregularities in the reduced data. However, despite these variations, the results for the second, third, and fourth moment still appear to conform to previously measured distributions.

Figure 3.4(b) indicates that the maximum turbulence intensity normalized on U_τ reaches a value of approximately 2.8 ~ 2.9 at about Y^+ = 12 to 13, which is consistent with the comparative data which indicates a maximum occurring from Y^+ = 10 to 20 and $(\overline{U'^2})^{1/2}/U_\tau$ = 2.6 to 3.1. The linear plot of the turbulence intensity in figure 3.4(a) indicates a bit of irregularity in the region Y^+ = 60 to 140; this may be a result of the limited range of the data, which could result in a very low frequency bias of the results, and thus the irregularities in the time-averged curves.

The skewness and flatness of the bubble-line data, compared with the hot-film results of Johansson and Alfredsson (1982), are shown in figures 3.5 and 3.6. The comparsion in figure 3.5(a) appears generally good, with the largest variations being lower values of skewness and flatness very near the wall for the present data. These variations of the third and fourth moment very near the wall, while not significantly aberrant, are propably due to the resolution limitation of the present data in the region $Y^+ < 5$, as discussed in the experimental technique section. The variations noted in the region are again most likely the result of the same frequency and uncertainty limitations noted in the above discussion of the second moment results.

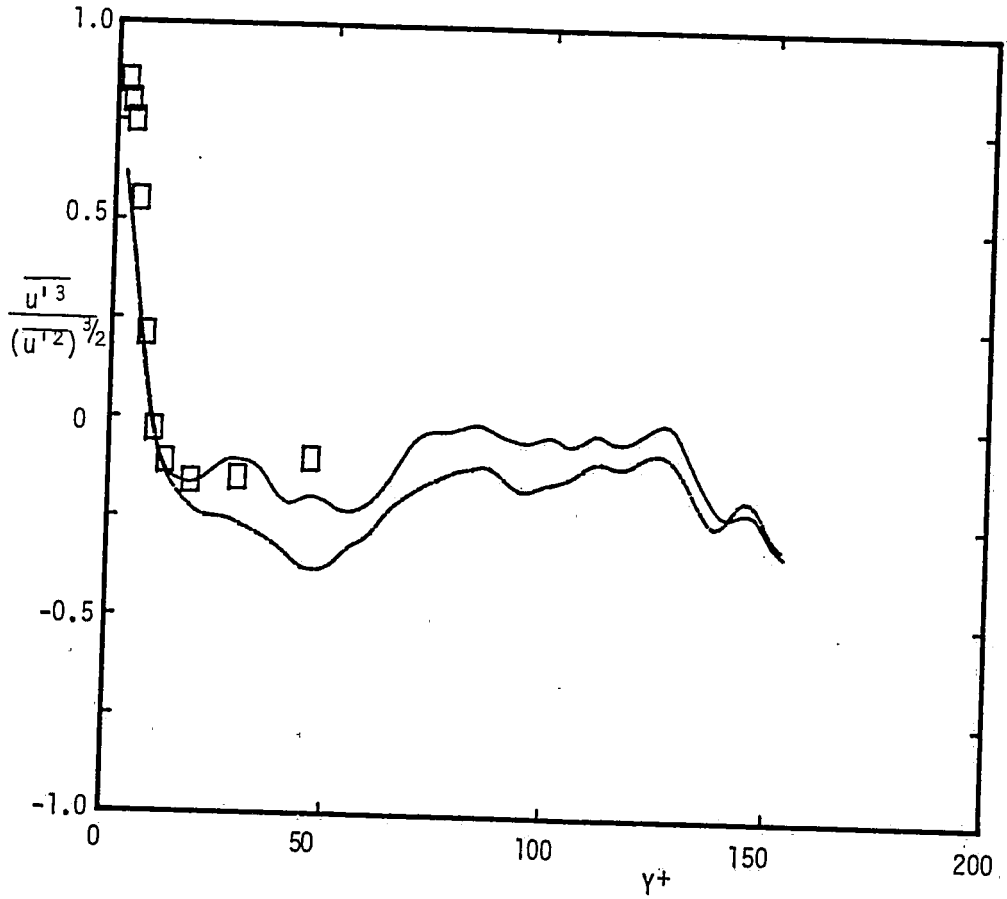

Figure 3.5(a) Velocity skewness profile, linear scale: —, first bubble-line data; ---, second bubble-line data. Re_θ=1120. □ , Johansson and Alfredsson (1982), Re_h=13800.

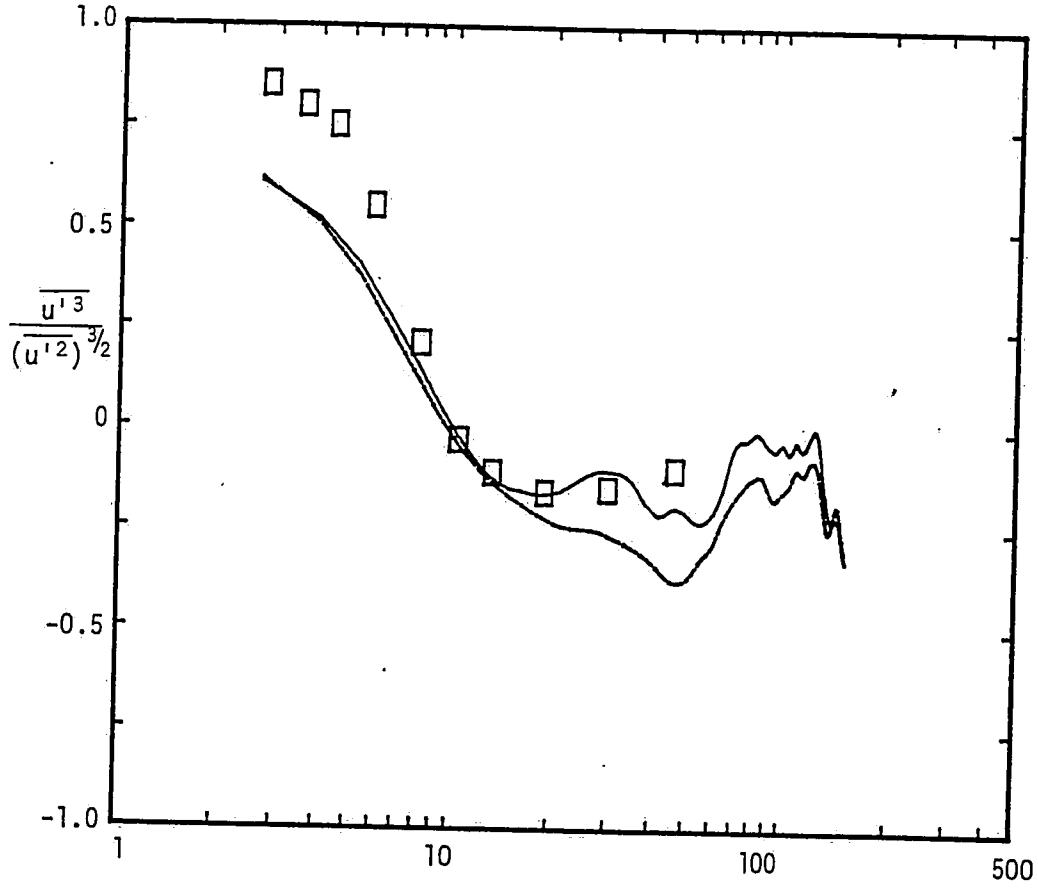

Figure 3.5(b) Velocity skewness profile, semi-log scale.

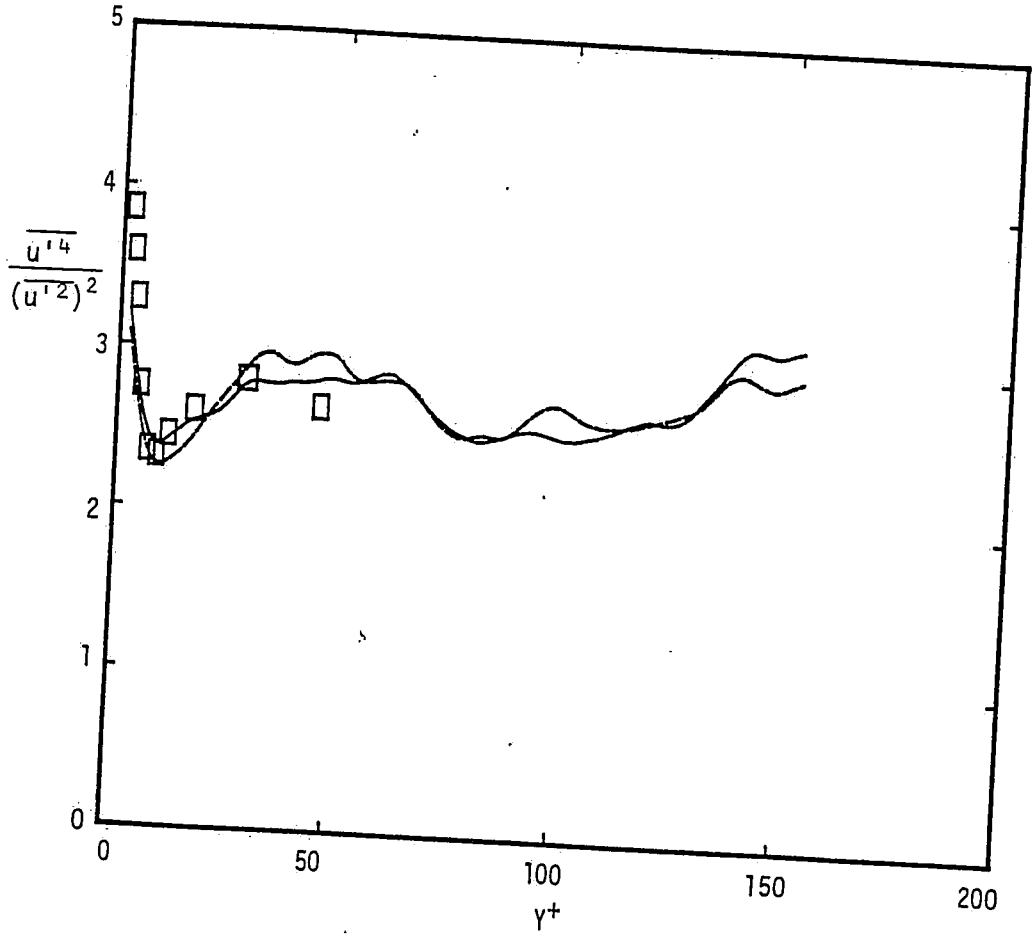

Figure 3.6(a) Velocity flatness profile, linear scale: ——, first bubble-line data; ---, second bubble-line data. Re_θ=1120. □, Johansson and Alfredsson (1982), Re_h=13800.

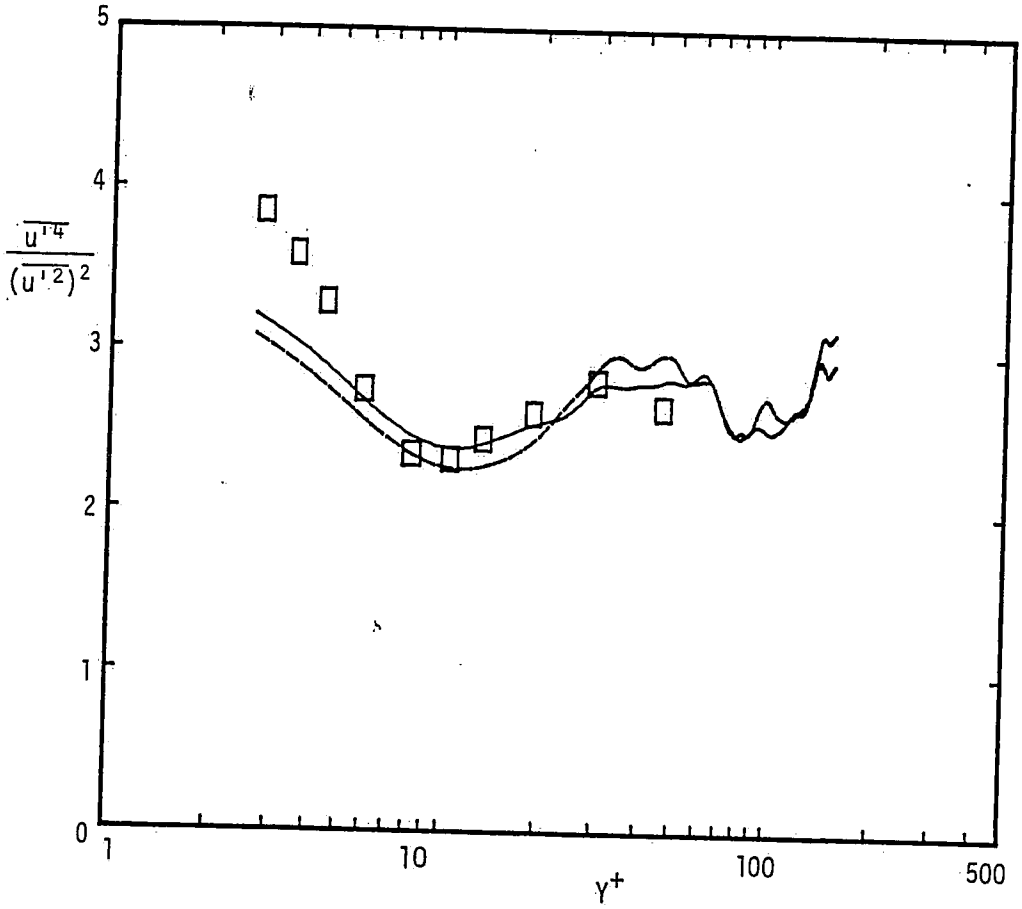

Figure 3.6(b) Velocity flatness profile, semi-log scale.

3.3 Burst Detection Statistics

One of the primary motivations for development of the present technique for determining instantaneous velocity data was to provide a mechanism for comparative evaluation of probe-type burst detection schemes with the flow visualization techniques which first revealed the details of the bursting process (i.e. Kim et al. 1971). Figure 3.7 illustrates the instantaneous fluctuating velocity vs. time behavior at a series of selected points across the wall region, as determined from the present results. Note the similarity of the results to the simultaneous velocity data taken with rake-type anemometers (e.g. see Blackwelder and Kaplan 1976). The corresponding short-time variance parameter as employed in the VITA technique (Blackwelder and Kaplan 1976) is shown in Figure 3.8. The short-time variance was determined from the fluctuating velocity data of figure 3.7 using the defining equation,

$$Var(t,T) = \frac{1}{T}\int_{t-1/2T}^{t+1/2T} U(s)^2 ds - \left(\frac{1}{T}\int_{t-1/2T}^{t+1/2T} u(s)\, ds\right)^2 \qquad (10)$$

with $T^+ = 11$. The data shown in figure 3.8 is normalized on $\overline{u'^2}$ (fluctuating normal stress), yielding a measure of local flow "activity".

Interestingly, the present data indicates that peaks in the short-time variance are not particularly localized, but appear to occur in a quasi-organized pattern across the boundary layer. In

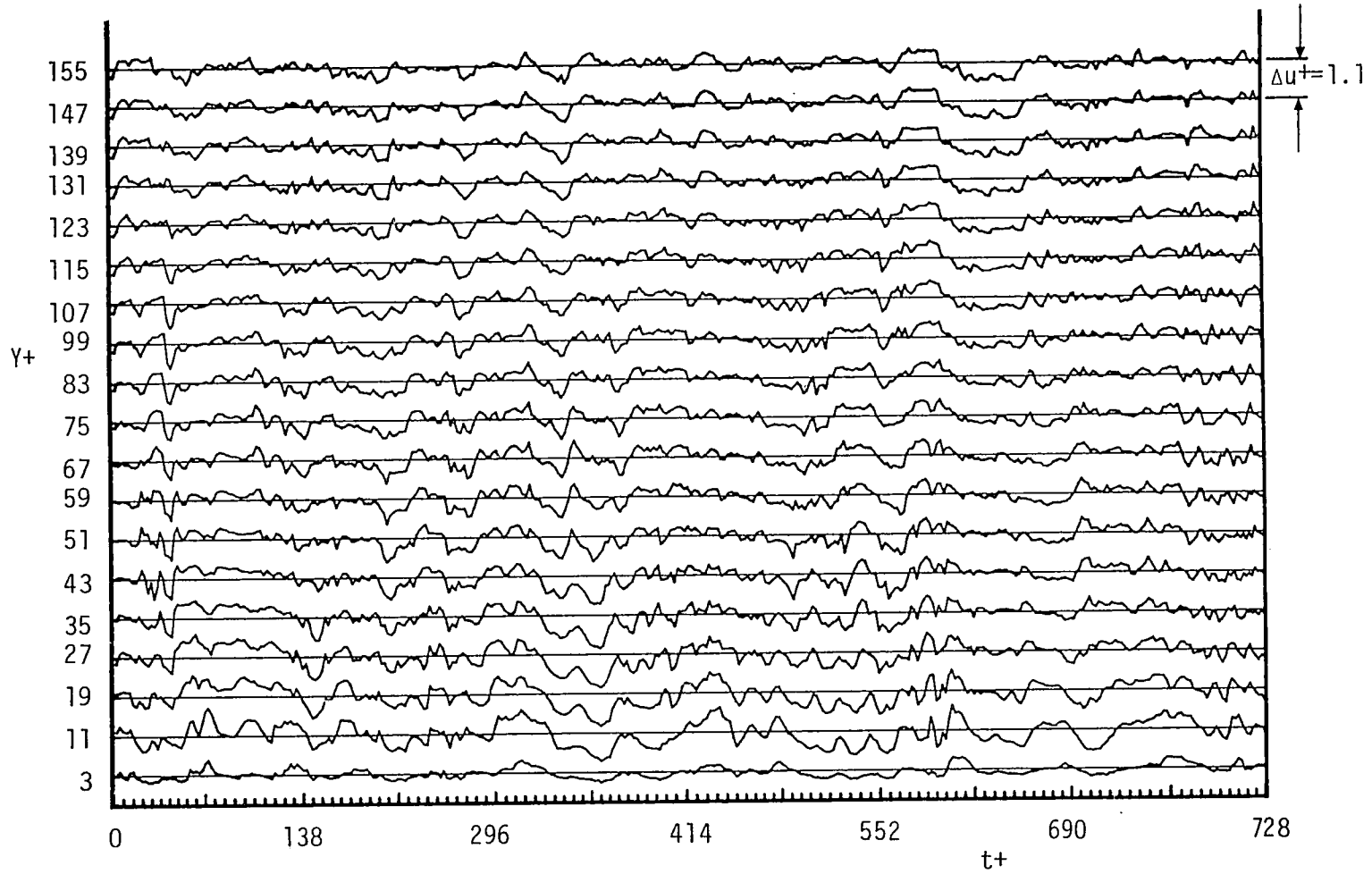

Figure 3.7 Instantaneous Streamwise Velocity Behavior at Selected Heights Above Surface.

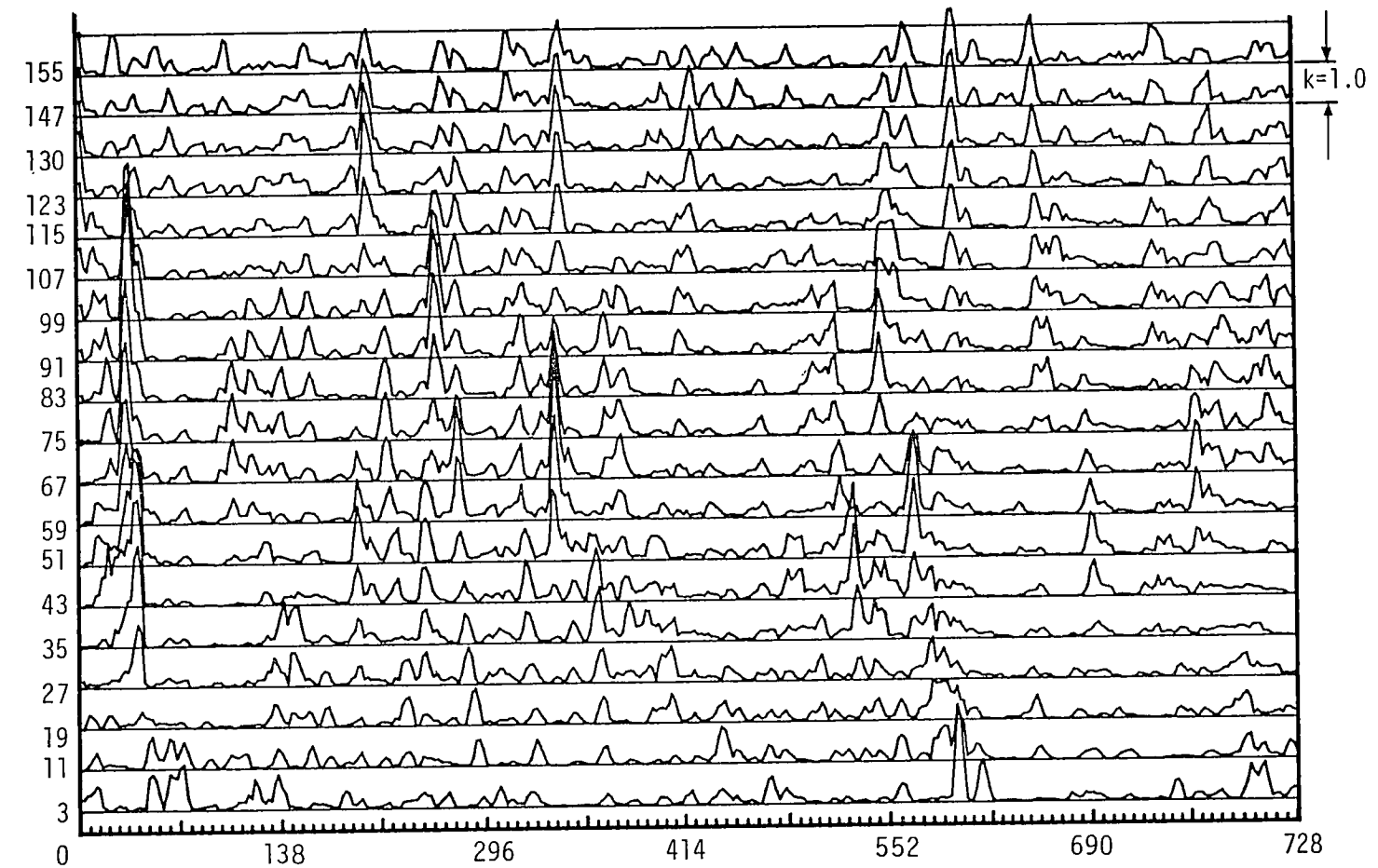

Figure 3.8 Short-time Variance of Velocity Signals shown in Figure 3.7. Amplitude of Curve Represents $K=Var(t,T)/\overline{u'^2}$.

fact, some of the largest peaks in figure 3.8 occur in regions well beyond $Y^+ = 15$, which is the generally accepted location for detection of "bursting".

To further accentuate the regions of "bursting" activity, as defined by the VITA technique, both isocontours and a series of instantaneous profiles of short-time variance are presented in figure 3.9 for the first 4 seconds ($0 < t^+ < 276$) of data. Both the isocontours and the profiles appear to confirm that the regions of most "active" behavior occur away from the surface, in the early logarithithmic region. In addition, the contiguous burst contours marked A and B in figure 3.9 appear to indicate that the passage of outer regions of activity either give rise to, or are followed by, regions of inner activity (this observation is consistent with the previous investigation of Blackwelder and Kaplan 1976). If one reviews the corresponding velocity data in figure 3.7 for the time-span over which the bursting contours A and B occur, this pattern of outer activity preceding inner activity can be oberved, although not nearly so clearly.

For comparison, a sequence of 12 scenes from the video sequence comprising burst contour B are shown in figure 3.10. Note that in the video sequence the bubble-line patterns observed in the center of the pictures are manifestations of flow structures or motions detected in the quantitative velocity approximately $\Delta t^+ = 9$ to 10

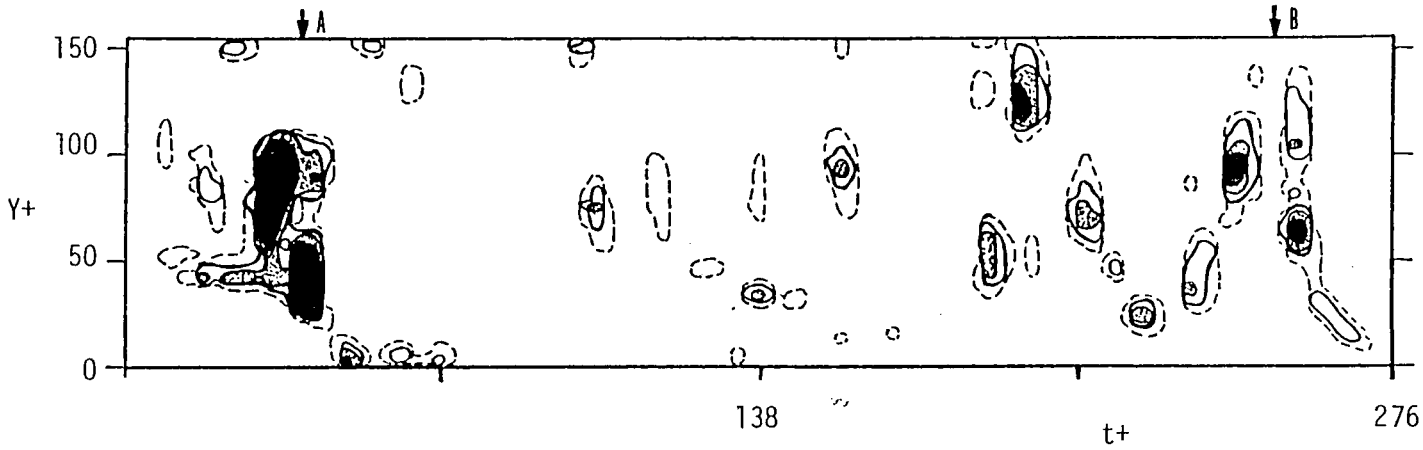

(a)

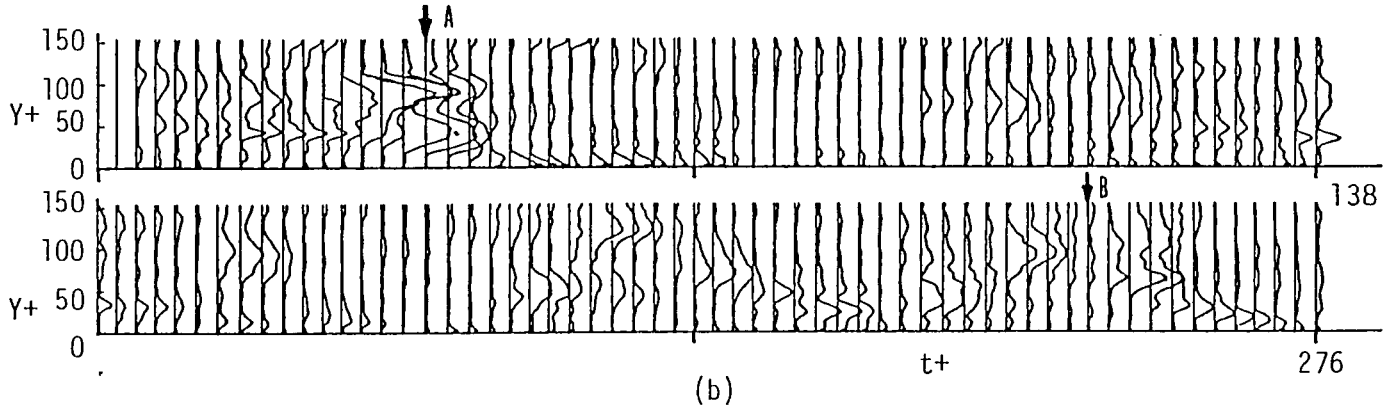

(b)

Figure 3.9(a) Contours of $k=Var(t,T)/\overline{u'^2}$. A and B indicate contiguous burst contours. ---, k=0.5; ——, k=0.75; dotted area, k=1.0; darkened area, k=1.25.
(b) Instantaneous VITA prpfiles corresponding to contours in (a).

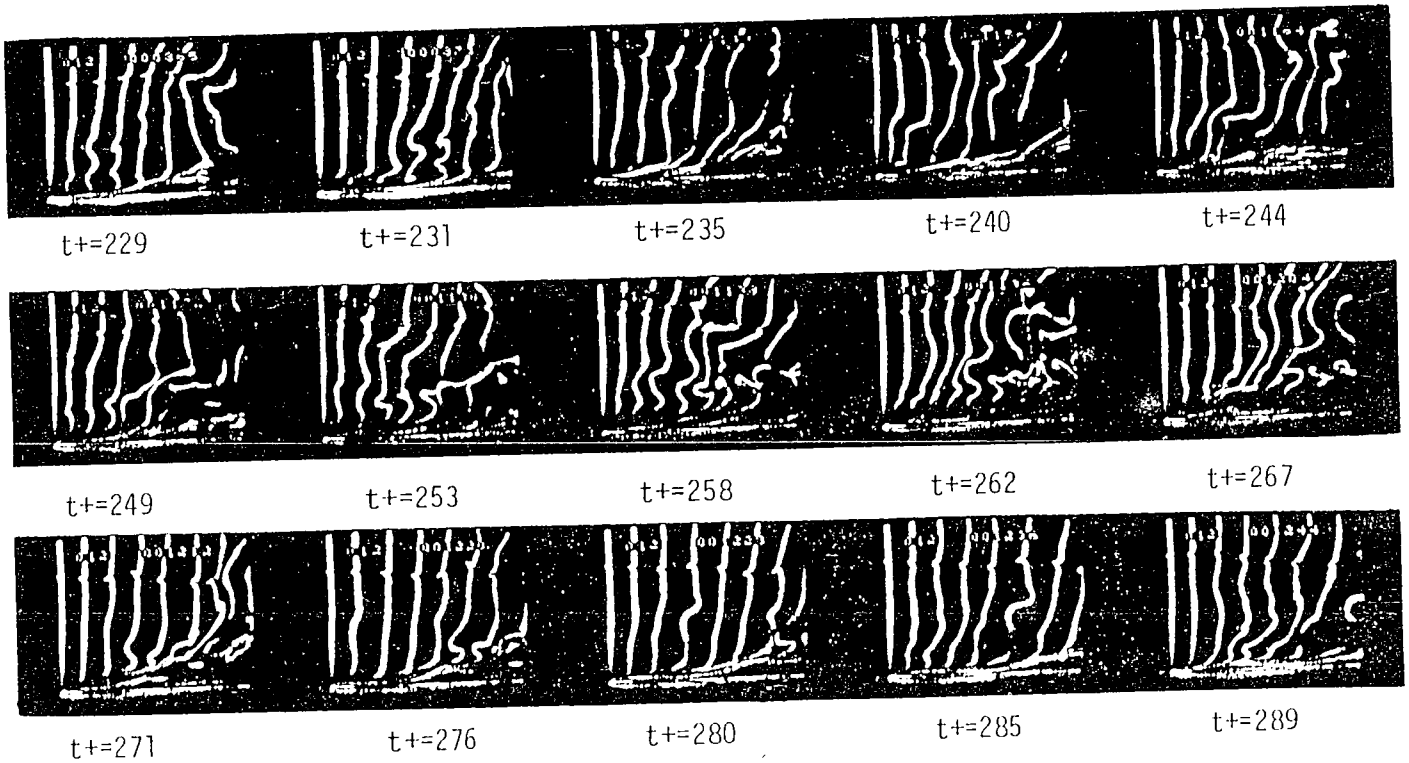

Figure 3.10. Scenes from original video sequence illustrating visualization patterns during burst contour labeled as B in figure 3.9.

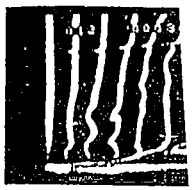

t+=229

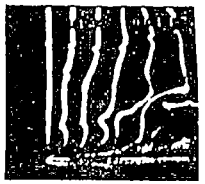

t+=249

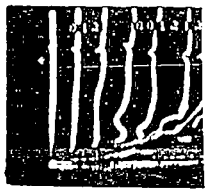

t+=271

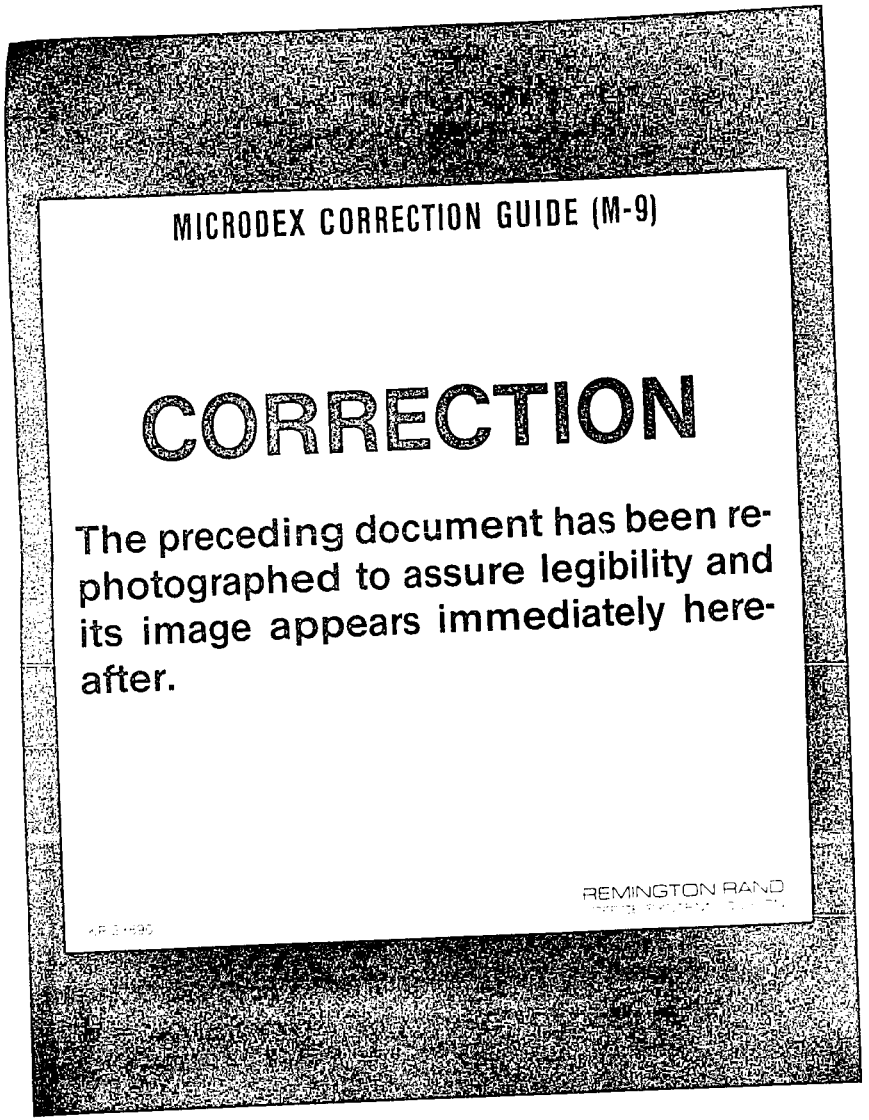

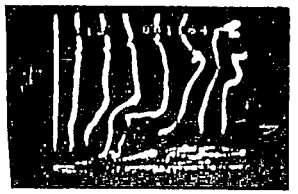

t+=244

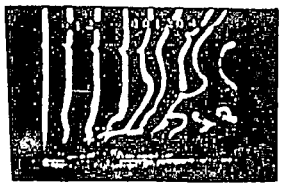

t+=267

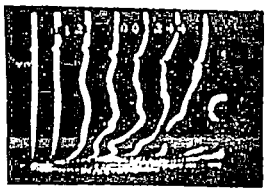

t+=289

Figure 3.10. ɔn patterns

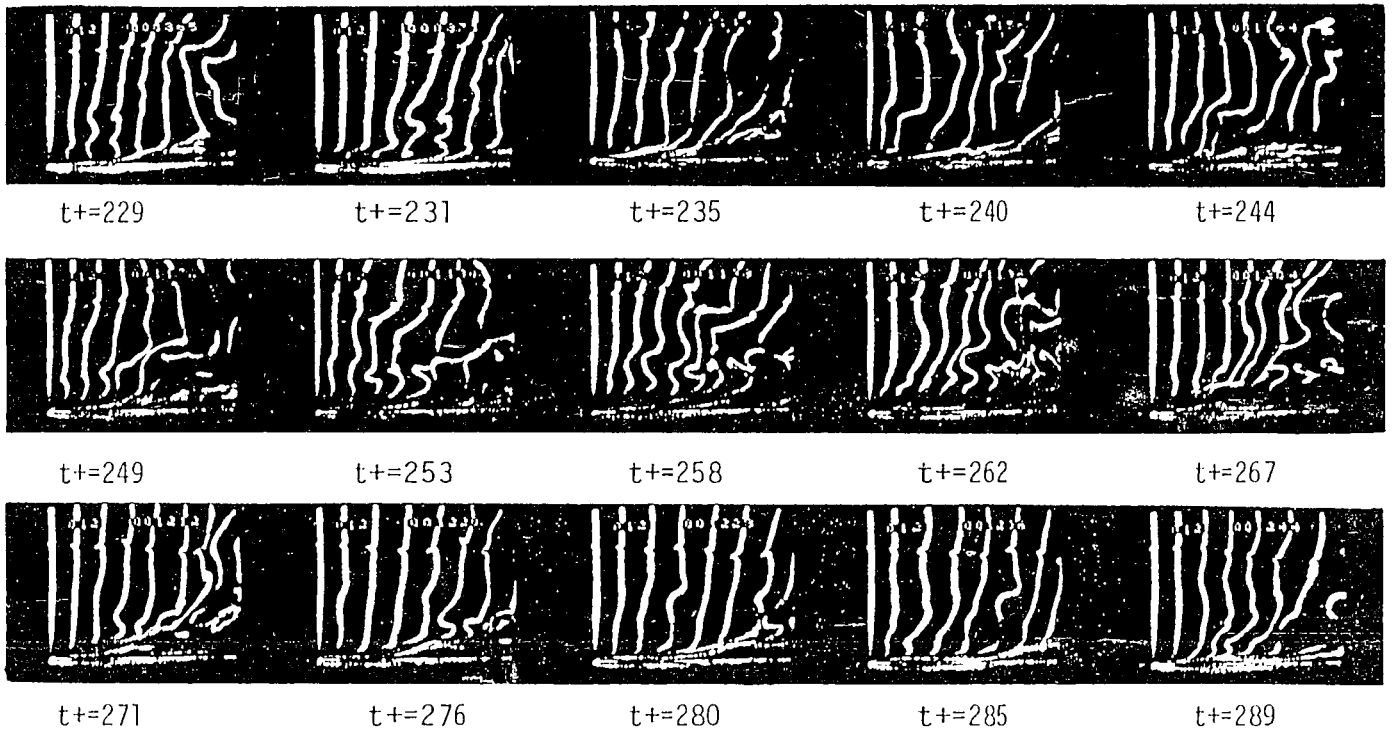

Figure 3.10. Scenes from original video sequence illustrating visualization patterns during burst contour labeled as B in figure 3.9.

earlier in the sequence. Keeping this in mind, one can observe the passage of an outer flow structure (as evidenced by the transverse kink at $t^+ = 244$), followed by a secondary, streamwise structure nearer the wall ($t^+ = 253$ to 262), which leads to a lift-up and acceleration of sublayer fluid ($t^+ = 267$), terminated by a sweep-type event ($t^+ = 276$). Basically, these events can be roughly traced in the contours of short-time variance in figure 3.9(a).

3.4 Instantaneous Turbulence Statistics and Relation to Coherent Behavior

3.4.1 Instantaneous Turbulence Statistics Profile

Using numerical differentiation and manipulation of the velocity profile data, the velocity properties of du/dy, d^2u/dy^2, and du/dt were derived to support conventional profiles of u, u' and VITA. As an aid in the examination of bursting behavior, a property which is the product of VITA and u' was also established to examine its potential utility in helping establish burst identification. Figure 3.11 shows a series of typical profiles corresponding to the visual sequence A indicated in figure 3.9 (Appendix C provides profiles for the entire visualization sequence of first bubble-line data examined in the present study). The profiles cover a spatial region of $1 < Y^+ < 155$ and time intervals of $\Delta t^+ = 2.3$.

Because the velocity profiles are not truly continuous, some

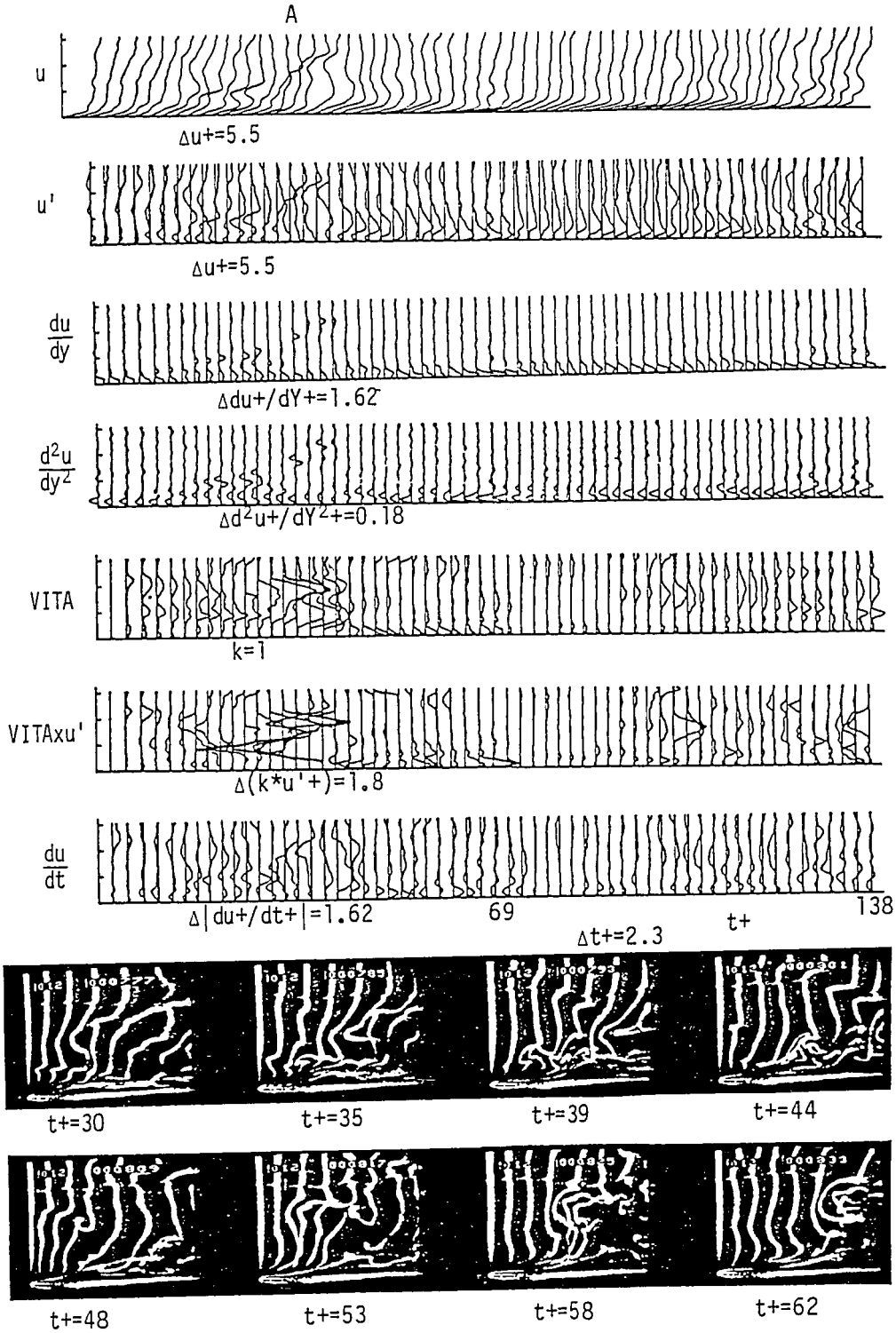

Figure 3.11. Profiles of velocity properties derived from velocity profile data. Sequence spans bursting contour A indicated in figure 3.9.

adaptation was necessary to determine the particular properties shown in figure 3.11. The velocity fluctuation (u') profiles were established by subtracting the time-mean profiles from the local profiles. The result illustrates which portions of the flow lead or lag the time-mean behavior. In order to establish the local derivative profiles, du/dy and d^2u/dy^2, a quadratic spline of the form $u = Ay^2 + By + C$ was fit to each data point using that central point and the two adjoining data points to establish the three unknowns A, B and C. du/dy and d^2u/dy^2 were then established for the central point by differentiation of the spline-fit curve; thus $du/dy = 2AY + B$ and $d^2u/dy^2 = 2A$ respectively. Since the profiles quantized from the image have a certain degree noise, a linear filter was applied to smooth the curves prior to calculation of the du/dy and d^2u/dy^2 profiles. Because every velocity profile below the region of $Y^+ = 4$ was fit to a linear profile (see discussion in section 2.4), the du/dy and d^2u/dy^2 profiles in that region sometimes display some unusual variations which may be reflective of the fitting and differentiation procedure more than the physics of the flow. Even though the lateral velocities v and w cannot be obtained from the present image-processing procedure, the du/dy profiles are still generally reflective of the local shear stress and the d^2u/dy^2 profiles should be indicative of the inflectional stability of the flow.

To establish the local time derivative of velocity, a quadratic

spline fit of the form $u = Dt^2 + Et + F$ was employed. Local three-point fits are again established which allow the coefficients D, E, and F to be determined. The time derivative, du/dt, is then estalished as 2Dt + E for the central time step. Due to the rather large time step between points ($\Delta t^+ = 2.3$), the du/dt profiles do not yield what appear to be uniformly smooth and continuous curves; however, they do allow at least a general interpretation of local acceleration and deceleration effects.

To establish a property which allows the evaluation of whether VITA detected burst events are of the accelerating or decelerating type (see Johansson and Alfredsson 1982), a property utilizing the short-time variance (VITA) convoluated on the local velocity fluctuation (u') is determined (i.e. VITA*u') to examine whether this property can clarify the detection of the type of burst activity and the flow behavior prior to, during, and following bursting events. The results demonstrate that VITA*u' always becomes negative during the detected burst period, becoming much less negative or even becoming positive upon the termination of the bursting interaction; this character is clearly shown in the following sections.

3.4.2 Representation of Side-View Bursting Behavior

The relationship of burst detections obtained via probe measurements to visually observed patterns or flow structures has been a particularly unsatifactory process because the two types of data have always been taken via separate methods. The present image processing technique allows the correlation between the visual and probe-type detections to be done effectively. However, it must be realized that the patterns, whether visual or probe detected, represent either slices or pointwise detections of more complicated, three-dimensional occurrences. Thus, the expectation is that a typical "burst" event may be detected as one of several types of patterns (see for example, Kline et al. 1971 and Offen and Kline 1975) in either mode of detection. An investigation of the bursting behavior using the present data showed this to clearly be the case, although the types of patterns observed during a burst event were clearly characterizable. The present section reviews the types of patterns that were established with the present data as representative of the bursting process.

Figures 3.12 to 3.19 represent characteristic side-view burst interactions which were selected from the data sequence based on the indication of bursting by the VITA results. Each type of identified burst interaction is represented by profiles of u, u', du/dy, d^2u/dy^2, VITA, VITA*u' and du/dt over a spatial region of $1 < Y^+ < 155$, with a time interval of $\Delta t^+ = 2.3$ between each profile series

and $\Delta t^+ = 4.6$ between each frame of the corresponding visual sequence. The figures demonstrate that a characteristic flow visualization sequence can be related to a sequence of corresponding quantitative profiles. Using the VITA profiles as a detection criteria, a series of typical patterns of bursting behavior are classified and described in the following subsections.

3.4.2.1 Lift-Up Type Burst

A typical lift-up burst visualization sequence is shown in figure 3.12. This is the classic burst sequence described originally by Kim et al. (1971) which is characterized by wall streak migration (see the region around time-line A of the first scene of figure 3.12), streak lift-up from the surface (see the second and third scenes), followed by an oscillation, and ejection downstream (see subsequent scenes), which ends the burst interaction. Note that even though inflectional profiles are observed prior to time-line A, the VITA profiles do not indicate a "burst" occurrence until time-lines B and C, during the initiation of streak oscillation and breakup. Note that the VITA*u' profiles indicate that this detected burst occurs in a region of retarded flow. The du/dy profiles indicate the development of a high shear stress in the region $1 < Y^+ < 30$ upon burst detection; d^2u/dy^2 profiles indicate the development of inflectional velocity profiles just prior to the VITA detected burst ($\Delta t^+ = 7$ to 9). The local profiles of du/dt indicate a rough transition from a locally decelerating flow to an accelerating flow

in the inner region of $30 < Y^+ < 90$ during the development of the detected burst.

Similar lift-up type burst sequences are shown in figures 3.13 and 3.14; note the less violent oscillaton stage in the visual sequences in these figures. The burst detection as indicated by the VITA profiles, differs slighty from figure 3.12, in that the period over which the bursting behavior seems to be detected is of varying length. The other characteristics behave similarly to figure 3.12.

3.4.2.2 Ejection-Sweep Type Burst

Corino and Brodkey (1969) have suggested that the ejection events related to the bursting phenomena initiate in a region $0 < Y^+ < 30$ in which the streamwise velocity is decelerated as much as 50% less than the local mean velocity. They suggest that high-speed fluid entering this region, due to a high sweep event which is propagating from upstream, is the mechanism which stimulates ejections from this region, which are contrued as the burst. Figures 3.15 to 3.16 illustrate an ejection-sweep type burst event similar to those described by Corino and Brodkey.

The visual sequence of figure 3.15(a) shows the development of a decelerated wavy streak (see the first two scenes), which accumulates, and then appears to accelerate (see subsequent two scenes) and eject downstream (last scene). Although the streak

deceleration is not so accentuated, figures 3.15(b) and (c) show a similar type of streak development, with subsequent ejection and sweep behavior occurring near the wall region. For all of the figures, the VITA profiles clearly indicate a burst occurrence for $Y^+ < 50$, with a strong retardation indicated by the VITA profiles. Note also the striking similarity in the du/dt profiles, which demonstrate a sharp acceleration in the near-wall region toward the end of the ejection process, which was suggested by Corino and Brodkey as the entry of high-speed fluid from upstream. Such a sweep event is also suggested by Blackwelder and Eckelmann (1977, 1979) to be caused by a stretched vortex associated with a previous burst from further upstream which imposes a positive pressure gradient on the wall beneath it.

Figure 3.16 is of an ejection-sweep type burst which exhibits very high amplitudes in the VITA profiles, and correspondingly higher VITA*u' responses. The visual sequence shows that a strong flow retardation around $50 < Y^+ < 100$ at $t^+ = 0$ causes a strong streak lift-up followed by a strong acceleration of the accumulated streak as it is swept downstream by a high-speed flow (sweep) from upstream. The u' profile and the visual pictures indicate that the retarded flow lifts up from the wall, moving outward into the region $Y^+ = 100$. The du/dt profiles indicate a strong acceleration in the region $50 < Y^+ < 100$ which develops just after VITA burst detection ($\Delta t^+ = 9$). This type of bursting sequence appears to be similar to

the inrush bursting behavior as discussed by Grass (1971). This inrush (illustrated in the fourth scene of the visual sequence) also occurs about $\Delta t^+ = 8 \sim 9$ after the burst is detected visually (approximately the second visual scene).

3.4.2.3 Roll-Up Type Burst

Figure 3.17 shows a bubble-line pattern indicating a vortex roll-up typical of the development of a hairpin vortex pattern during a burst event. The first scene of the visual sequence shows the lift-up of low-speed fluid from the wall, followed by the development of a strong inflection by the appearance of time-line B. As shown in the second scene, this inflection breaks down into a vortex roll-up, which leads to the formation of a hairpin (the head is visible in the third scene). Following its formation, the hairpin vortex then moves downstream (shown in the third and fourth scenes). Generally, the breakdown of this inflectional velocity profile (illustrated in profile B) has been suggested to result in the generation of hairpins, which move downstream by a combination of induction and convection effects. Examining the VITA profiles, the initial interaction region occurs for $Y^+ < 50$, with the roll-up of the vortex becoming complete about $\Delta t^+ = 9$ after the detection of the inflection in time-line B. Note that, in general, the pattern of a burst behavior developing from a region of retardation, with subsequent acceleration of the flow following bursting, is borne out by the profile data of figure 3.17.

A similar type of roll-up behavior is illustrated in figures 3.18(a) and (b). Although the subsequent visual patterns do not indicate the coherency of figure 3.17, the derived velocity profile characteristics are remarkably similar, varying only in the scale of extent of the behavior. Clearly, the characteristics preceding and following a detected roll-up type burst event are remarkably consistent.

Figure 3.19(a) and (b) illustrate sequences in which the VITA detection appears to be responding to the passage of a large, outer region flow structure which stimulates a low-speed fluid lift-up and burst-like activity in the near-wall region. Note the development of a double peak in the VITA profile, followed by the subsequent acceleration in the near-wall after passage of the large flow structure.

3.4.2.4 Summary

Most reseachers believe that turbulence arises as a consequence of an elevated shear flow, and that the high-shear flow persists as a consequence of the turbulent fluctuations. It is also felt that a cyclic bursting phenomenon is the predominant mode of turbulence production. The bursting phenomena has been described as consisting of the lateral wall migration of low-speed fluid resulting in streak formation, followed by the lift-up, oscillation, and subsequent break up of the low-speed streak. The low-speed streaks lift up

until they penetrate the buffer or the logarithmic layer, which creates an unstable, inflectional velocity profile. Subsequent breakdown of such inflectional profiles is observed in the present study to result in a series of simplified patterns which can be categorized as lift-up, oscillation, and break-up (shown in figures 3.12 to3.14), ejection and sweep behavior (shown in figures 3.15 to 3.16), vortex roll-up (shown in figures 3.17 and 3.19), or a combination of these type of patterns.

Observation of side-view bursting sequences which have been detected by the VITA technique indicates that the local velocity profiles during the initial detection of bursting behavior (such as wall migration, lift-up, or roll-up) are almost always lower than the mean velocity. The results show that a burst almost always originates in a retarded flow region commensurate with a streak lift-up (as suggested by Corino and Brodkey 1969). The evaluation of VITA*u' indicates the degree of flow retardation and bursting strength in one parameter. The du/dt profiles indicate that local acceleration is always observed at the end of a bursting sequence, as a sweep-type event (as suggested by Corino and Brodkey) enters from the upstream. From the present data, it is estimated that the visually detected breakup or breakdown characterizing a bursting event occurs within $\Delta t^+ = 10$ after the local VITA profile indicates a detected burst event.

Note that figures 12 to 19 of instantaneous u, u', du/dy, d^2u/dy^2, VITA, VITA*u', and du/dt profiles determined from image-processed hydrogen bubble flow visualization. Each profile is $\Delta t^+ = 2.3$ apart, and is offest respectively $\Delta u^+ = 7$, $\Delta u'^+ = 7$, $\Delta du^+/dy^+ = 1.5$, $\Delta du+^2/dy+^2 = 0.15$, $k = 1$, $k * \Delta u'^+ = 5$, $\Delta du^+/dt^+ = 1.2$.

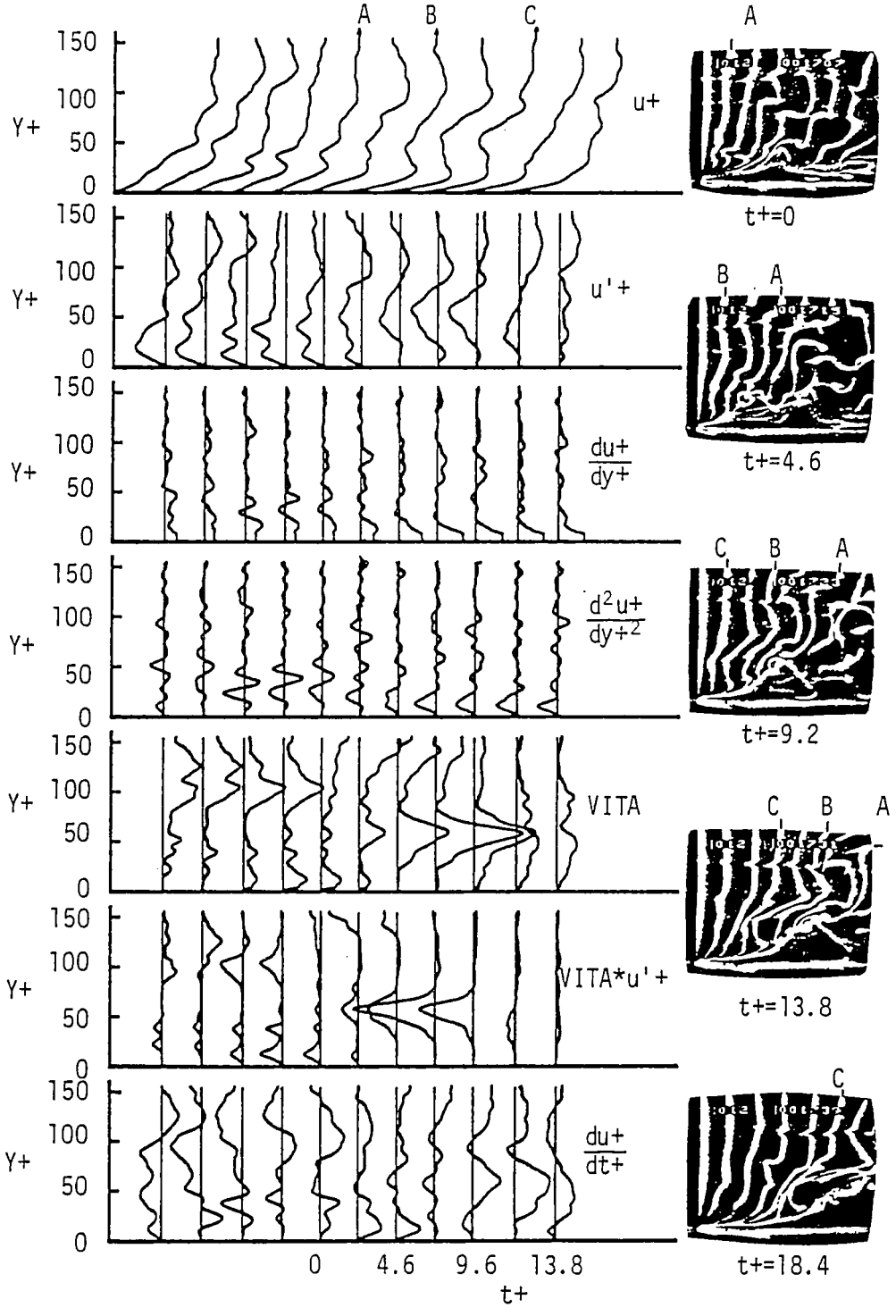

Figure 3.12 Lift-up type burst (t+=0 in figure corresponds to t+=559 in data sequence).

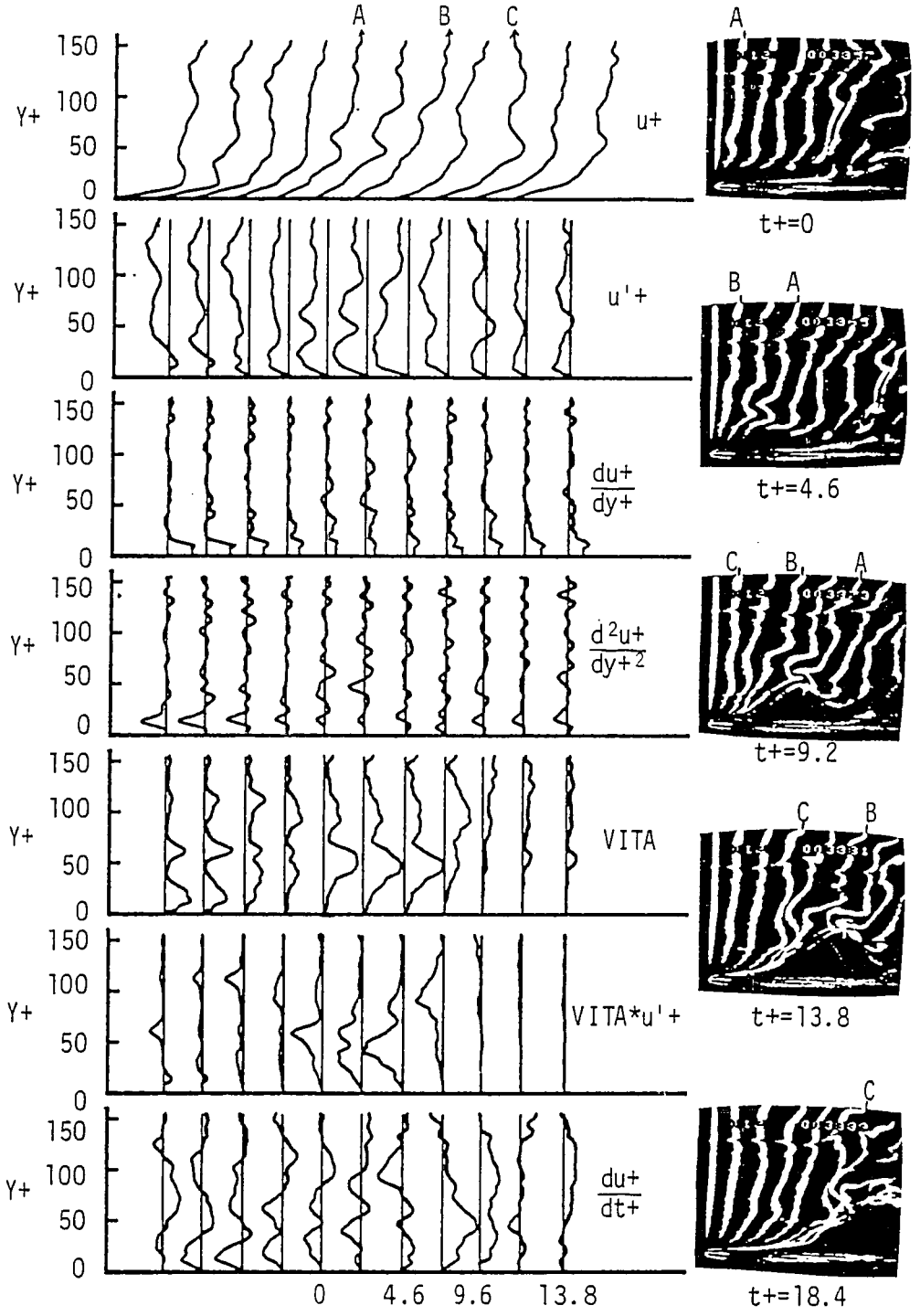

Figure 3.13 Lift-up type burst (t+=0 in figure corresponds to t+=177 in data sequence).

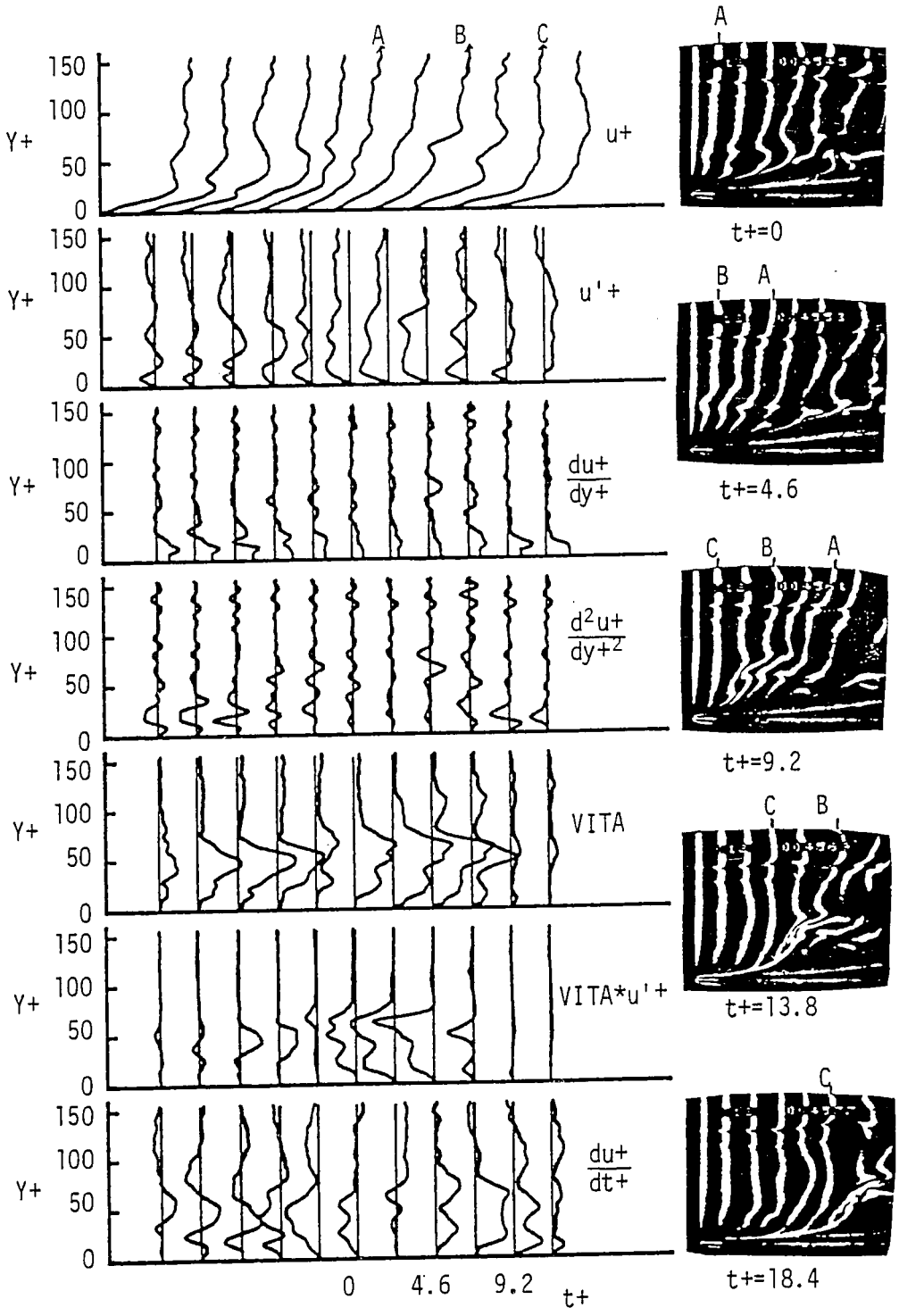

Figure 3.14 Lift-up type burst (t+=0 in figure corresponds t+=2194 in data sequence).

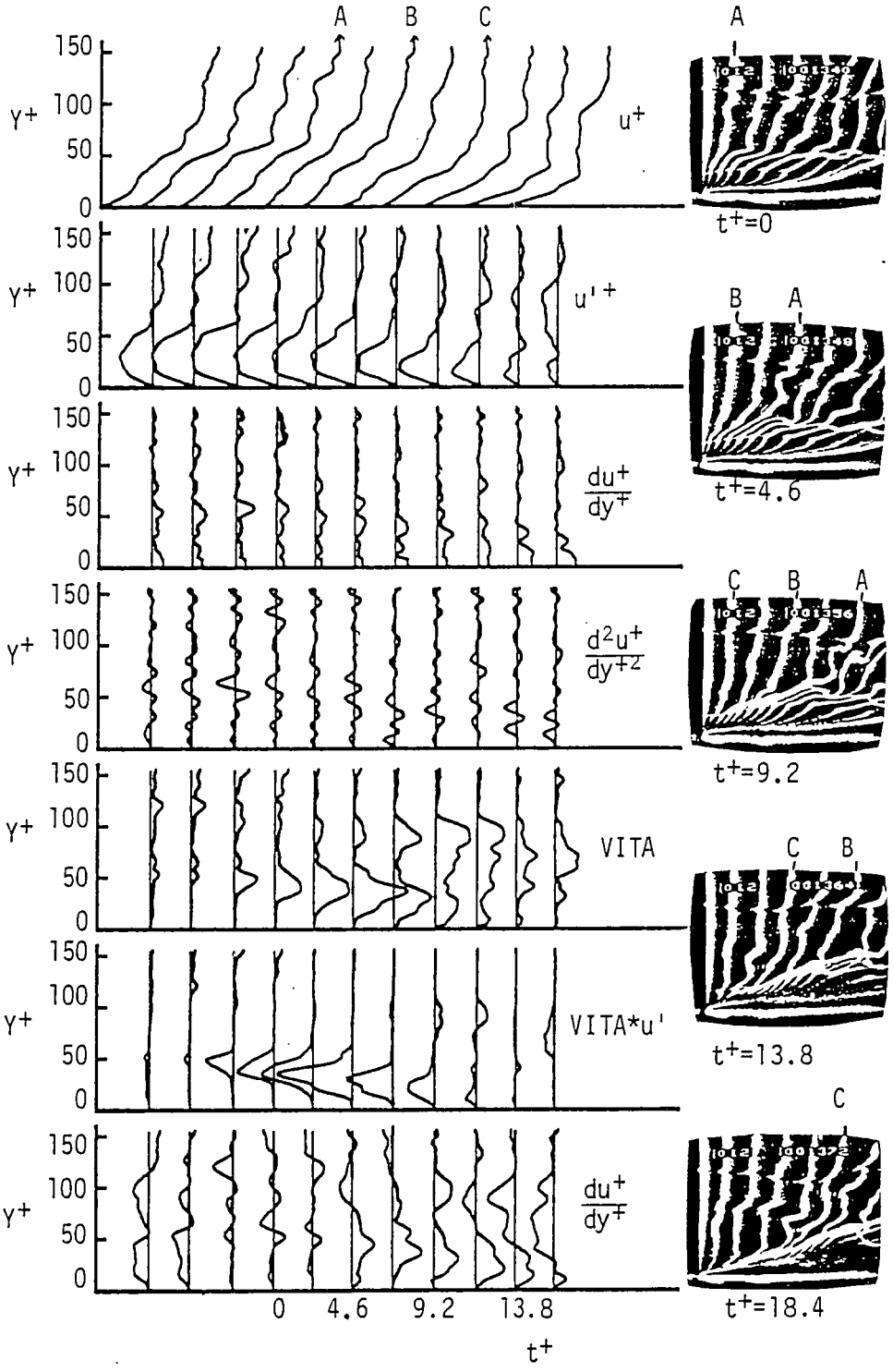

Figure 3.15(a) Ejection-sweep type burst (t^+=0 in figure corresponds to t^+=347 in data sequence).

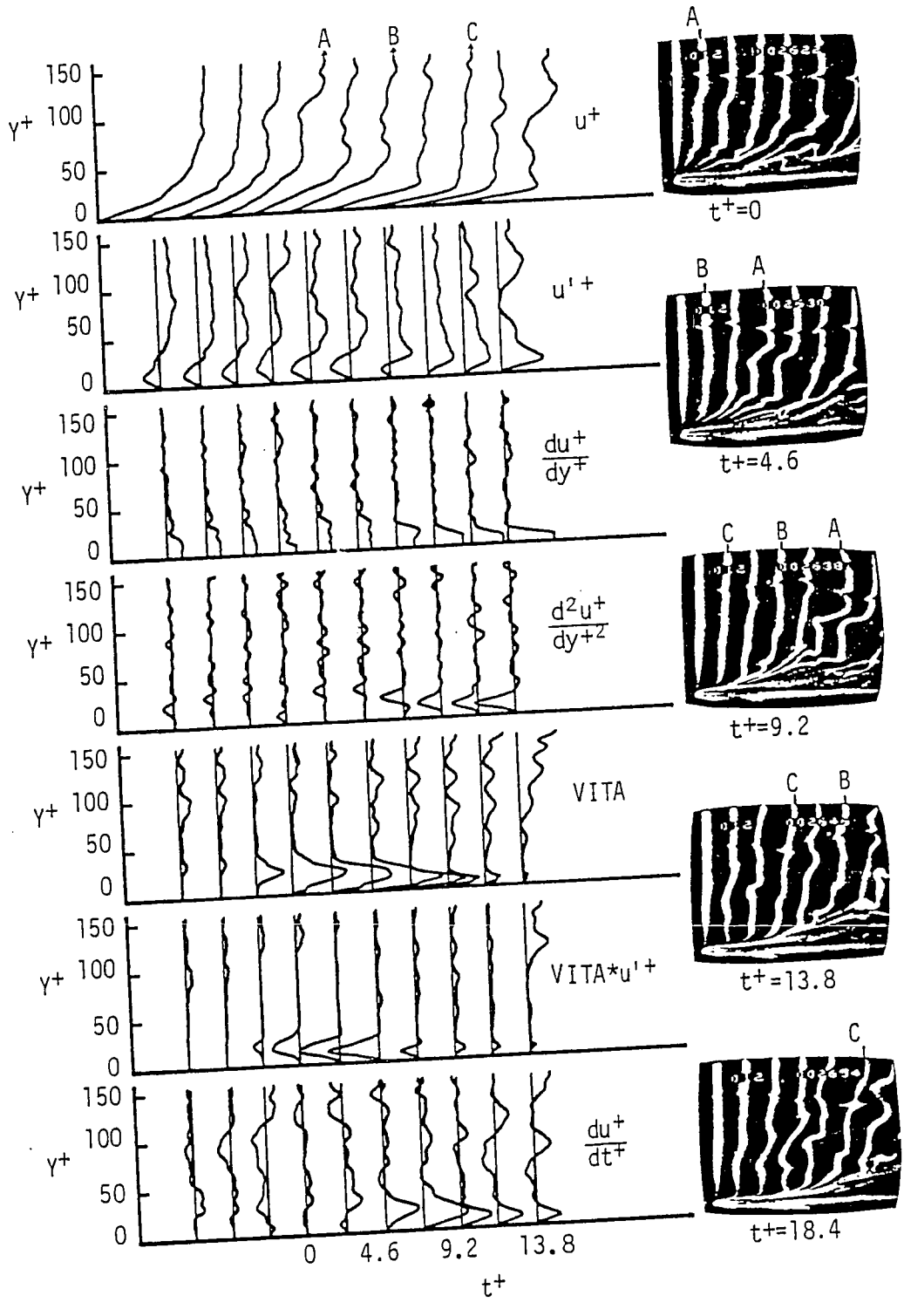

Figure 3.15(b) Ejection-sweep type burst ($t^+=0$ in figure corresponds to $t^+=1086$ in data sequence).

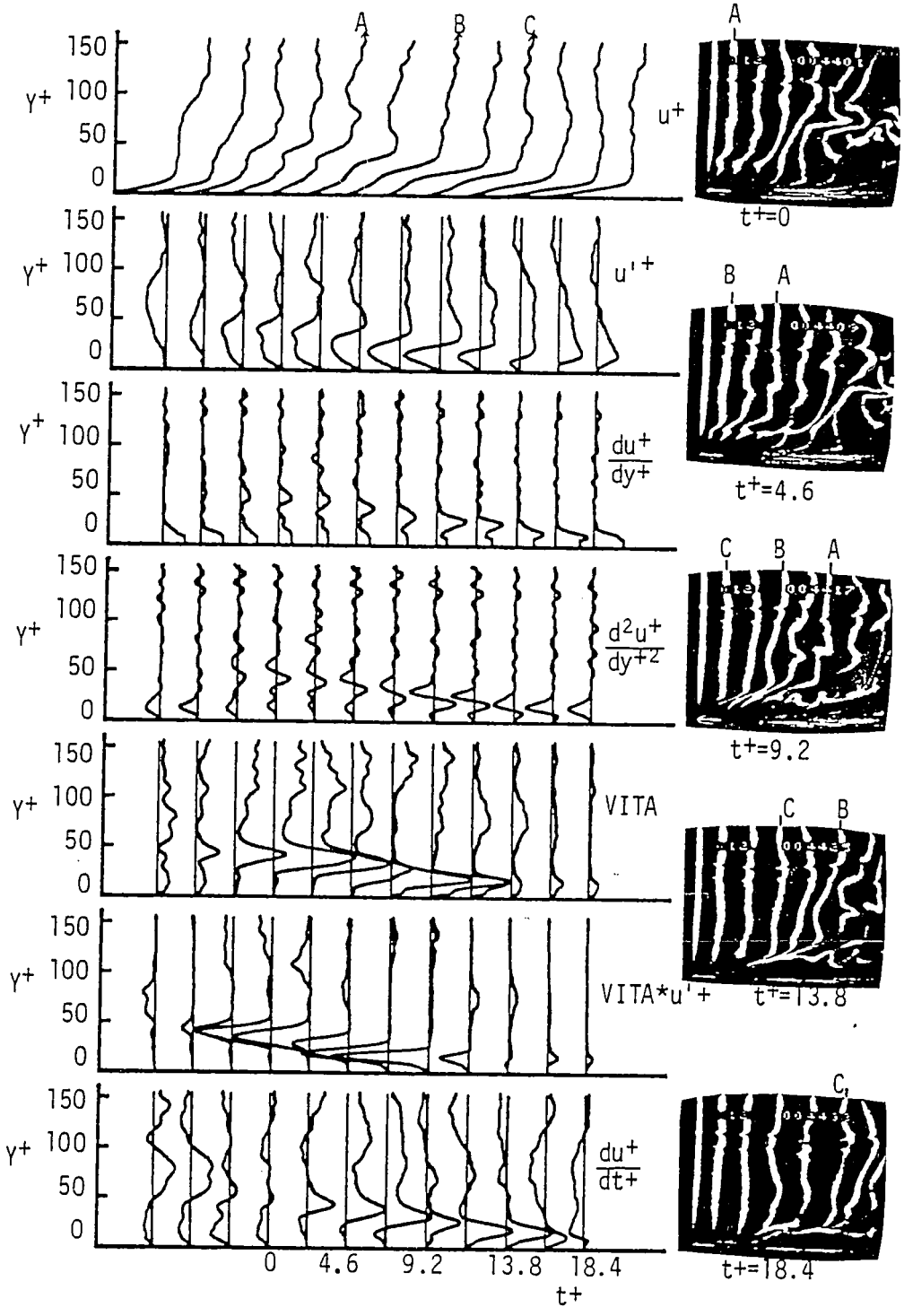

Figure 3.15(c) Ejection-sweep type burst ($t^+=0$ in figure corresponds to $t^+=2111$ in data sequence).

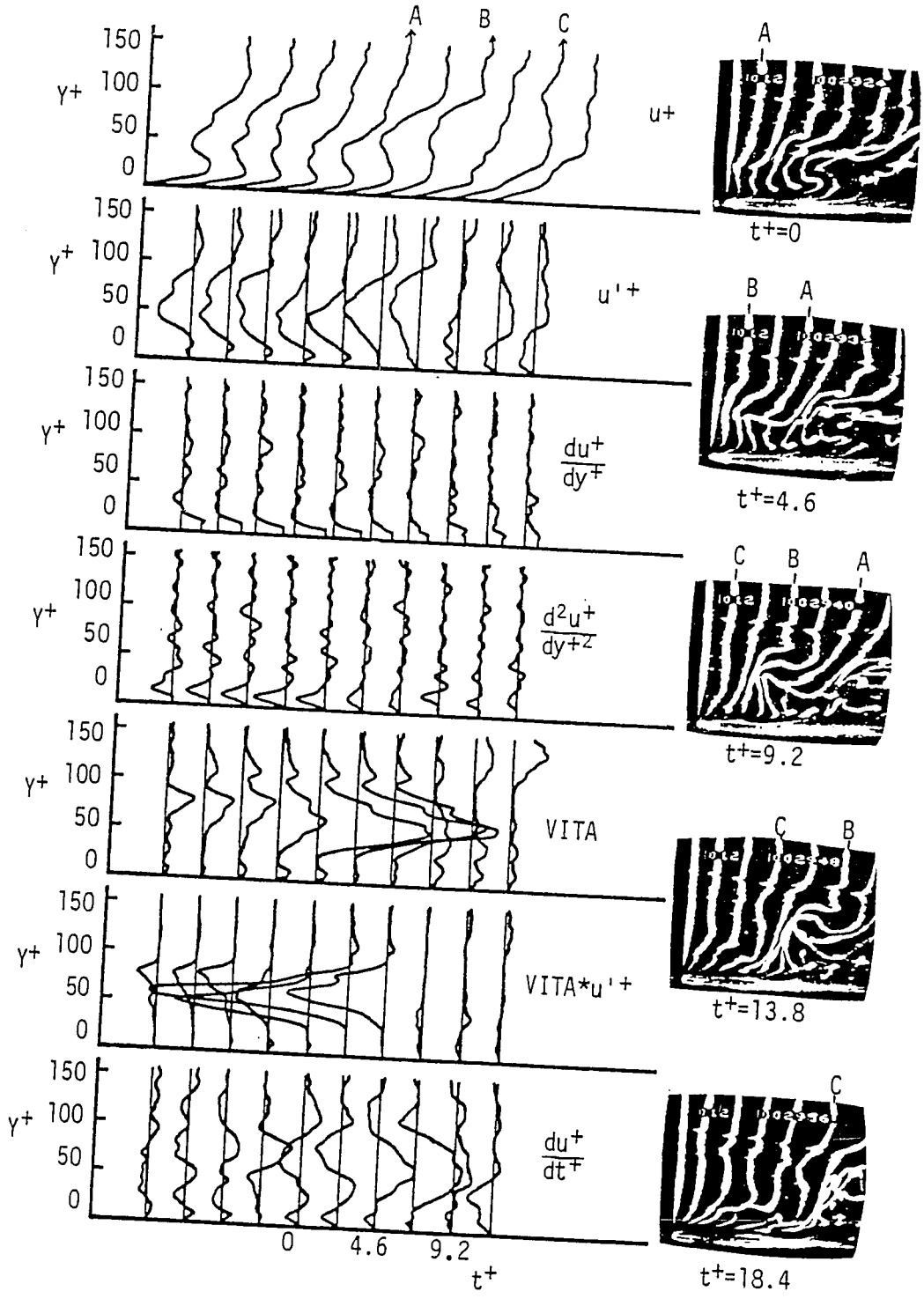

Figure 3.16 Ejection-sweep type burst ($t^+=0$ in figure corresponds to $t^+=1260$ in data sequence).

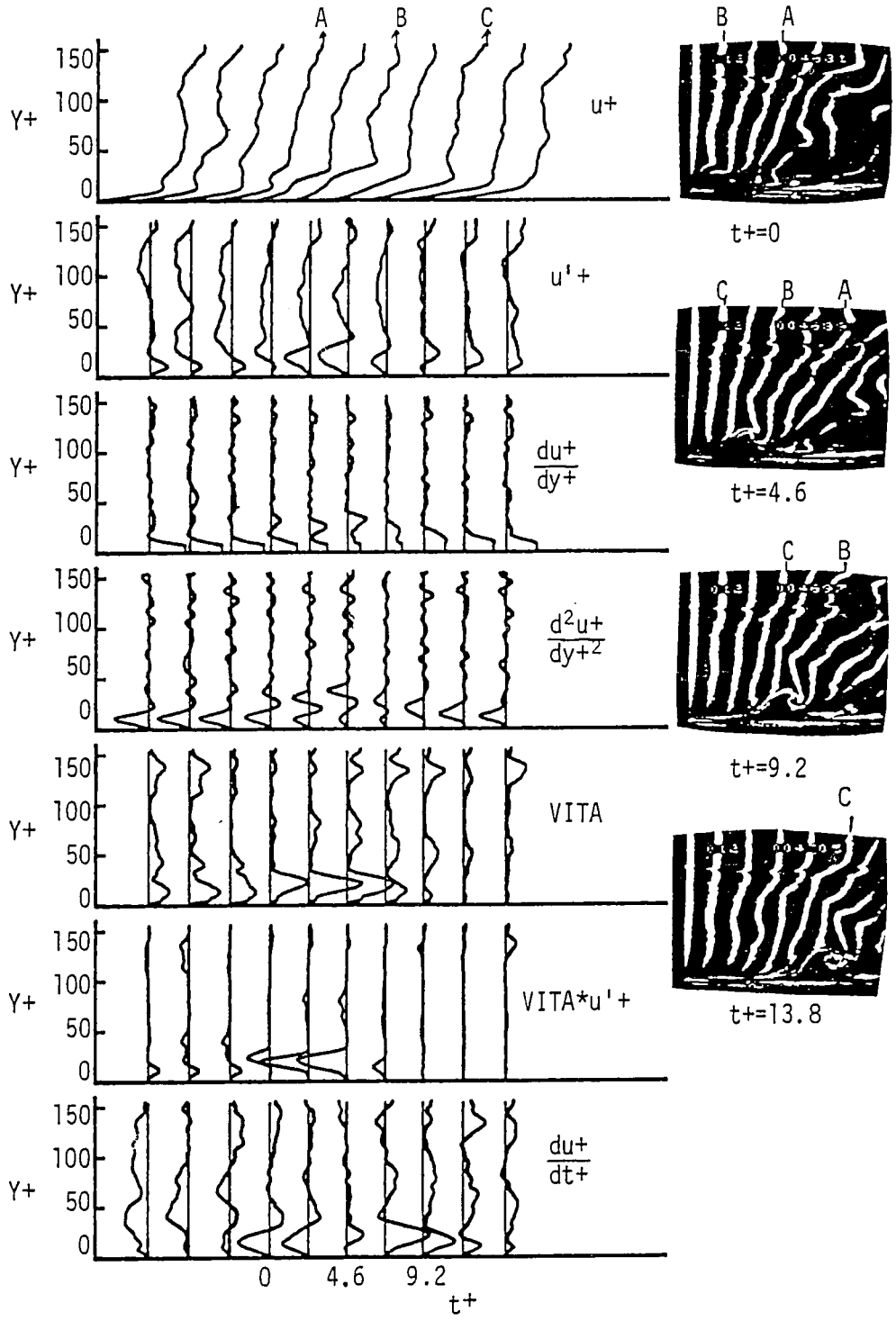

Figure 3.17 Roll-up type burst, generation of a hair-pin type vortex (t^+ in figure corresponds to t+=2272 in data sequence).

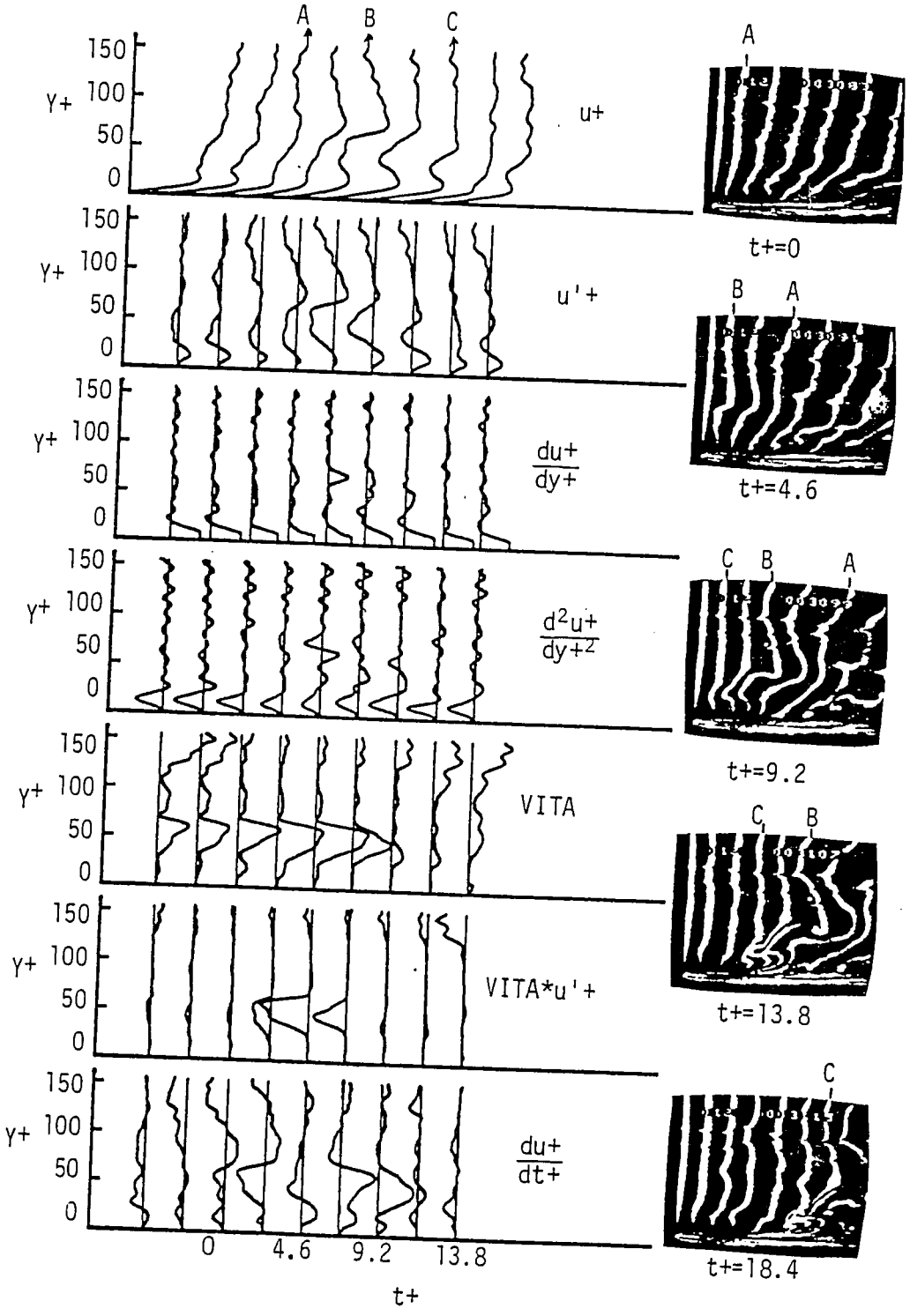

Figure 3.18(a) Roll-up type burst ($t^+=0$ in figure corresponds to $t^+=1352$ in data sequence).

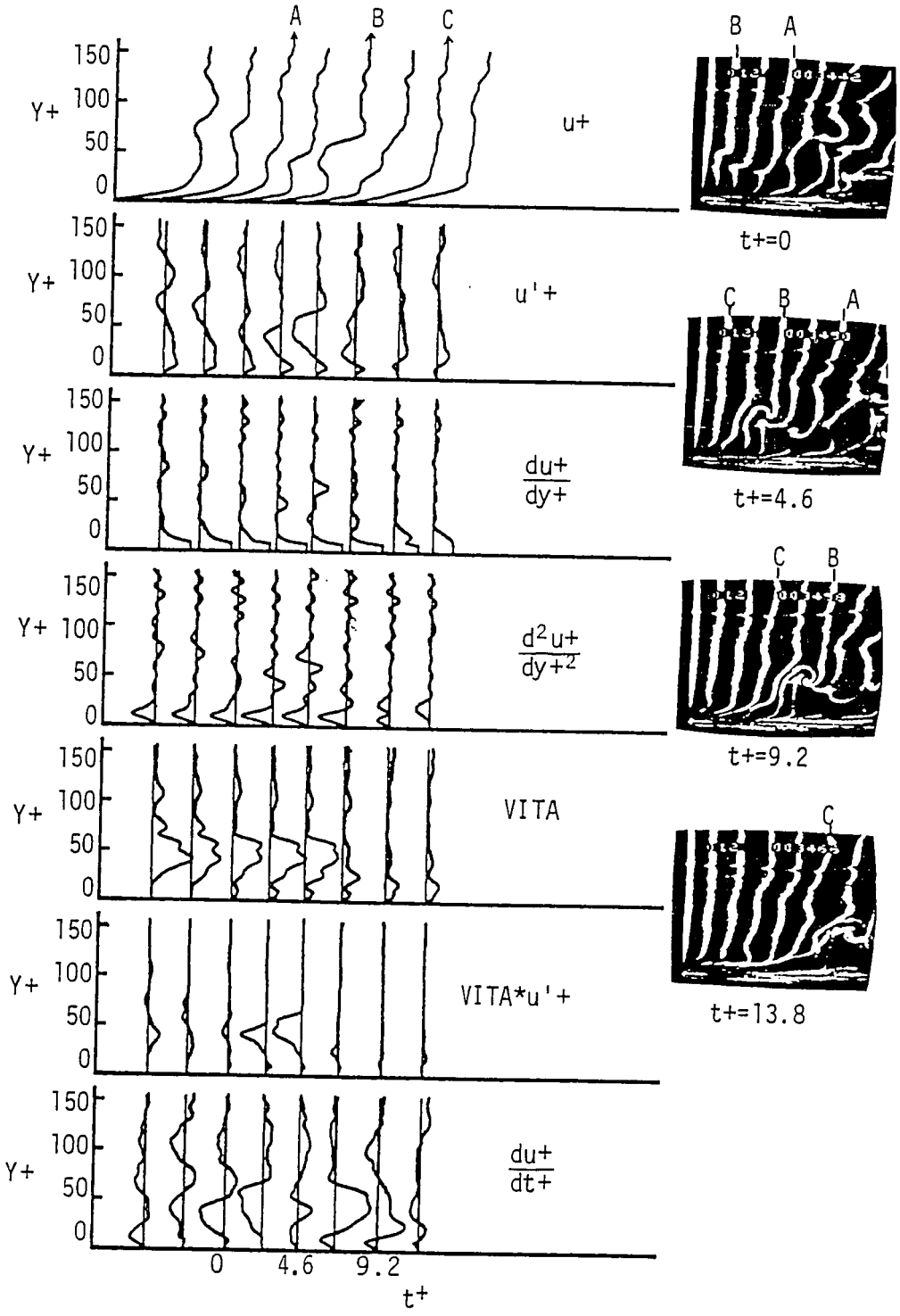

Figure 3.18(b) Roll-up type burst (t+=0 in figure corresponds to t^+=1509 in data sequence).

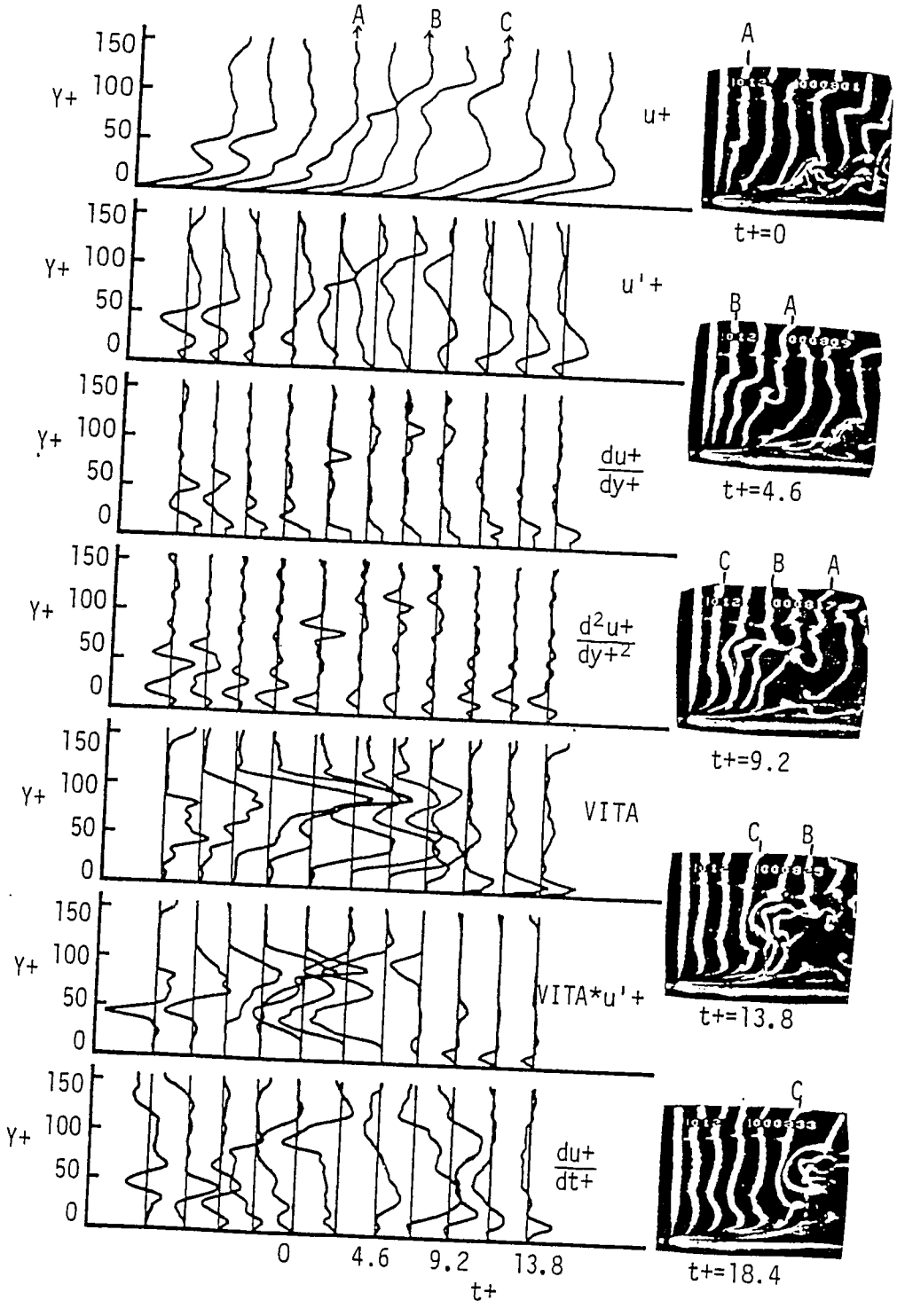

Figure 3.19(a) Large, outer region roll-up type burst (t+=0 in figure corresponds to t+=37 in data sequence).

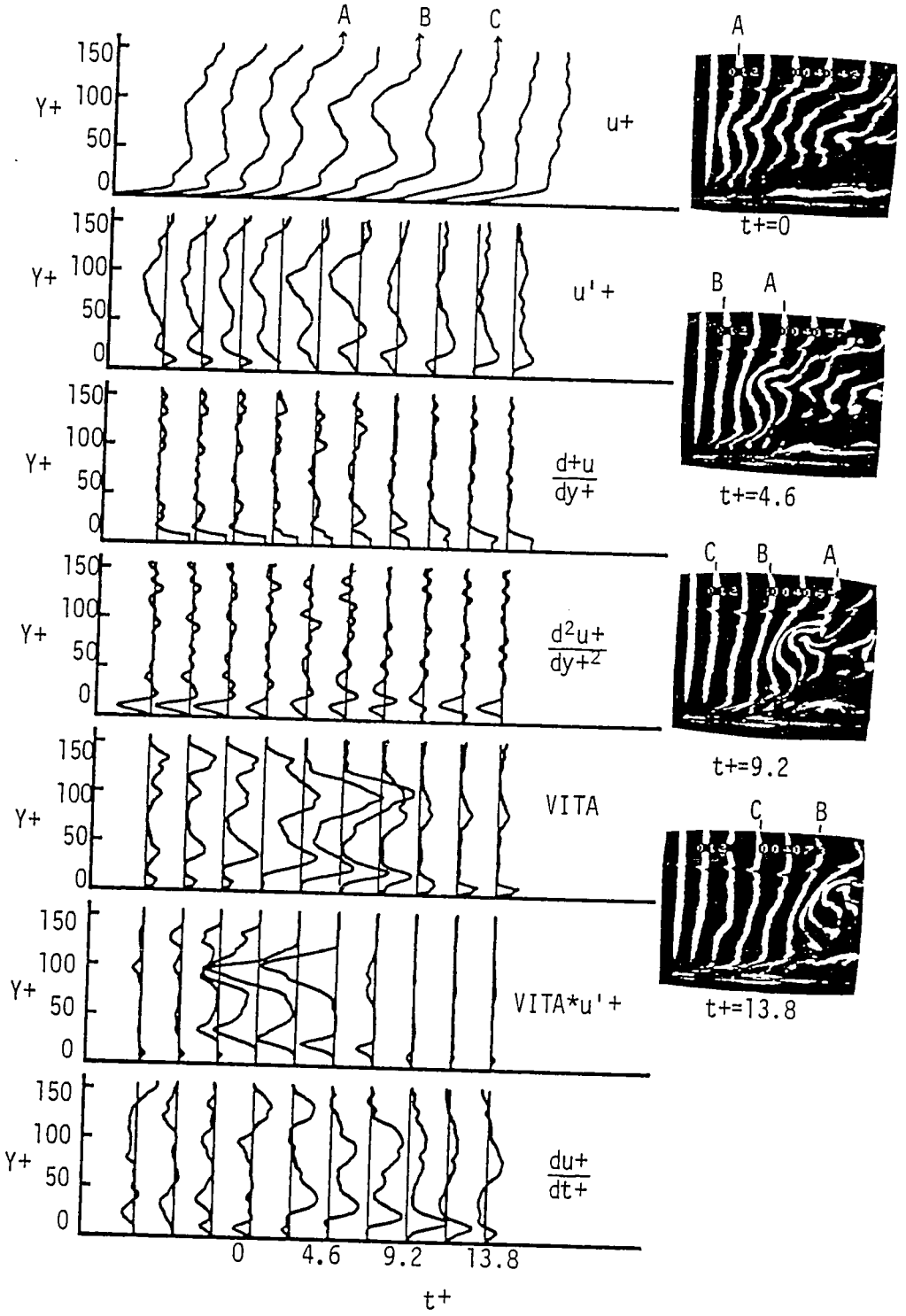

Figure 3.19(b) Large, outer region roll-up type burst (t+=0 in figure corresponds to t+=1909 in data sequence).

4. SUMMARY

The use of automated image processing of hydrogen bubble-line pictures to establish instantaneous velocity profile data has been demonstrated to be feasible and relatively accurate, as indicated by time-averged statistics. The capability for correlating qualitative, visual data with quantitative burst detection techniques appears very promising. Furthermore, the present technique allows the determination of the characteristics of instantaneous profiles of turbulence statistics; these profiles have been demonstrated to be quite useful in characterizing the coherent flow behavior of the turbulent bursting phenomena.

Clearly it is desirable to expand the present system of image analysis to time-streak markers in order to yield combined u and v velocity, such as was done manually by Kim et al. (1971) and Grass (1971). However, the use of time-streak markers presents several problems, not the least being the effective creation of the markers themselves without significant interference with the flow. Work is continuing in an effort to adapt the present technique for use with time-streak marker visualization, as well as to accelerate the present process of data acquisition.

REFERENCES

Abernathy, F.H., Bertschy, J.R. and Chin, R.W., 1977, "Turbulent Spectra Using Laser-Doppler Anemometry andSelective Seeding", Pro. of 5th Symp. on Turb., G.K. Patterson and J.L. Zakin, eds., Univ. Missour-Rolla, P133.

Acarlar, M.S. and Smith, C.R., 1984, "An Experimental Study of Hairpin-Type Vortices as A Potential Flow Structure of Turbulent Boundary Layers", Report FM-5, Dept. of Mech. Engrg. and Mech., Lehigh University.

Ballard, D.H. and Brown, C.M., 1982, Computer Vision, Prentice-hall , New York.

Balint, J.L., Ayraut, M. and Schon, J.P., 1983, "Quatitative investigation of the velocity and concentration fields of turbulent flow combining visualization and image processing", 3rd Int. Symp. on Flow Visualization, W.J. Yang et al., eds., Univ. Michigan, p315.

Blackwelder, R.F. and Eckelmann, H., 1979, "Streamwise Vortices Associated with the Bursting Phenomenon", J. Fluid Mech., Vol. 94, p577.

Blackwelder, R.F. and Kaplan, R.E., 1976, "On the Wall Structure of the Turbulent Boundary Layer", J. Fluid Mech., Vol. 76, p98.

Blackwelder, R.F. and Eckelmann, H., 1979, "Streamwise Vortices Associated with Bursting Phenomenon", J. Fluid Mech., Vol. 94, p577.

Blackwelder, R.F. and Harilonidis, J.H., 1983, "Scaling of the Bursting Frequency in Turbulent Boundary Layers", J. Fluid Mech., Vol. 132, p87.

Bloklond, R. and Prasad, K.K., 1983, "Some Visualization Studies on Turbulent Boundary Layer Using Multi-Wire Hydrogen Bubble Generation", Pro. of 8th Symp. on Turb., J.L. Zakin and G.K. Patterson, eds., Univ. Missour-Rolla, p5.

Bradshaw, P., 1971, An Instroduction to Turbulence and its Measurement, Pergamon Press.

Chang, T. and Tatterson G., 1983, "An Automated Analysis Method for Complex Three Dimensional Mean Flow Fields", 3rd Int. Symp. on Flow Visualization, W.J. Yang et al., eds., Univ. Michigan, p266.

Cornelius, K., Takenchi, K. and Deutsch, S., 1977, Turbulent Flow Visualization : A Technique for Extracting Accurate Quantitative

information", Pro. of 5th Symp. on Turb., J.L. Zakin and G.K. Patterson, eds., Univ. Missour-Rolla, p287.

Clauser, F.H., 1956, "The Turbulent Boundary Layer", Adv. Appl. Mech., Vol. 4, p1.

Coles, D.E., 1956, "The Law of the Wake in the Turbulent Boundary Layer", J. Fluid Mech., Vol. 1, p191.

Corino, E.R. and Brodkey, R.S., 1969, "A Visual Investigation of the Wall Region in Turbulent Flow", J. Fluid Mech., Vol. 37, p1.

Davis, W. and Fox, R.W., 1966, "An Evaluation of the Hydrogen Bubble Technique for the Quantitative Determination of the Fluid Velocities Within Clear Tubes", ASME Paper No. 66-WA/FE-21.

Falco, R.E., Chu, C.C. and Wiggert, D.C., 1985, "Experimental Determination of Drag Modifications Due to Elastic Compliant Surfaces Using Quantitative Visual Techniques", Pro. of 9th Symp. on Turb., X.B. Reed et al., eds., Univ. Missour-Rolla, p42.

Grass, A.J., 1971, "Structure Features of Turbulent Flow Over Smooth and Rough Boundaries", J. Fluid Mech., Vol. 50, p233.

Hall, E.L., 1979, Computer Image Processing and Recognition, Academic Press, New York.

Head, M.R. and Bandyopadhyay P., 1982, "New Aspects of Turbulent Boundary-Layer Structure", J. Fluid Mech., Vol. 107, p297.

Hinze, J.O., 1975, Turbulence, McGraw-Hill.

Johansen, J.B. and Smith, C.R., 1983, " The Effects of Cylindrical Surface Modifications on Turbulent Bounday Layers", Report FM-3, Dept. of Mech. Engrg. and Mech., Lehigh University.

Johanson, A.V. and Alfredsson, P.H., 1982, "On the Structure of Turbulent Channel Flow", J. Fluid Mech., Vol. 122, p295.

Johanson, A.V. and Alfredsson, P.H., 1982, "On the Detection of Turbulence Generating Events", Experimental Studies of Turbulent Channel Flow, paper IV, Dep. of Mech., the Royal Institute of Technology, S-100 44 Stockholm, Sweden.

Kim, H.T., Reynolds, W.C., Schraub, F.A. and Runsladler, P.W., 1967, "The Structure of Turbulent Boundary Layers", J. Fluid Mech., Vol. 30, p741.

Kim, H.T., Kline, S.J. and Reynolds, W.C., 1971, "The Production of Turbulence Near a Smooth Wall in a Turbulent Boundary Layer", J. Fluid Mech., Vol. 50, p133.

Klebanoff, P.S., Schubauer, G.B. and Tidstrom, K.D., 1955, "Measurements of the Effect of Two-Dimensional and Three-Dimensional Roughness Elements on Boundary-Layer Transition", J. Aeronautical Scinces, 22, No. 11, p803.

Kreplin, H.P. and Eckelmann, H., 1979, "Propagation of Perturbations in the Viscous Sublayer and Adjacent Wall Region", J. Fluid Mech., Vol. 95, p305.

Kline, S.J., Reynolds, W.C., Schraub, F.A. and Runstadler, P.W., 1967, "The Structure of Turbulent Boundary Layers", J. Fluid Mech., Vol. 30, p741.

Kunen, J.M.G., Ooms, G. and Vink, P.J.J., 1983, "On Detection Methods for Coherent Structures in Turbulent Flows", Pro. of 8th Symp. on Turb., J.L. Zakin and G.K. Patterson, eds., Univ. Missour-Rolla, p4.

Landanl, M.T., 1983, "Theoretical Modelling of Cherent Structures in Wall-Bounded Shear Flows", Pro. of 8th Symp. on Turb., J.L. Zakin and G.K. Patterson, eds., Univ. Missour-Rolla, p1.

Lu, L.J. and Smith, C.R., 1985, "Image Processing of Hydrogen Bubble Flow Visualization for Determination of Turbulence Statistics and Bursting Characteristics", to appear in Exp. in Fluids.

Nakagawa, H. and Nezu, I., 1981, "Structure of Space-Time Correlations of Bursting Phenomena in an Open-Channel Flow", J. Fluid Mech., Vol. 104, p1.

Offen, G.R. and Kline, S.J., 1975, "A Proposed Model of the Bursting Process in Turbulent Boundary Layers", J. Fluid Mech., Vol. 70, p209.

Purtell, L.P., Klebanoff, P.S. and Buckley F.T., 1981, "Turbulent Boundary Layer at Low Reynolds Number", Vol. 24, p802.

Rabiner, L.R. and Schafer, R.W., 1978, Digital Processing of Speech Signals, Prentice-Hall.

Rajagopalan, S. and Antonia, R.A., 1982, "Use of a Quadrant Analysis Techanique to Identify Coherent Structures in a Turbulent Boundary Layer", Phys. Fluids, Vol. 25, p949.

Rao, K.N., Narasimha, R. and Narayanan, M.A.B., 1971, "The 'Bursting' Phenomenon in a Turbulent Boundary Layer", J. Fluid Mech. , Vol. 48, p339.

Rosenfeld, A. and Kak, A.C., 1976, Digital Picture Processing, Academic Press, New York.

Schlichting, H., 1979, Boundary Layer Theory, McGraw-Hill, New York.

Schraub, F.A., Kline, S.J., Henry, J., Runstadler, P.W., JR. and Littell, A., 1965, "Use of Hydrogen Bubbles for Quantitative Determination of Time-Dependent Velocity Fields in Low-Speed Water Flows", J. of Basic Engng., Trans. ASME, 87, p429.

Shimizu, I., Yasuda, Y., Emori, Y., and Yang, W.J., 1983, "Quantitative Visualization of Jet Sprays by a Bi-directional Light-Scattering Image Processing Method", 3rd Int. Symp. on Flow Visualization, W.J. Yanget al., eds., Univ. Michigan, p358.

Smith, C.R., 1983, "A Synthesized Model of the Near-Wall Behavior in Turbulent Boundary Layers", Pro. 8th Symp. on Turbulence, Univ. of Missouri-Rolla, J.L. Zakin and G.K. Patterson, eds., p35.

Smith, C.R. and Abbott, P.E., eds., 1978, Coherent Structure of Turbulent Boundary Layers, Lehigh University.

Smith, C.R. and Metzler, S.P., 1983, "The Characteristics of Low-Speed Streaks in the Near-Wall Region of Turbulent Boundary Layer", J. Fluid Mech., Vol. 129, p27.

Smith, C.R. and Schwartz, S.P., 1983, "Observation of Streamwise Vortices in Near-Wall region of a Turbulent Boundary layer", Phy. of Fluids 26; 3 p641.

Smith, R.E., Jr., Speray, D.E. and Everton, E.L., 1983, "Visualization of Computer-Generated Flow Fields", 3rd Int. Symp. on Flow Visualization, W.J. Yang et al., eds., Univ. Michigan, p655.

Smith, C.R. and Paxson, R.D., 1983, "A Technique for Evaluation of Three-Dimensional Behavior in Turbulent Boundary Layers Using Computer Augmented Hydrogen Bubble- Wire Flow Visualization", Exp. in Fluids 1, p43.

Tennekes, H. and Lumley, J.L., 1971, A First Course in Turbulence, M.I.T. Press.

Wallace, J.M., Brodkey, R.S. and Eckelmann, H., 1977, "Pattern-Recognized Structures in Bounded Turbulent Shear Flows", J. Fluid

Mech., Vol. 83, p673.

White, F.M., 1974, Viscous Fluid Flow, McGraw-Hill, Inc. New York.

Appendix A. Digitization Users Guide

A.1. Introduction

The digitization work was excuted by interfacing the video system to a VAX 11/780 computer system via a Model 270 A Video Digiter. The digitization and computer system are located in the CAD/CAM Reserach Laboratory of Lehigh University. The interface control software was originally developed by Dave Evens and subsequently improved by the author.

A.2. Required Programs for Digitization

Several programs and commands have been written to excute the digitization processes, including : digitization, image display, and image storage. The digitization and display programs, named GRAB and DISP respectively, are written in MACRO-machine language (i.e. high-level language) to reduce the computer time below that required by low-level languages such as FORTRAN or BASIC. A main control program, named MASTER, is written in command-type system language and incorporates : a storage program function, the GRAB program, and the DISP program. The MASTER program also includes a series of assistance instructions to help the operator in excuting the digitization processs.

A.3. Digitization Procedure (refer to figure 2.4)

Step 1. Connect the INSTAR video recorder to the digitizer via four labeled cables, connecting the video input, display output H blanking, and FS location on each device directly to corresponding connector on the other.

Step 2. Place the digitizer in "set-up" mode.

(a). Turn digitizer power switch on (push to light).

(b). Place "Mode" switch in the "set-up" position.

(c). Place "Display" switch in the "on" position.

(d). Place "Cursor" switch in the "line" position.

Step 3. Turn on the video recorder; place the video display in the stand-by mode, displaying the gray-level test Pattern.

Step 4. Calibrate the intensity output for the scene(s) to be viewed.

(a). Use the "set up position" knob to locate the cursor such that the extremes of the picture to be viewed are displayed; the wave-form distribution of the intensity distribution will be indicated on the right side of screen.

(b). Use the "black level" and "video amplitude" knobs to

establish a suitable gray-level condition.

(Note that the optimum intensity range will give an intensity amplitude for the dark portions of a picture of essentially zero intensity, with the brightness intensity range set as high as possible.)

Step 5. Prepare to digitize :

(a). Change "Mode" switch to "run" position.

(b). Change "Display" switch to "off" position.

(c). Place "Cursor" switch in either "dot" or "line" position.

Step 6. Digitize the picture to the computer.

(a). Display the scene to be digitized, setting the video recorder to the slow-motion mode. Slow down the sequence speed to picture-by-picture until picture to be digitized appears.

(b). "Freeze" picture by pushing single-frame button on video recorder.

(c). Run the MASTER control program written in the system command language, following the instructions step by step.

(d). Relase single-frame button and proceed to the next frame to be digitized.

(Note that the instructions which appear on the computer display screen will direct the operator to run the GRAB program for digitizing, to run the DISP program for image re-display on the VAX 11/780 color terminal, and to store the numerical array of the picture image on disk.)

Appendix B. Uncertainty Analysis of Result

B.1. Introduction

Errors arising from limitations of the experimantal techniques, such as in the determination of a scale factor from the video screen, or in the quantification of the video image can be estimated using statistical methods for uncertainty estimation.

The uncertainty in numerical quantities due to the finiteness of a data sample is estimated by a confidence interval at a specified significance level. The total uncertainty W_R in an experimental result $R = R(V_1, V_2, \ldots, V_N)$ may be calculated (Kline and McClintock (1953)) by using the relation :

$$W_R = [\ (\frac{dR}{dV_1} W_1)^2 + (\frac{dR}{dV_2} W_2)^2 + \ldots + (\frac{dR}{dV_n} W_n)^2\ ]^{1/2}$$

where $W_1, W_2, \ldots, W_n$ are the uncertainty intervals in $V_1, V_2, \ldots, V_n$ for a certain estimated level of confidence, generally 95%. $V_1, V_2, \ldots, V_n$ must be independent and their statistical distributions must have only a single peak.

Schraub et al. (1964) gives a detailed uncertainty analysis for a single velocity determination by the hydrogen-bubble method. Using that work as a guide, a simplified and estimated analysis was made

for the various measured and calculated data of the present study; the results are summarized below.

B.2. Uncertainty in Experimental Results

In general, all results are based on length and time measurements for a selected frame of data from a video sequence. Measurements were take from the digitized image which represent the video frame as a finite pixel matrix. All uncertainties discussed in this section consider only the velocity derived from the hydrogen bubble-line images and neglect the effects of the correction for the velocity defect generated by the hydrogen bubble generating wire.

B.2.1. Uncertainty in Velocity Measurement

The instantaneous velocity can be expressed as

$$U_i = \frac{\Delta xi}{\Delta ti} * \frac{1}{s}$$

where U_i is the estimate of the x-component of the actual local Eulerian field velocity and is a temporal and spatial average taken during the short-time interval, Δti,

Δxi : the horizontal displacement between the two bubble time-lines nearest to the generating wire

Δti : the bubble-pulse period (1/30 sec)

s : scale factor coverting displacement in the video picture, Δxi, to the true displacement.

(a) Time Calibration Uncertainty

Time measurements are based on the video framing rate and the bubble-line generation frequency, 30 frames per second. The estimated value of $W_{\Delta ti}$ is ti*2/1012 for the present study. The uncertainty for the framing rate was

$$\frac{W_{\Delta ti}}{\Delta ti} = \pm 0.2\% \quad (95\% \text{ confidence})$$

and was assumed to be negligible.

(b). Scale Calibration Uncertainty

The scale transformation from the video picture to the true scale was established from a ruler image taken (see figure B.1) as a reference at the same physical location. The calibration indicated a conversion scale of 57 pixels per centimeter in the x direction. The uncertainty in scale calibration was determined as :

$$\frac{Ws}{s} = \pm (1/57 * 100\%) = \pm 1.7\% \quad (95\% \text{ confidence})$$

(c) Uncertainty in X-component Measurement

Δxi was obtained by taking the differential distance between two bubble lines, where $\Delta xi = xi - xo$. Thus, the value of $W_{\Delta xi}$ was approximated as $W_{\Delta xi} = (W_{xi}^2 + W_{xo}^2)^{1/2}$ where W_{xi} and W_{xo} for the

present study were assumed to be ± 1 pixel for the image. The uncertainty of x-component change can be estimated as

$$\frac{W_{\Delta xi}}{\Delta xi} = \left[\left(\frac{W_{xi}}{\Delta xi} \right)^2 + \left(\frac{W_{xo}}{\Delta xi} \right)^2 \right]^{1/2}$$

$$= \pm 4.7\% \text{ of } \Delta xi = 30 \text{ pixel at } Y^+ = 100 \text{ (95\% confidence)}$$

$$= \pm 30\% \text{ of } \Delta xi = 5 \text{ pixel, near the wall}$$

Since the mean value of $\Delta\bar{x}$ is given by the equation,

$$\Delta\bar{x} = \frac{1}{N} \sum_{1}^{N} \Delta xi ,$$

the uncertainty in the mean value of $\Delta\bar{x}$ is estimated as

$$\frac{W_{\Delta\bar{x}}}{\Delta\bar{x}} = \left\{ \frac{\frac{1}{N} \sum_{1}^{N} W_{\Delta xi}^{\,2}}{\left(\frac{1}{N} \sum_{1}^{N} \Delta xi \right)^2} \right\}^{1/2} = \frac{\left(N \sum_{1}^{N} W_{\Delta xi}^{\,2} \right)^{1/2}}{\sum_{1}^{N} \Delta xi}$$

$$\simeq \pm 0.21\% \text{ at } Y^+ = 100$$

$$\simeq \pm 3\% \text{ at } Y^+ = 2$$

B.2.2 Uncertainty in Turbulence Intensity, Skewness, and Flateness

Because most of values of skewness fall near zero, the uncertainty of the skewness normalized on the absoulate value of the corresponding skewness loses its physical sense. A similar argument can be made for the flatness and turbulence intensity as well. Thus, to represent the uncertainty of the mean data, which yields a phyical

appreciation, the three higher moments are normalized on an appropriate fixed property and the results plotted graphically in conjunction with the corresponding mean property; the dimensional uncertainty of turbulence intensity ($Urms = \sqrt{\overline{u'^2}}$) is normalized on U_τ (see figure 3.4), the skewness is normalized with respect to $Urms^3$ (see figure 3.5), and the flatness is normalized with respect to $Urms^4$ (see figure 3.6). The uncertainties of these higher moments are evaluated as follows :

(1). Uncertainty of turbulence intensity

$$Urms = \sqrt{\overline{u'^2}} = \left[\frac{1}{N} \sum_{1}^{N} (ui - \bar{u})^2 \right]^{1/2}$$

$$W_{Urms} = \left\{ \frac{\left(\frac{2}{N\Delta ti^2 s^2}\right)^2 \sum_{1}^{N} (\Delta xi - \Delta\bar{x})^2 (W_{\Delta xi}^2 + W_{\Delta\bar{x}}^2)}{\left(\frac{1}{N\Delta ti^2 s^2}\right) \sum_{1}^{N} (\Delta xi - \Delta\bar{x})^2} \right\}^{1/2}$$

$$W_{Urms} / U_\tau = \pm 3\% \quad \text{at} \quad Y^+ = 100$$

(see figure B.2)

(2). Uncertainty of skewness

$$\overline{u'^3} = \frac{1}{N} \sum_{1}^{N} (ui - \bar{u})^3$$

$$W_{\overline{u'^3}} = \left\{ \left(\frac{3}{N\Delta ti^3 s^3}\right)^2 \sum_{1}^{N} (\Delta xi - \Delta\bar{x})^4 (W_{\Delta xi}^2 + W_{\Delta\bar{x}}^2) \right\}^{1/2}$$

$$W_{\overline{u'^3}} / \overline{u'^3} = \pm 8\% \quad \text{at} \quad Y^+ = 100$$

(see figure B.3)

(3). Uncertainty of flatness

$$\overline{u'^4} = \frac{1}{N}\sum_{1}^{N}(ui - \bar{u})^4$$

$$W_{\overline{u'^4}} = \left\{\left(\frac{4}{N\Delta ti^4 s^4}\right)^2 \sum_{1}^{N} (\Delta xi - \Delta\bar{x})^6 (W_{\Delta xi}{}^2 + W_{\Delta\bar{x}}{}^2)\right\}^{1/2}$$

$$W_{\overline{u'^4}} \,/\, \overline{u'^4} = \pm 18\% \quad \text{at} \quad Y^+ = 100$$

(see figure B.4)

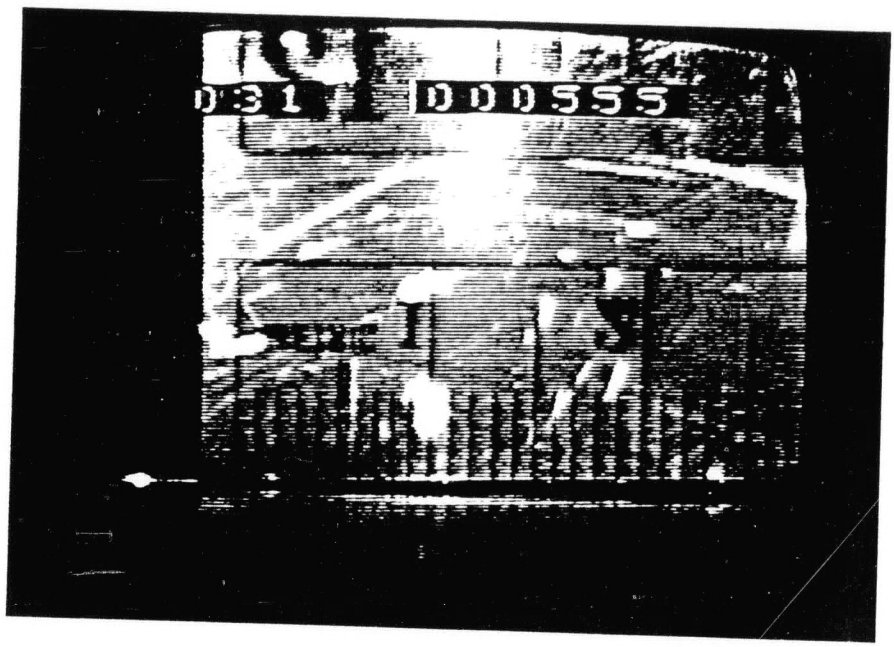

Figure B.1 Picture of calibration ruler.

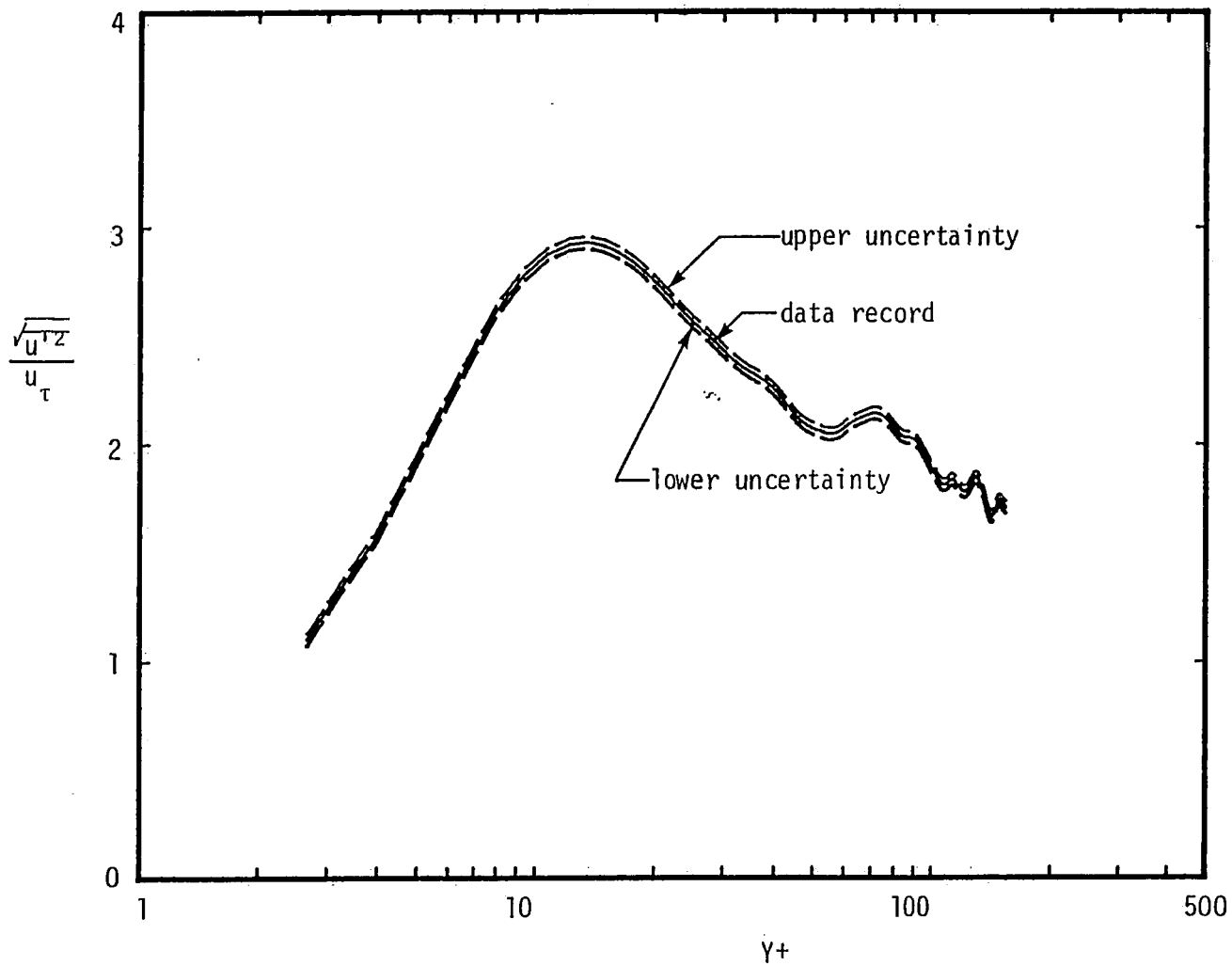

Figure B.2 Uncertainty of turbulence intensity for the first bubble line.

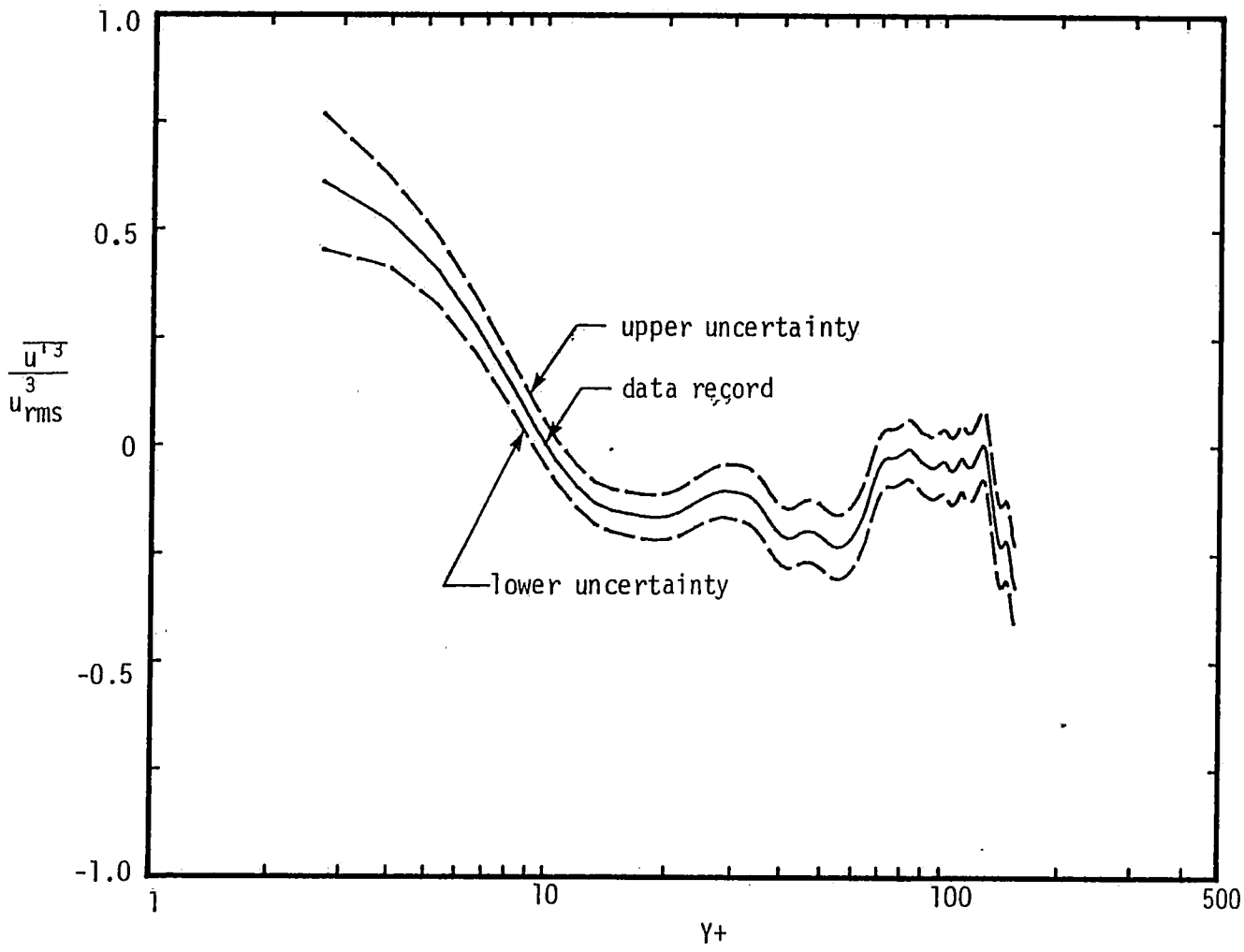

Figure B.3 Uncertainty of skewness for the first bubble line.

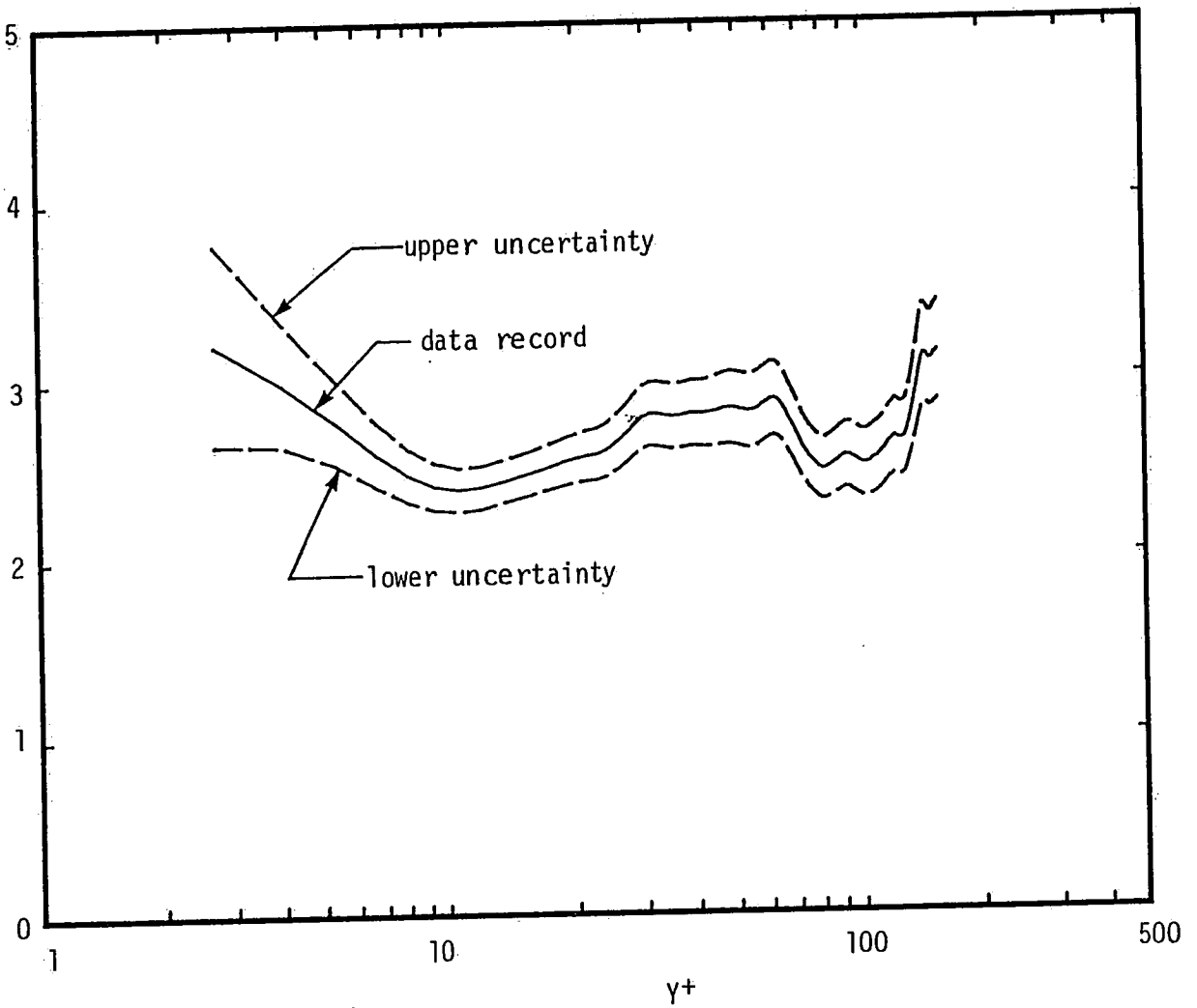

Figure B.4. Uncertainty of flatness for the first bubble line.

Appendix C. Data Sequence Presentation

C.1 Sequence of instantaneous u, u', du/dy, d^2u/dy^2, VITA, VITAxu', and du/dt profiles determined from image-processed hydrogen bubble flow visualization. Each profile is $t^+ = 2.3$ apart, and is offset respectively by $\Delta u^+ = 5.5$, $\Delta u'^+ = 5.5$, $\Delta du^+/dy^+ = 1.62$, $\Delta du^{+2}/dy^{+2} = 0.18$, $k = 1$, $k * u'^+ = 1.8$, $\Delta du^+/dt^+ = 1.62$.

C.2 Instantaneous streamwise velocity behavior and corresponding VITA result, presented at selected haights above the boundary surface.

C.3. Contours of $k = Var(t,T)/u'^2$.

----, $k = 0.5$; ——— , $k = 0.75$; dotted area, $k = 1.0$; darkened area, $k = 1.25$.

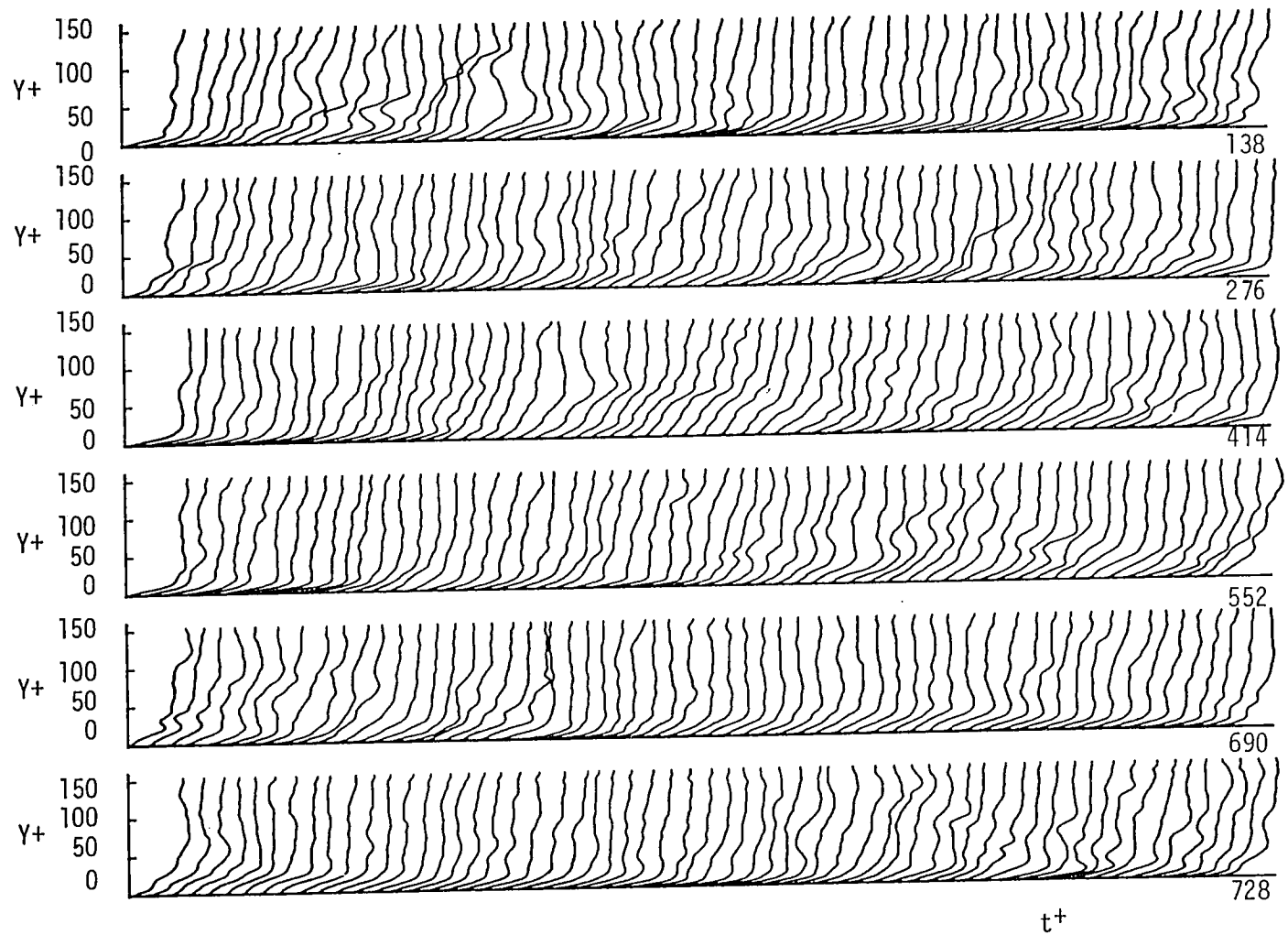

Figure C.1.1.(a) Instantaneous velocity profiles for the first bubble-line data sequence; $\Delta u^+=5.5$, $\Delta t^+=2.3$.

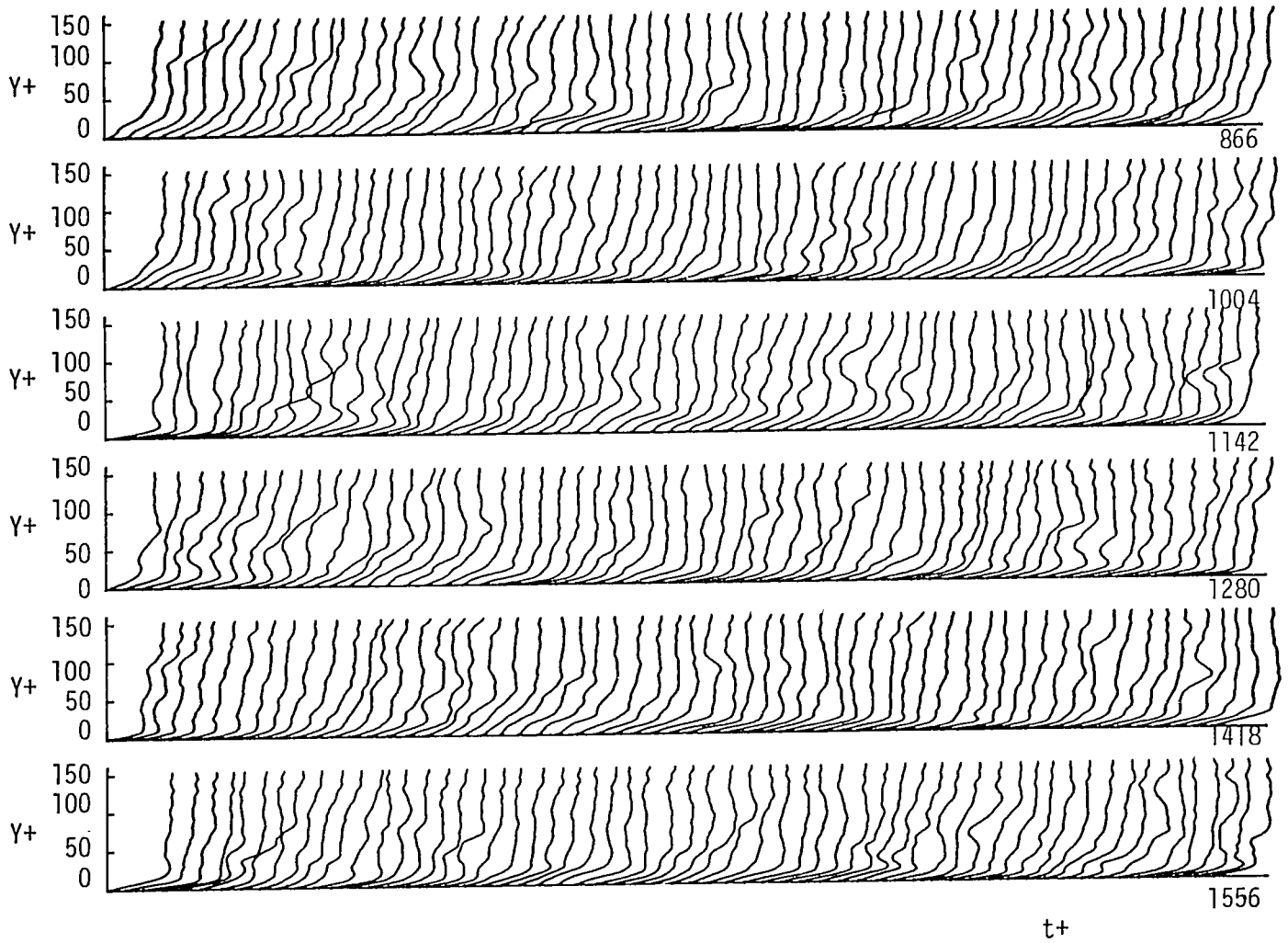

Figure C.1.1.(b) Continued.

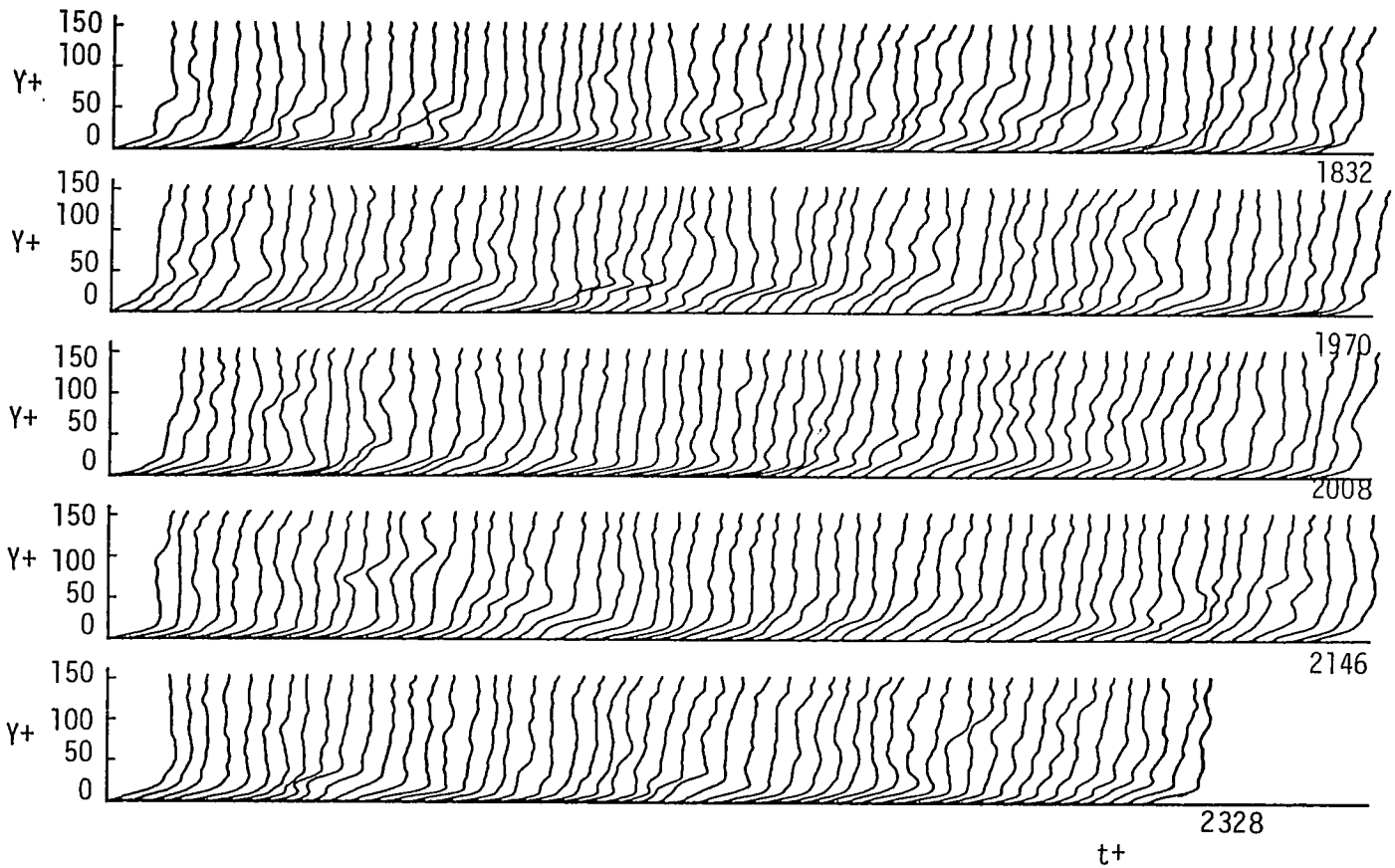

Figure C.1.1.(c) Continued.

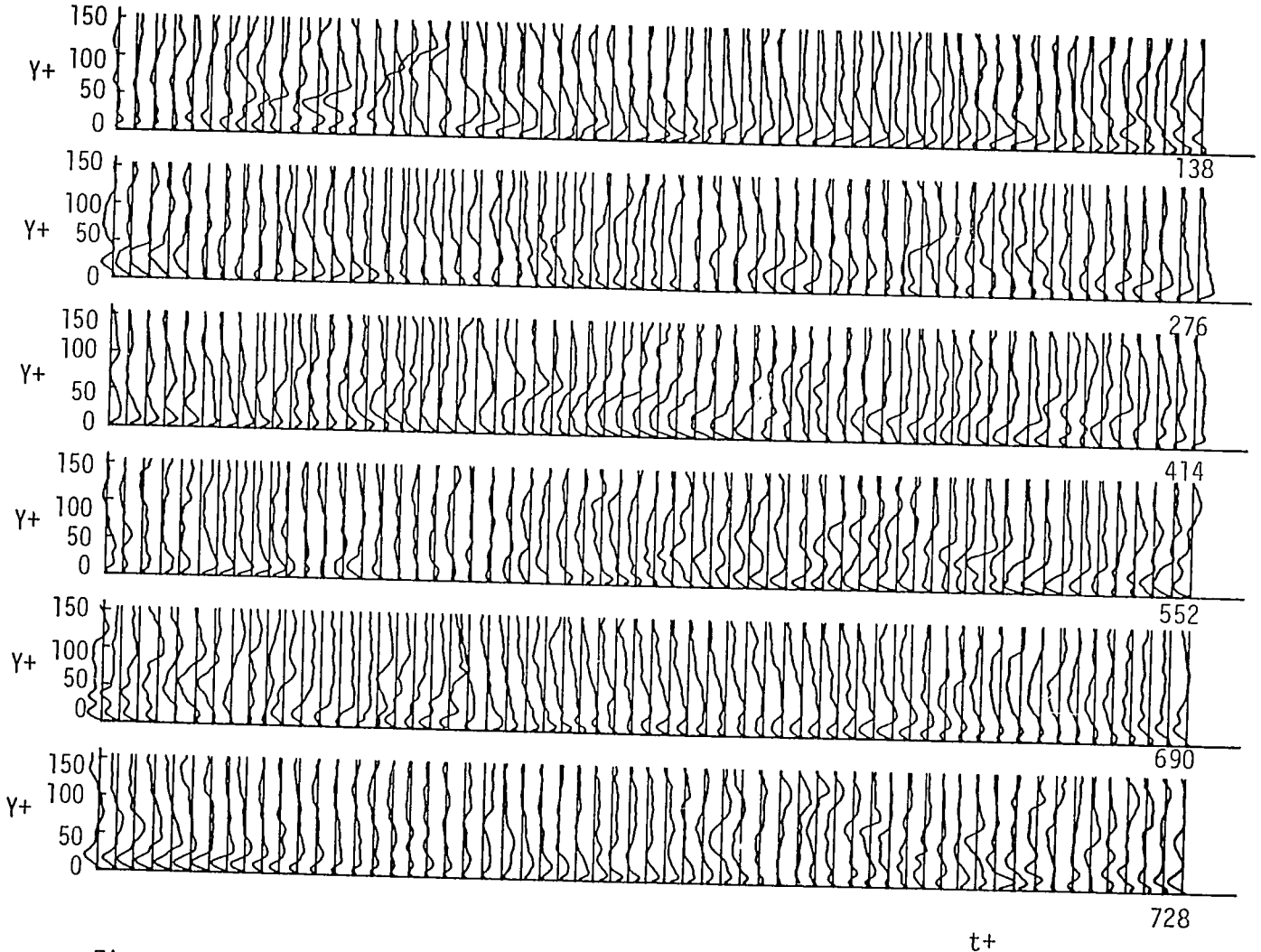

Figure C.1.2.(a) Instantaneous velocity fluctuation profiles for the first bubble-line data sequence;$\Delta u'^+=5.5$, $\Delta t^+=2.3$.

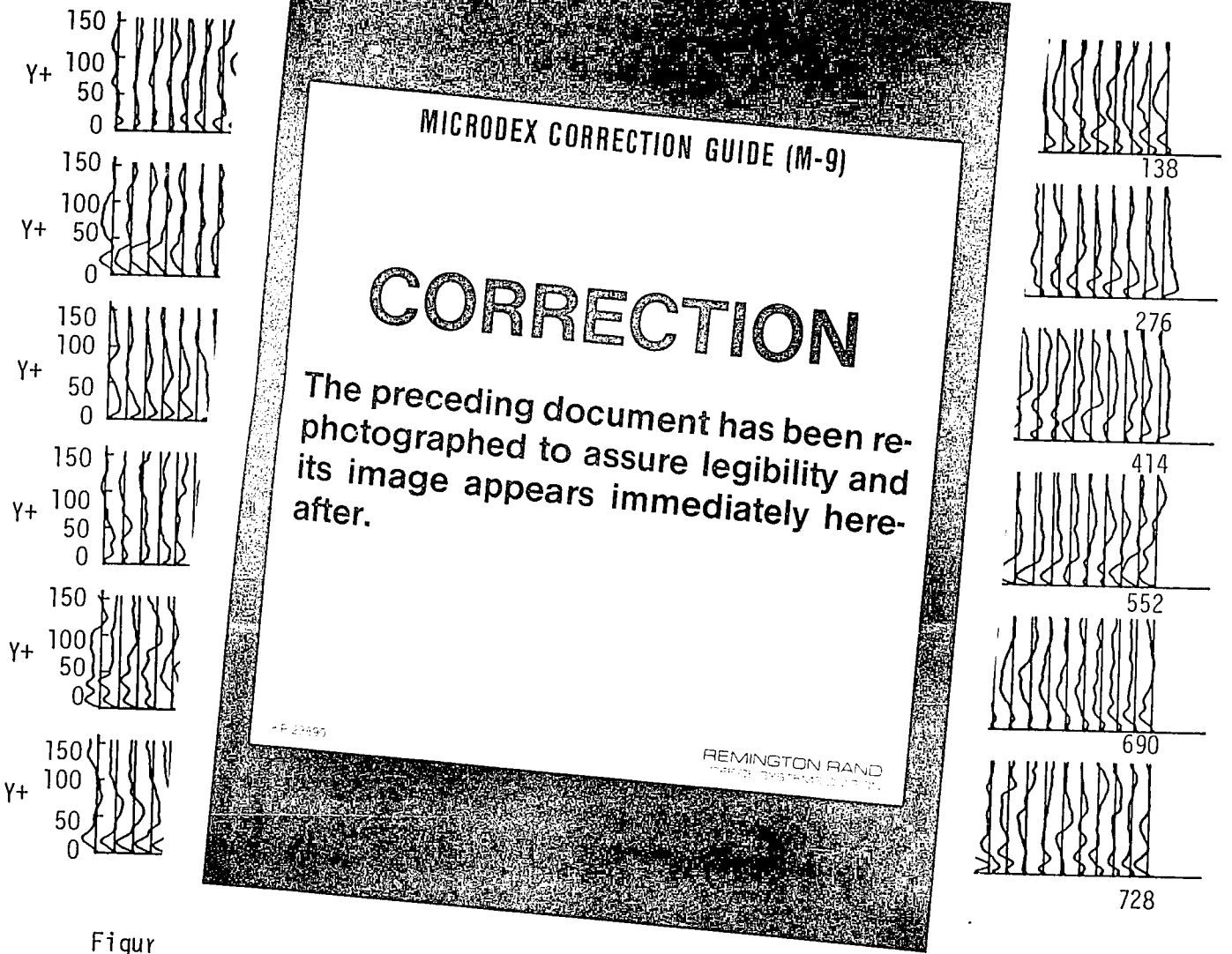

Figur

he first

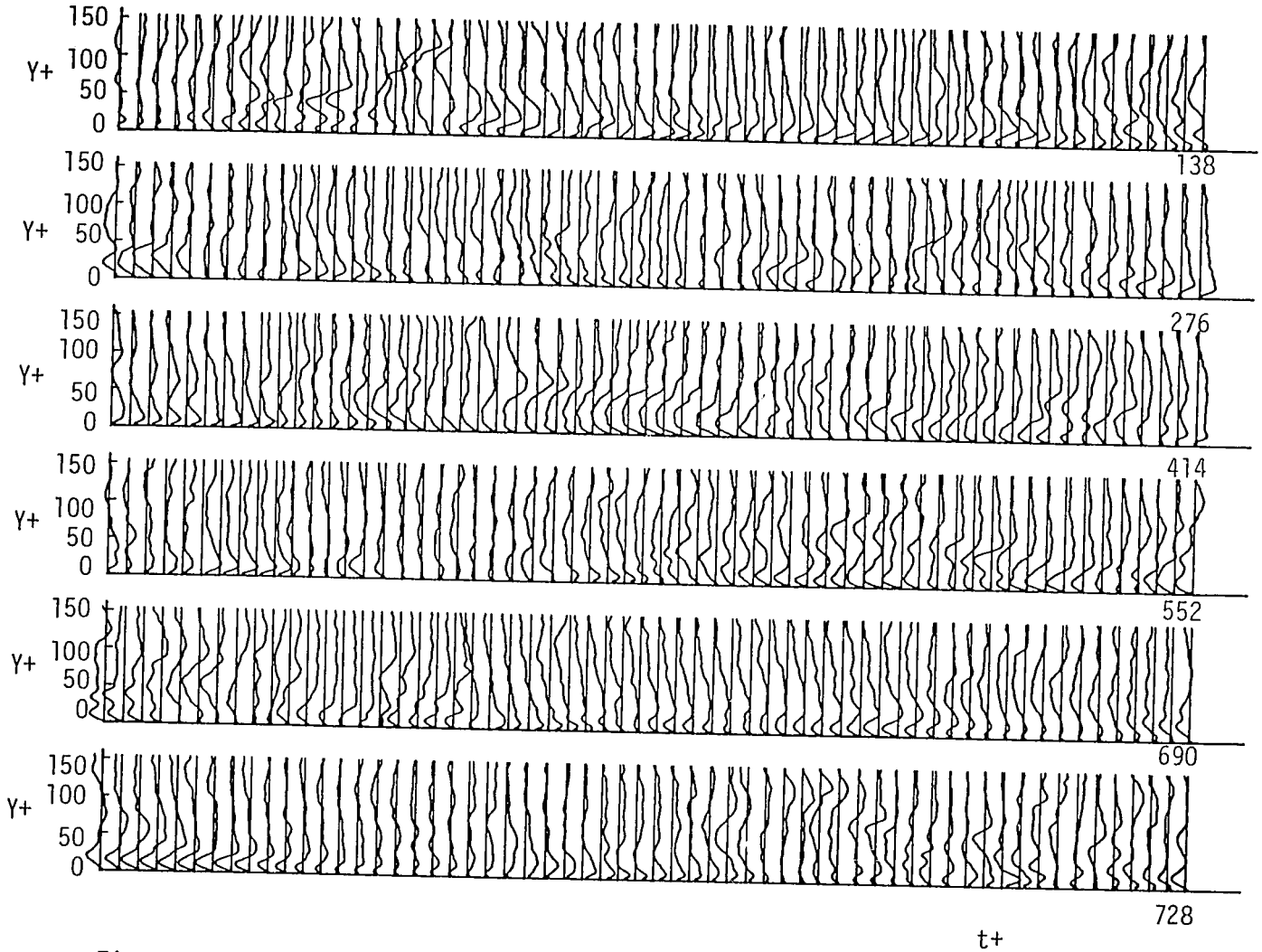

Figure C.1.2.(a) Instantaneous velocity fluctuation profiles for the first bubble-line data sequence;$\Delta u'^+=5.5$, $\Delta t^+=2.3$.

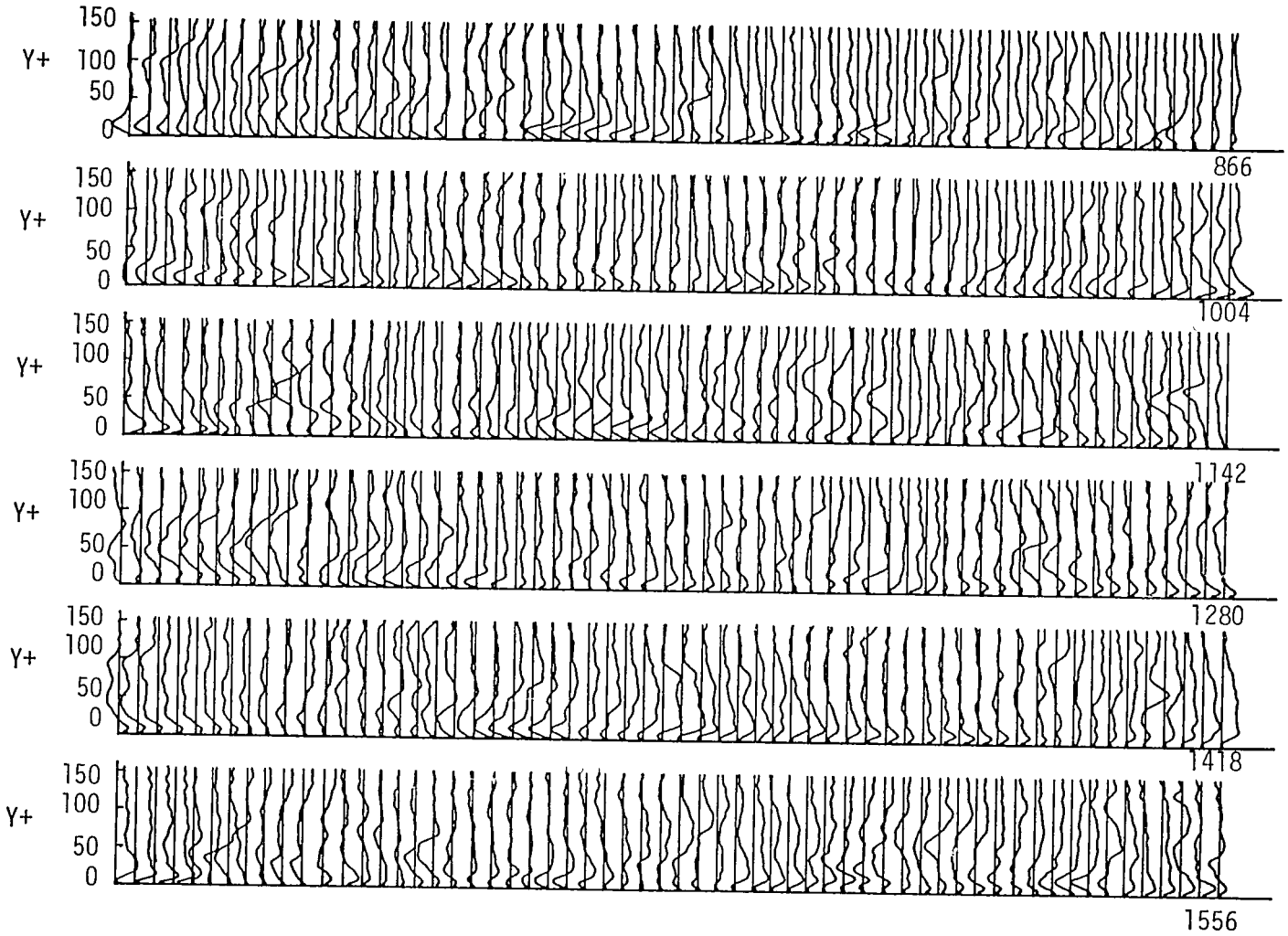

Figure C.1.2.(b) Continued.

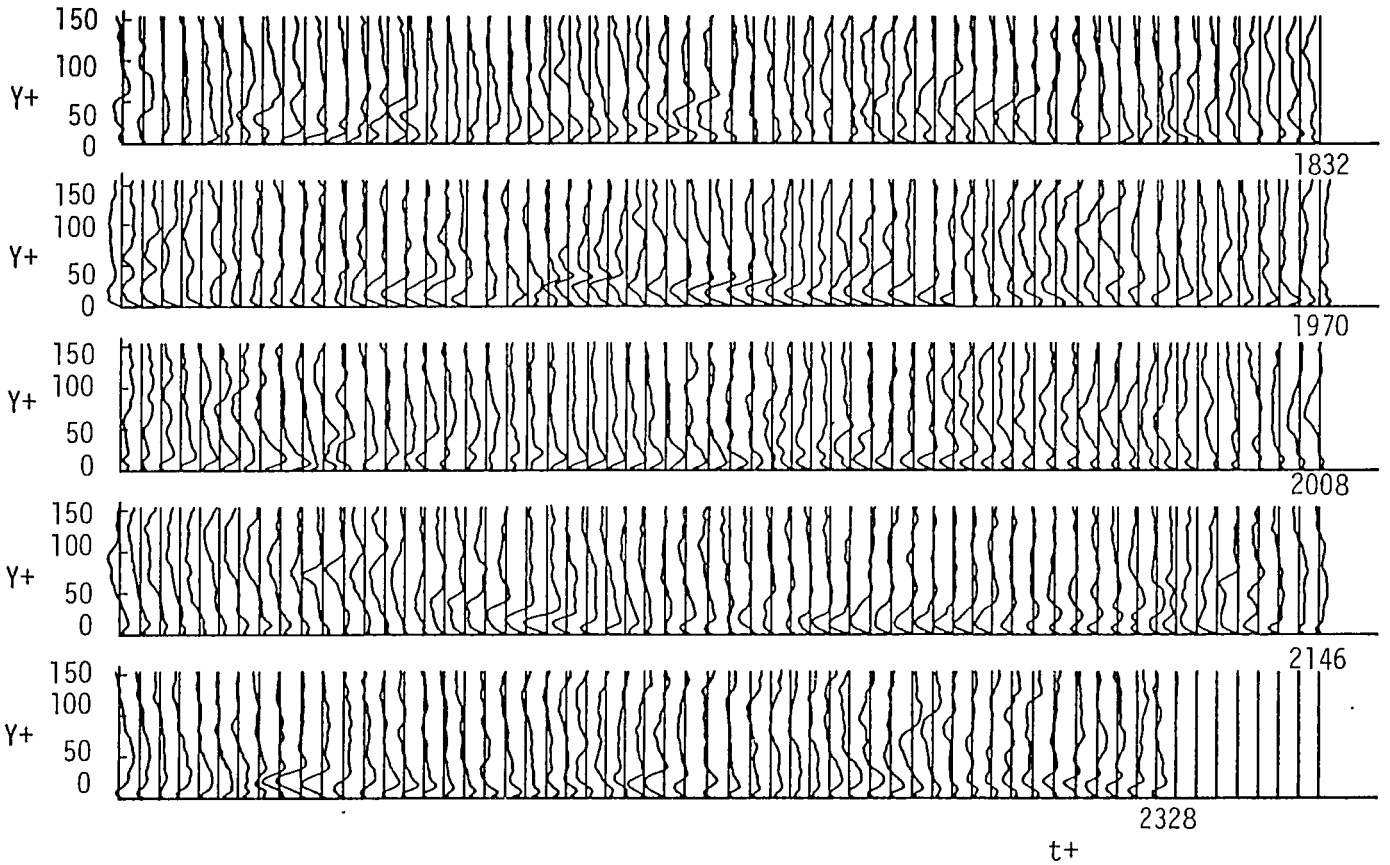

Figure C.1.2.(c). Continued.

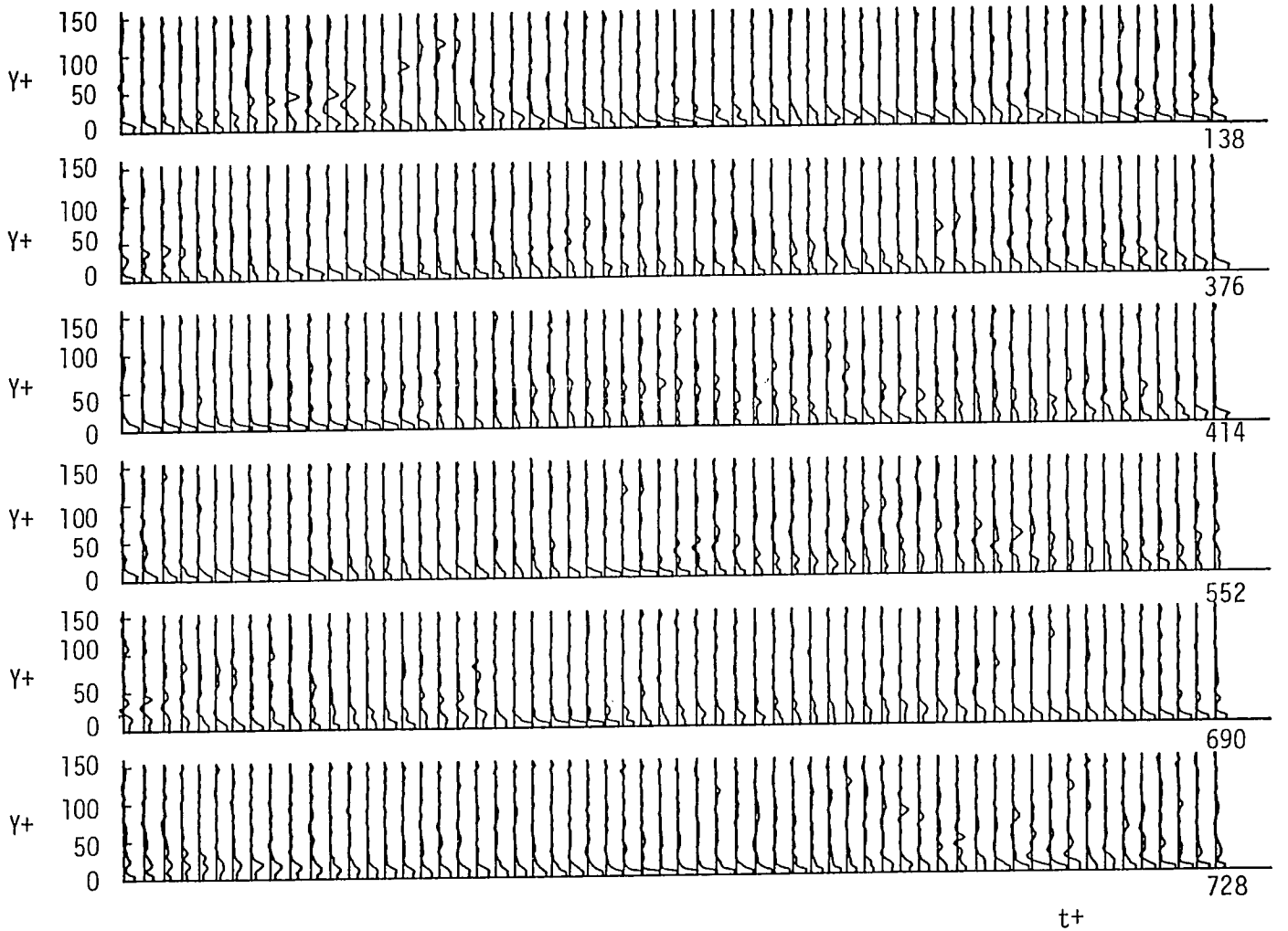

Figure C.1.3.(a). Instantaneous du+/dy+ profiles for the first bubble-line data sequence; $\Delta|du+/dy+| = 1.62$, $\Delta t+=2.3$.

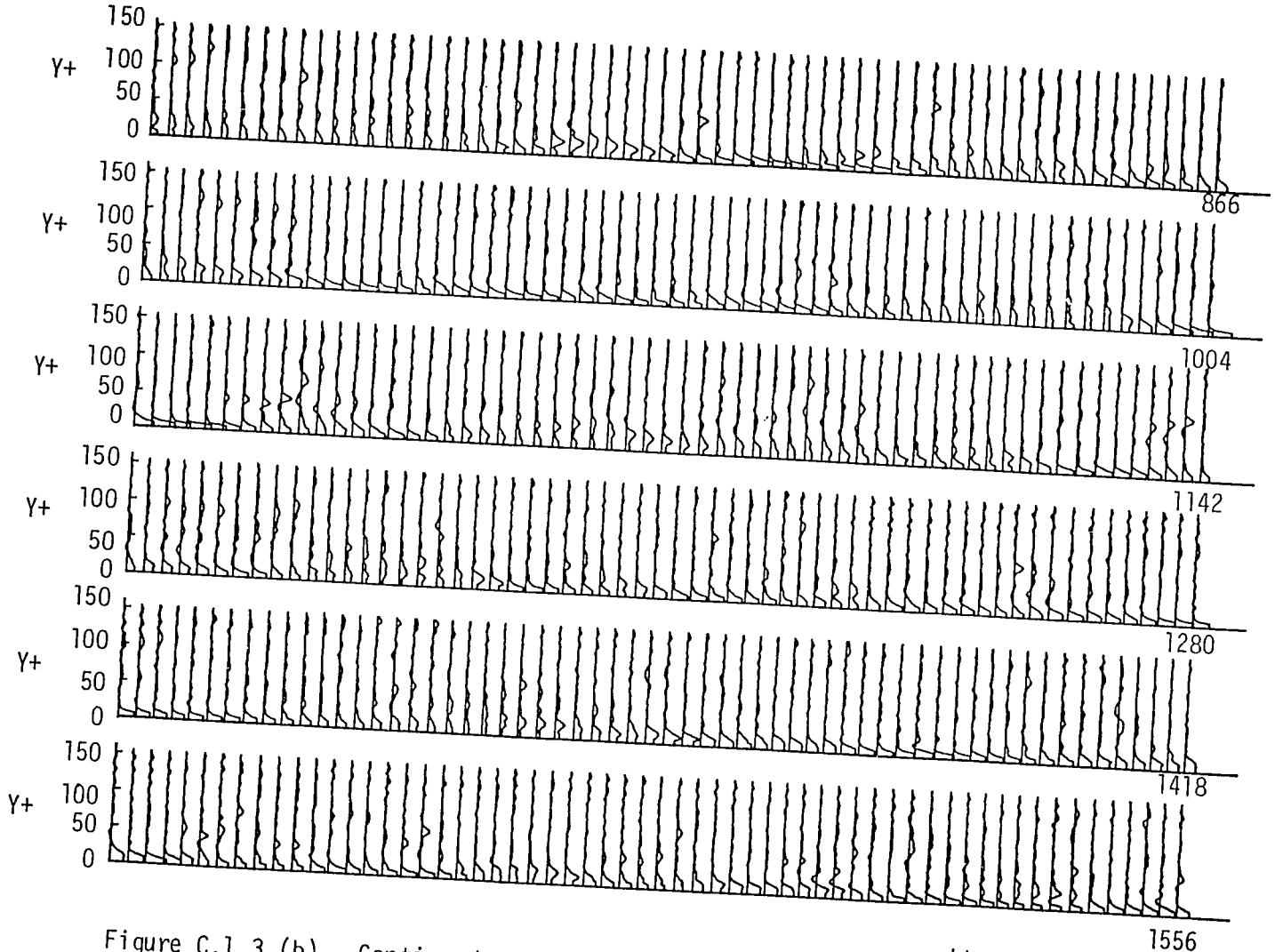

Figure C.1.3.(b). Continued.

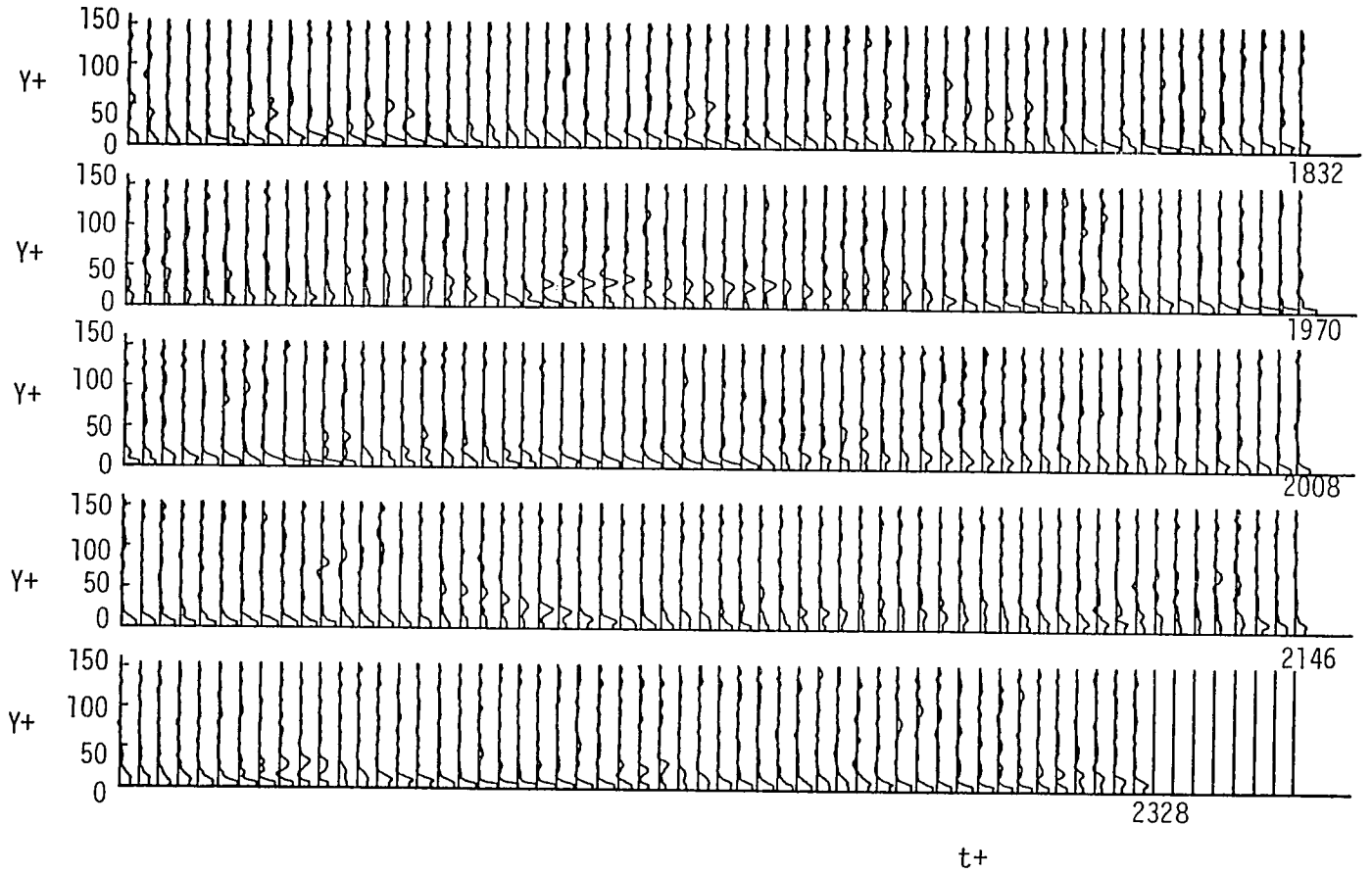

Figure C.1.3.(c). Continued.

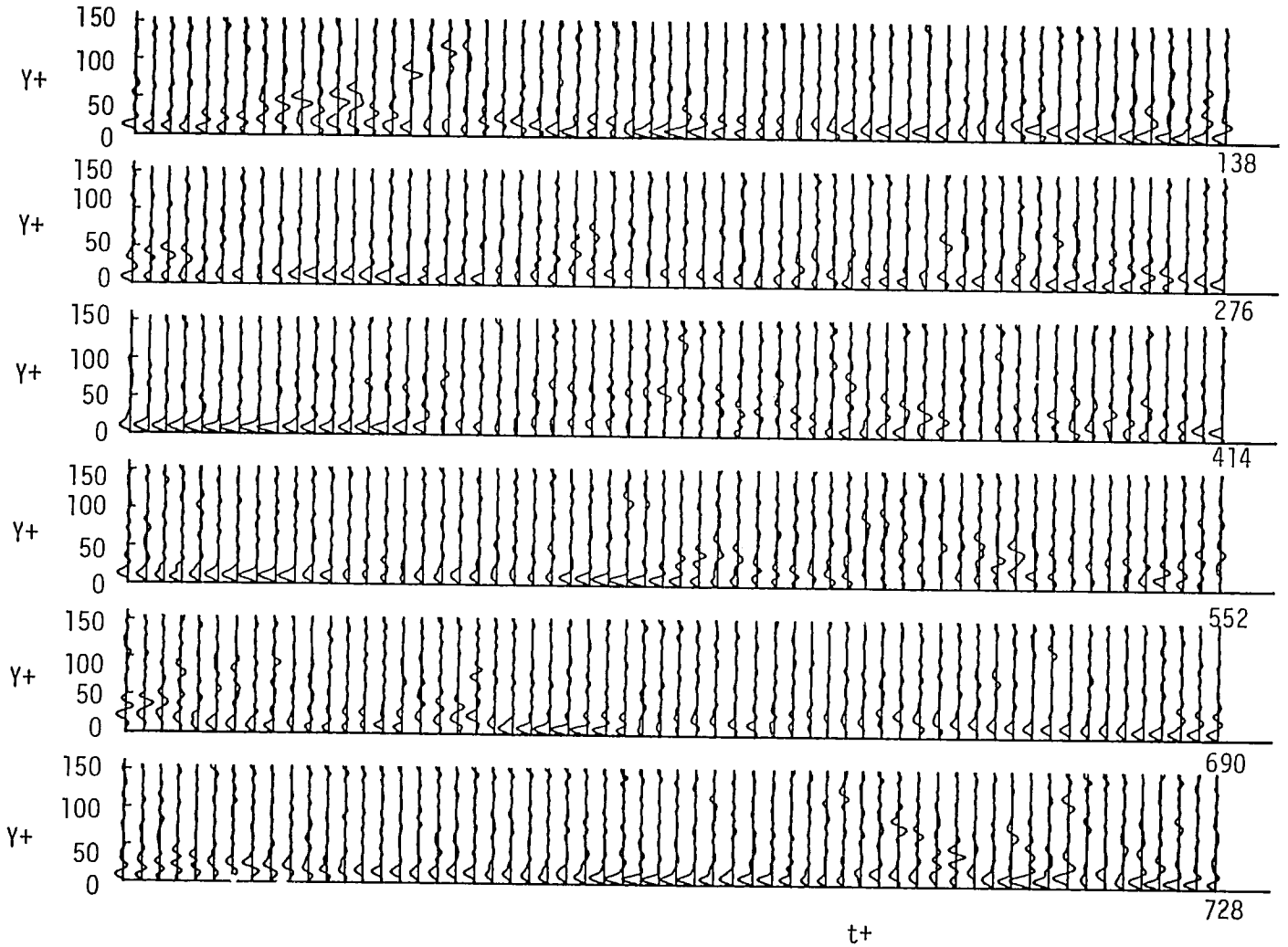

Figure C.1.4.(a). Instantaneous d^2u/dy^2 profiles for the first bubble-line data sequence; $\Delta|d^2u+/dy+^2| = 0.18$, $\Delta t+=2.3$.

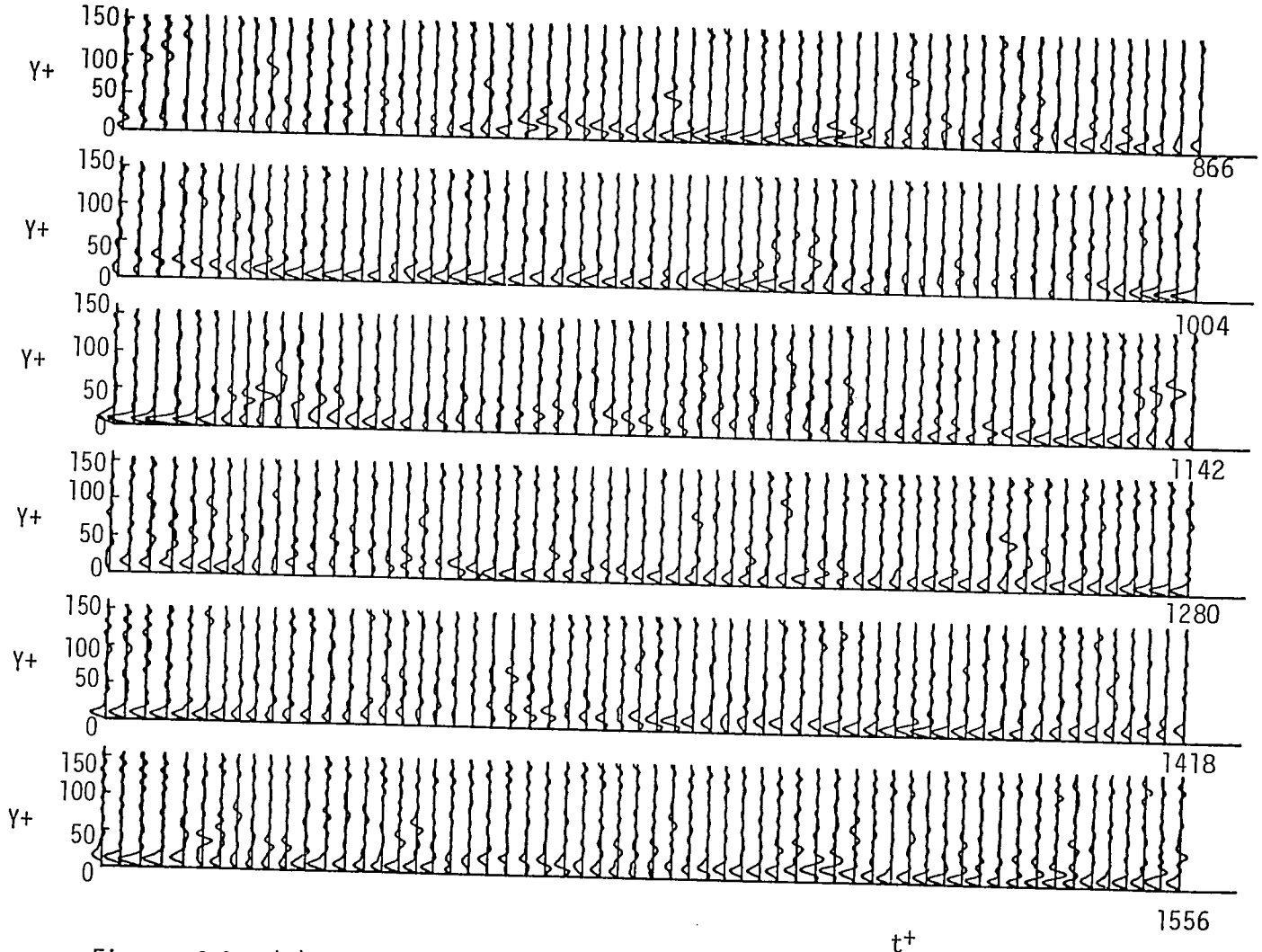

Figure C.1.4.(b) Continued.

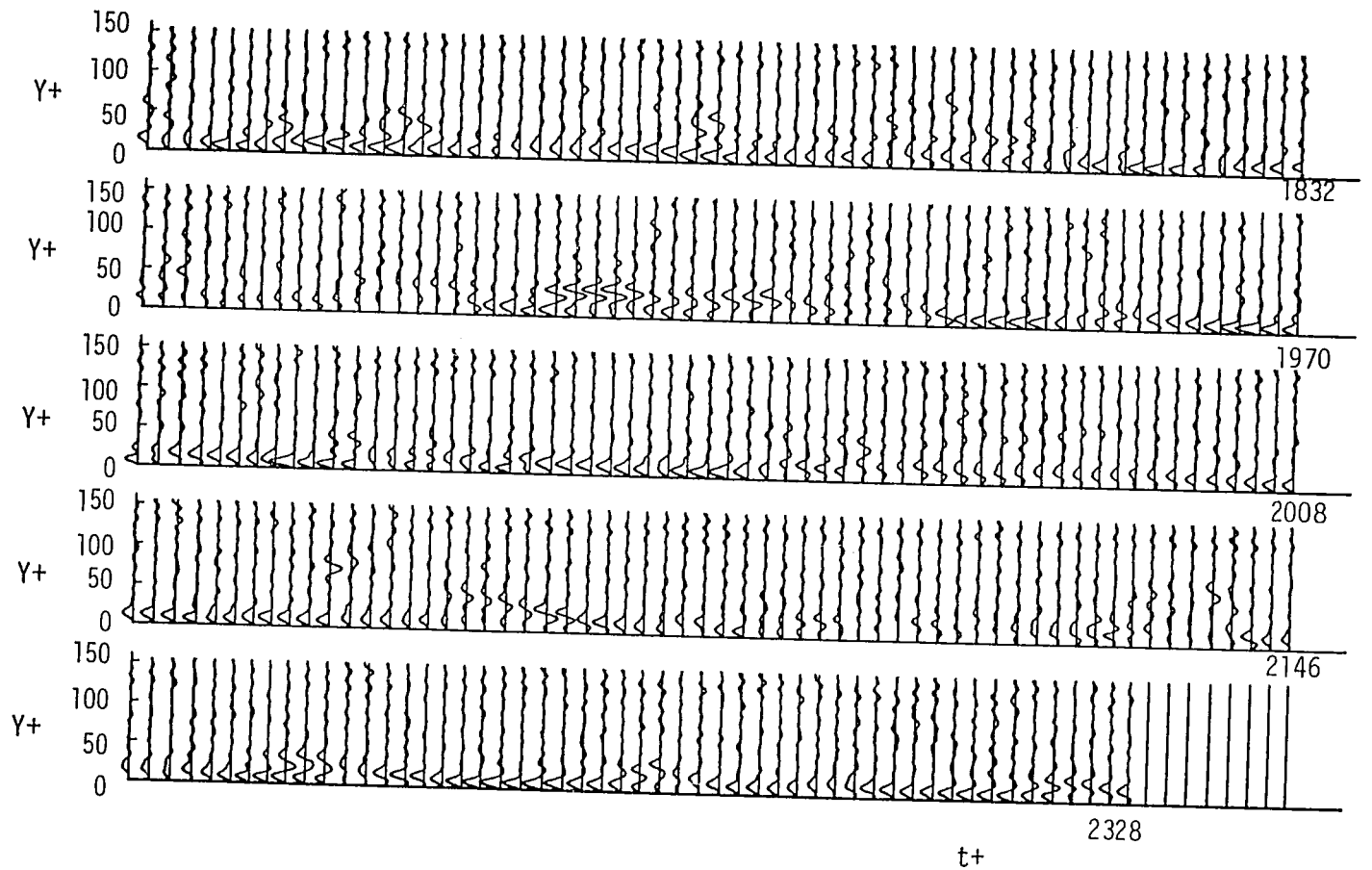

Figure C.1.4.(c). Continued.

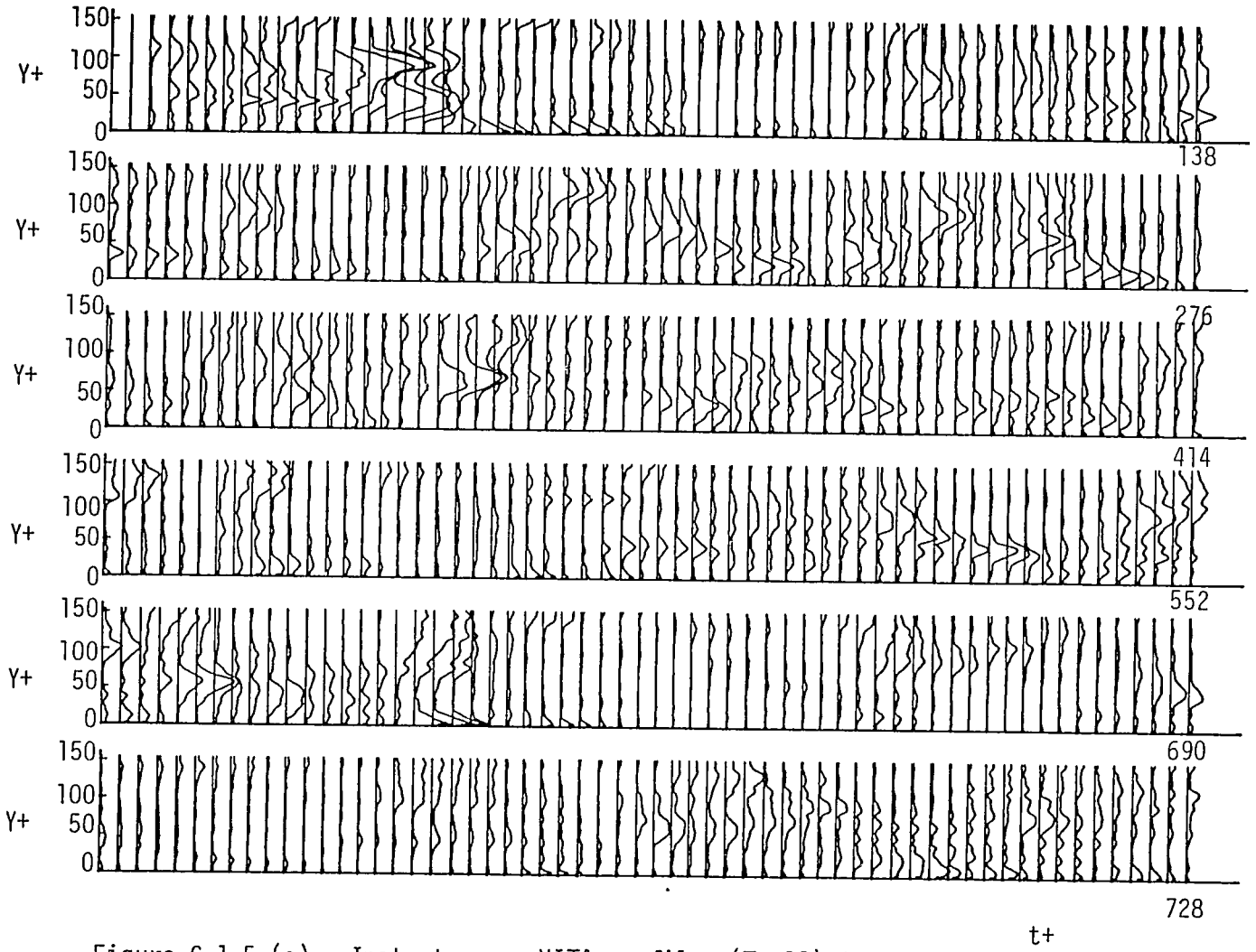

Figure C.1.5.(a). Instantaneous VITA profiles (T+=11) for the first bubble-line data sequence; $\Delta K=Var(t,T)/u^2_{rms}=1$, $\Delta t+=2.3$.

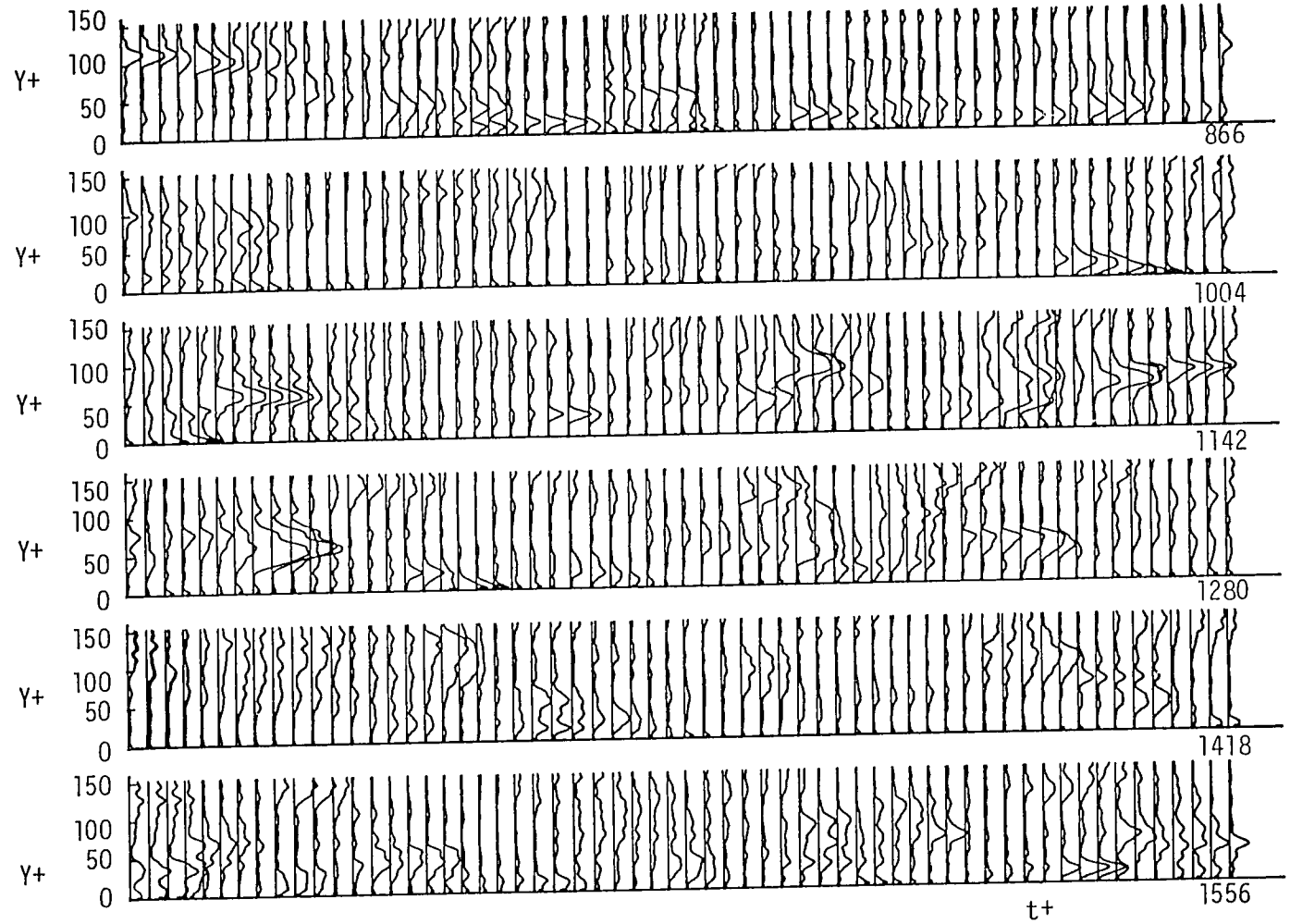

Figure C.1.5.(b). Continued.

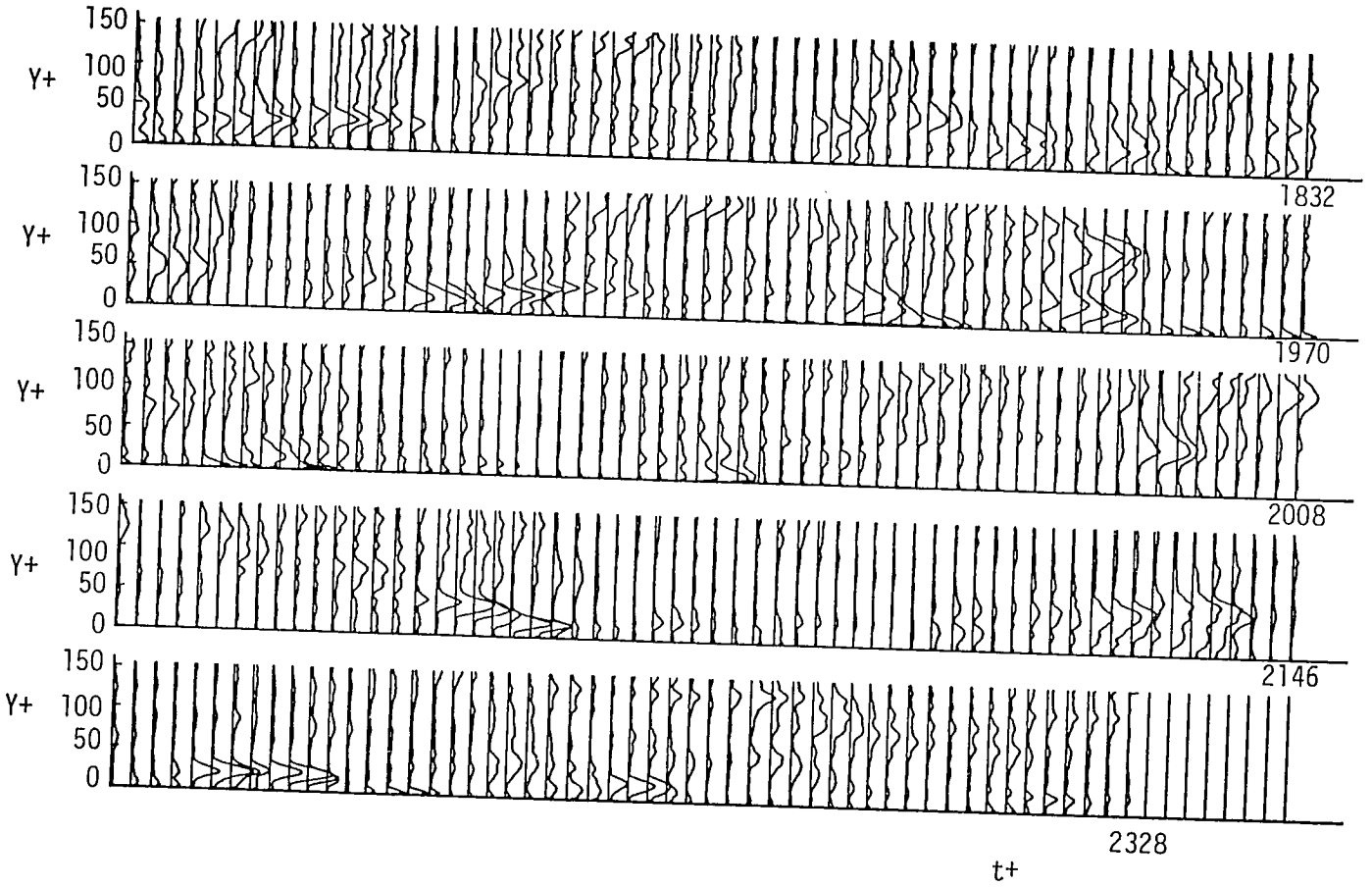

Figure C.1.5.(c). Continued.

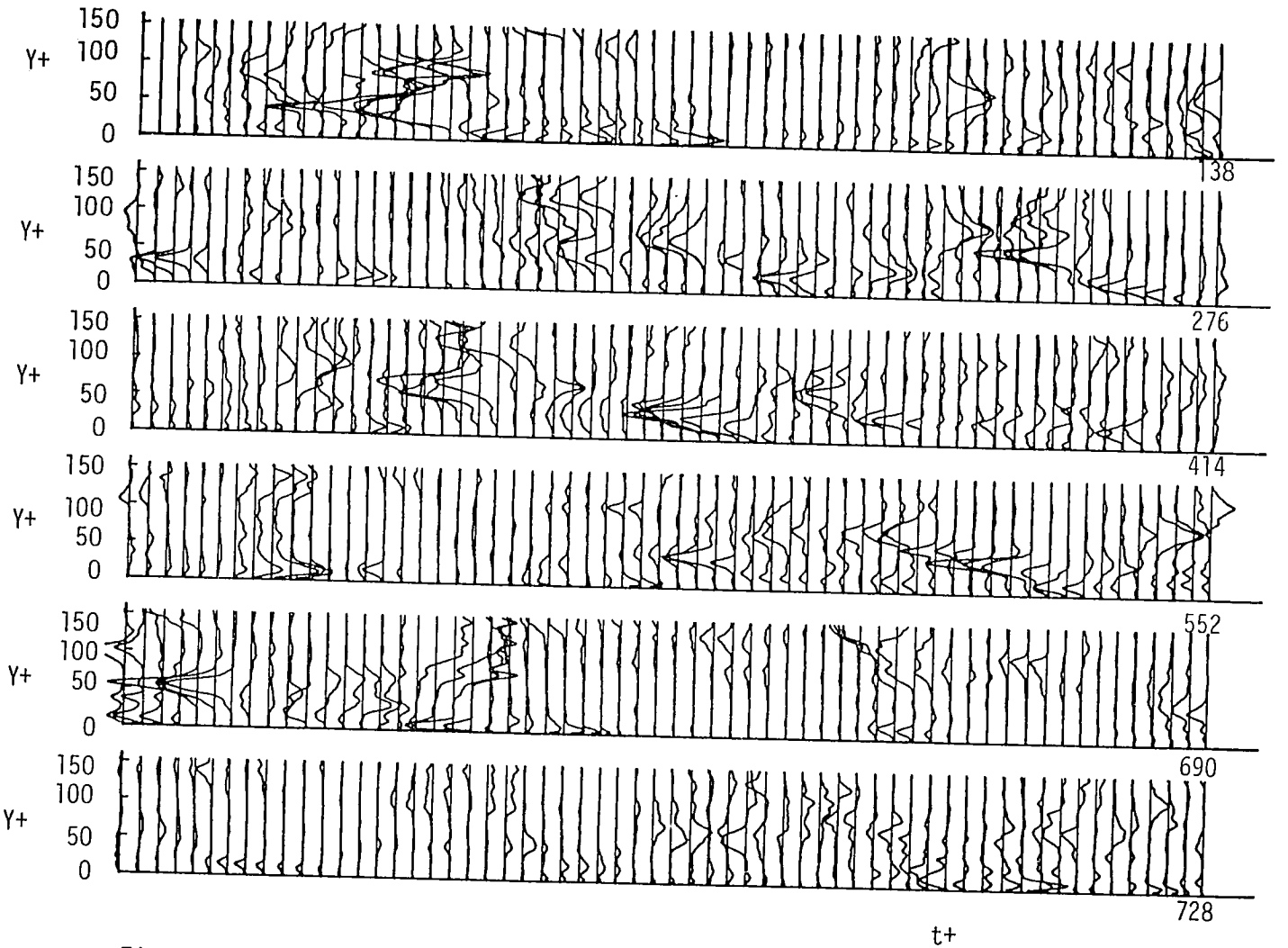

Figure C.1.6.(a). Instantaneous VITAxu' profiles for the first bubble-line data sequence; $\Delta|VITAxu'+|=1.8$, $\Delta t+=2.3$.

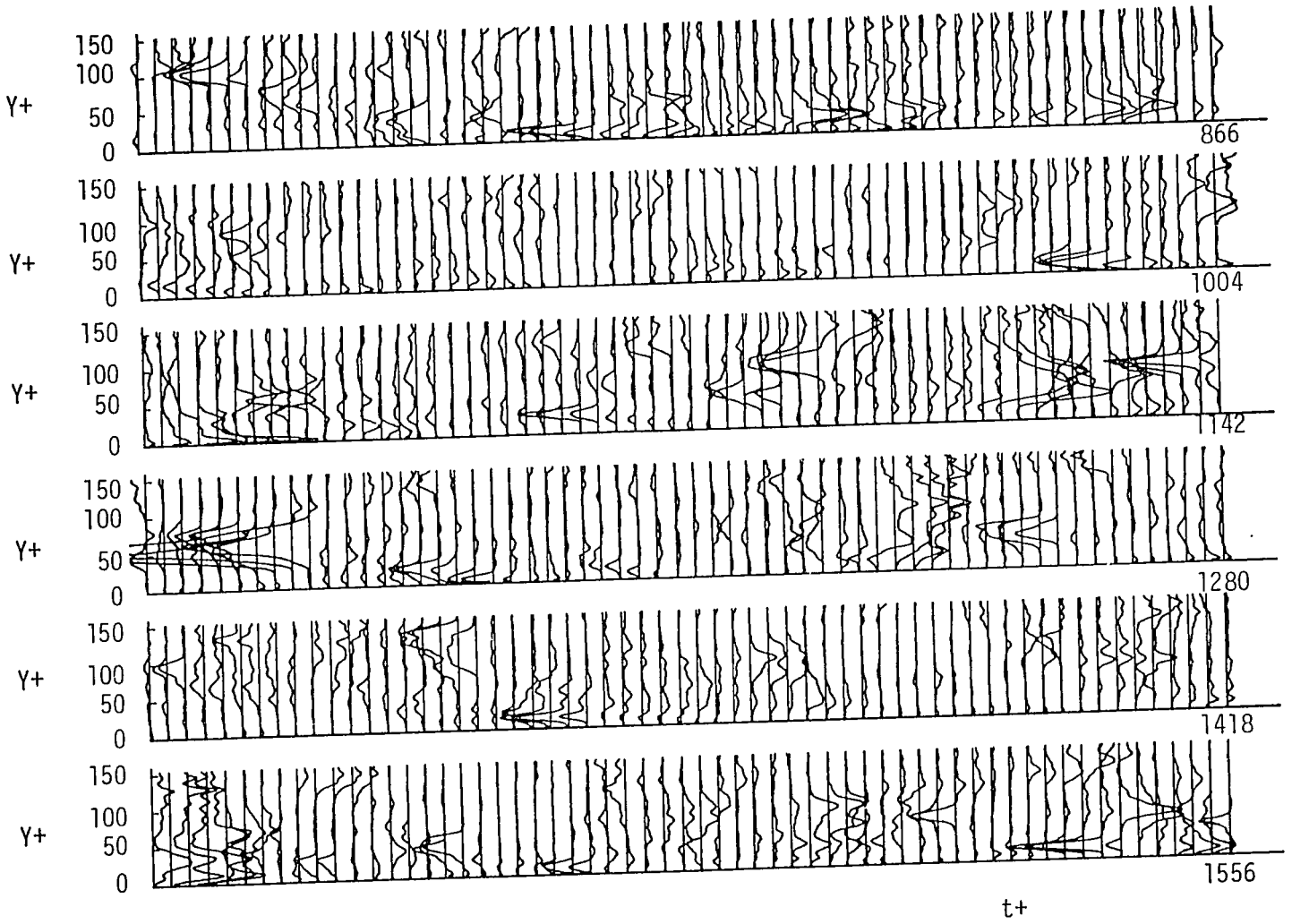

Figure C.1.6.(b). Continued.

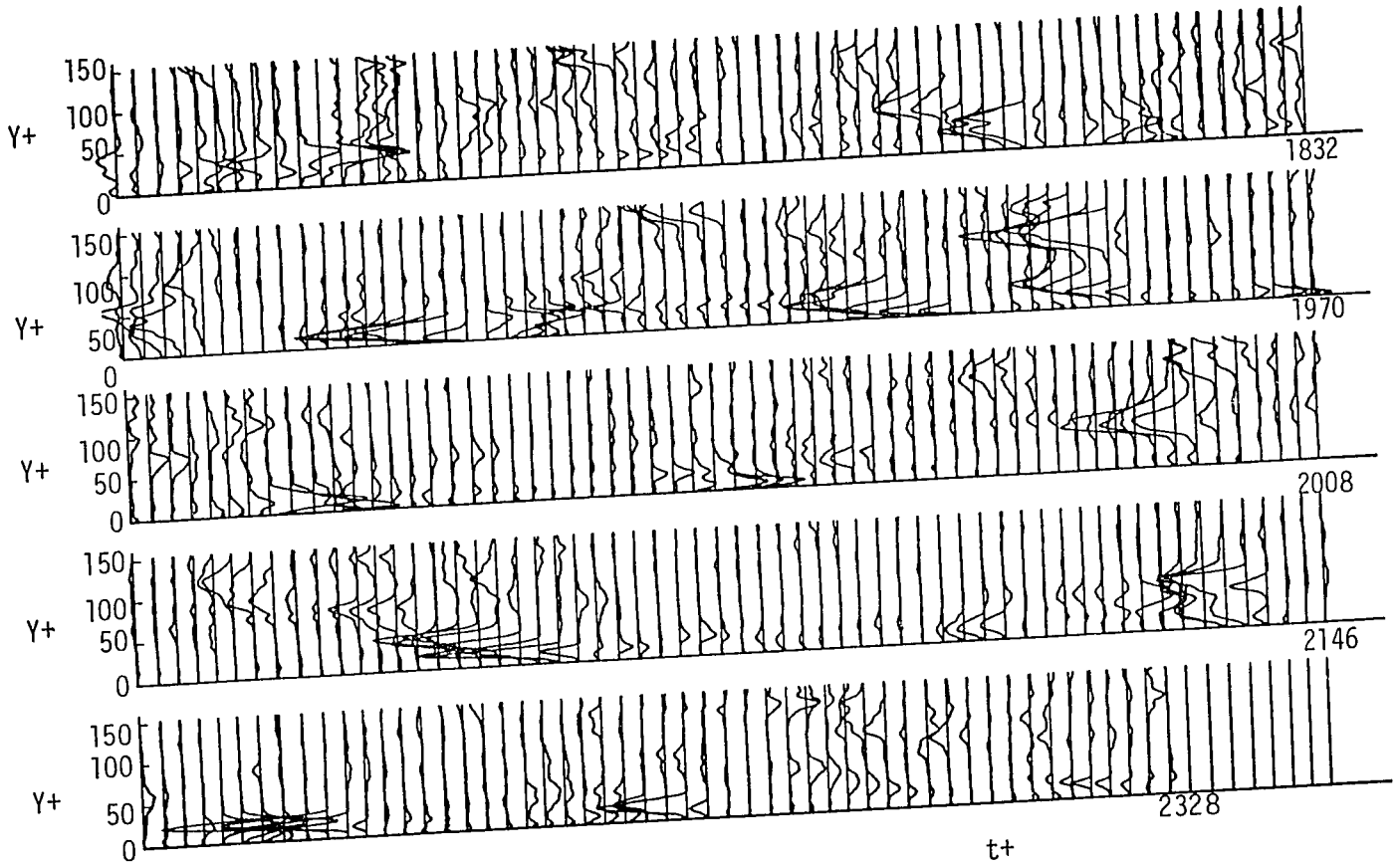

Figure C.1.6.(c) Continued.

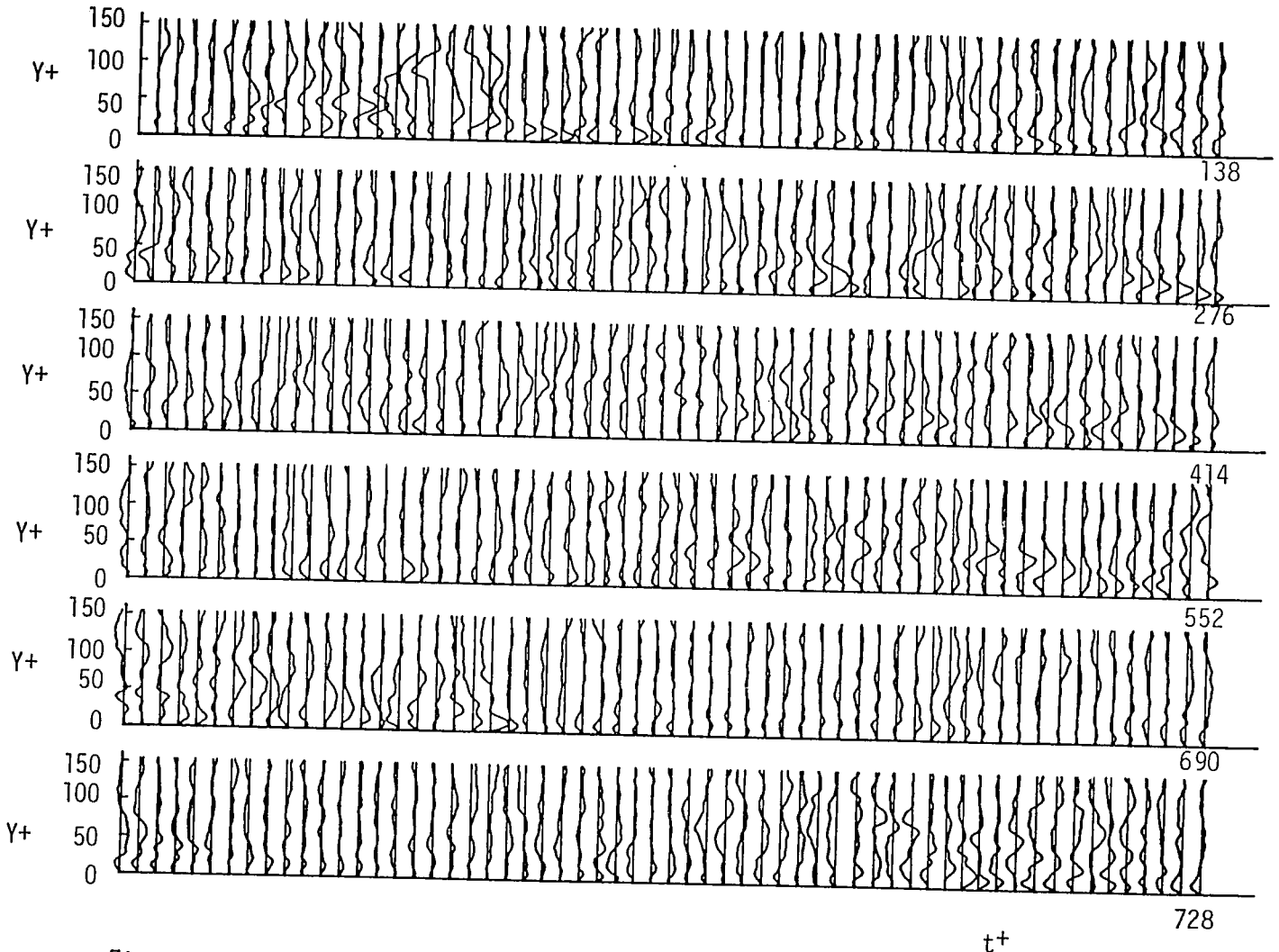

Figure C.1.7(a). Instantaneous du^+/dt^+ profiles for the first bubble-line data sequence; $\Delta|du^+/dt^+|=1.62$, $\Delta t^+=2.3$.

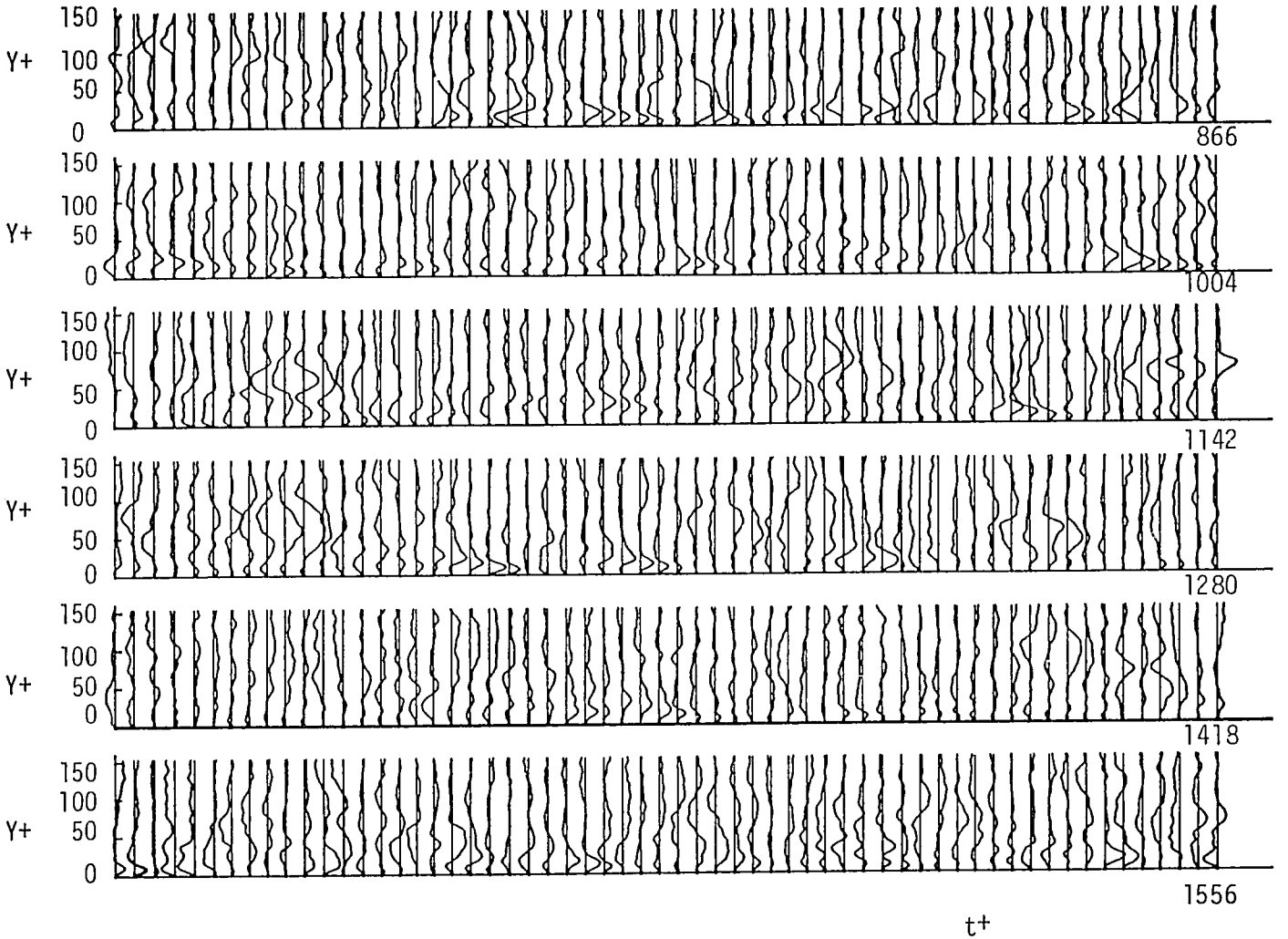

Figure C.1.7.(b). Continued.

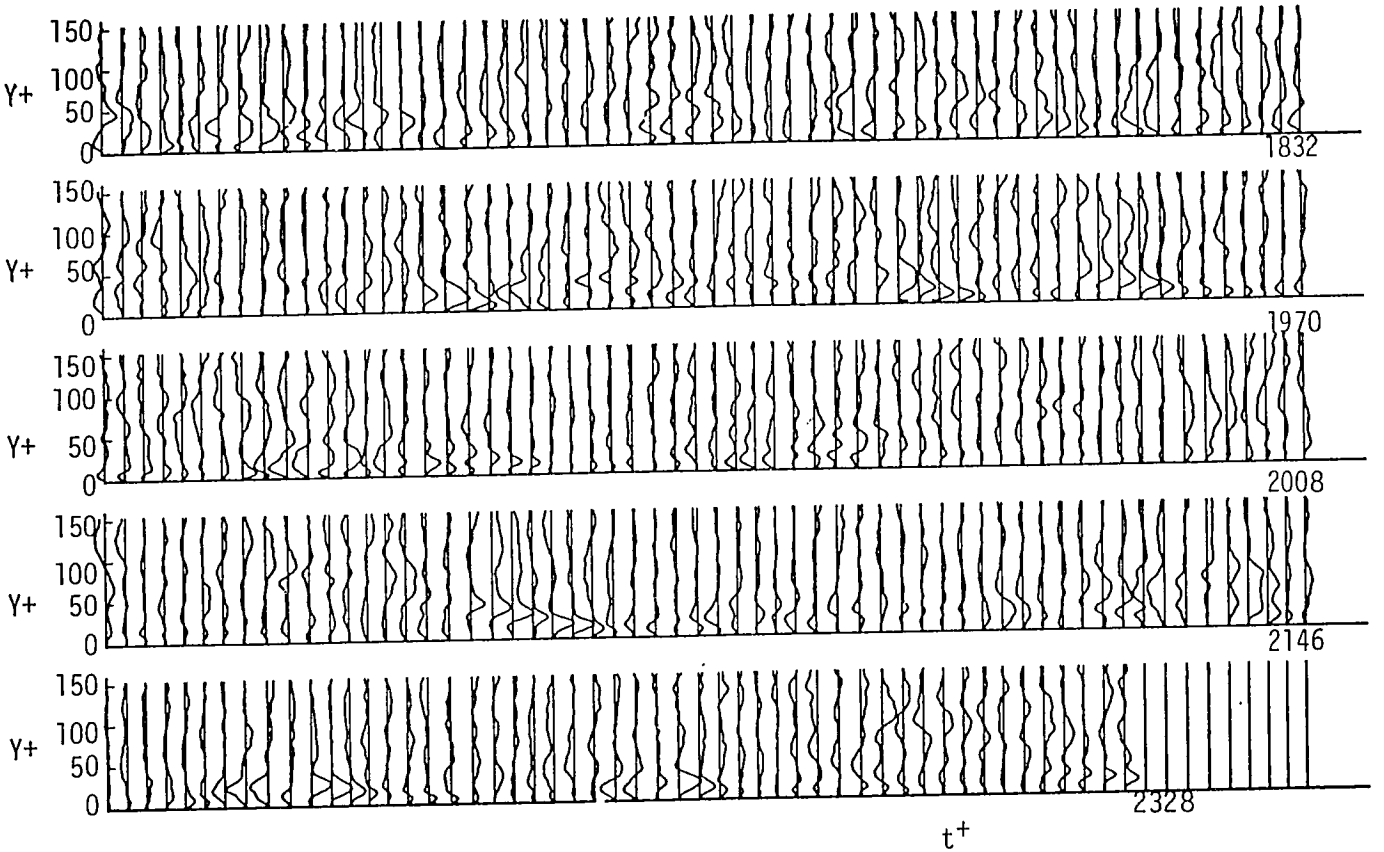

Figure C.1.7(c). Continued.

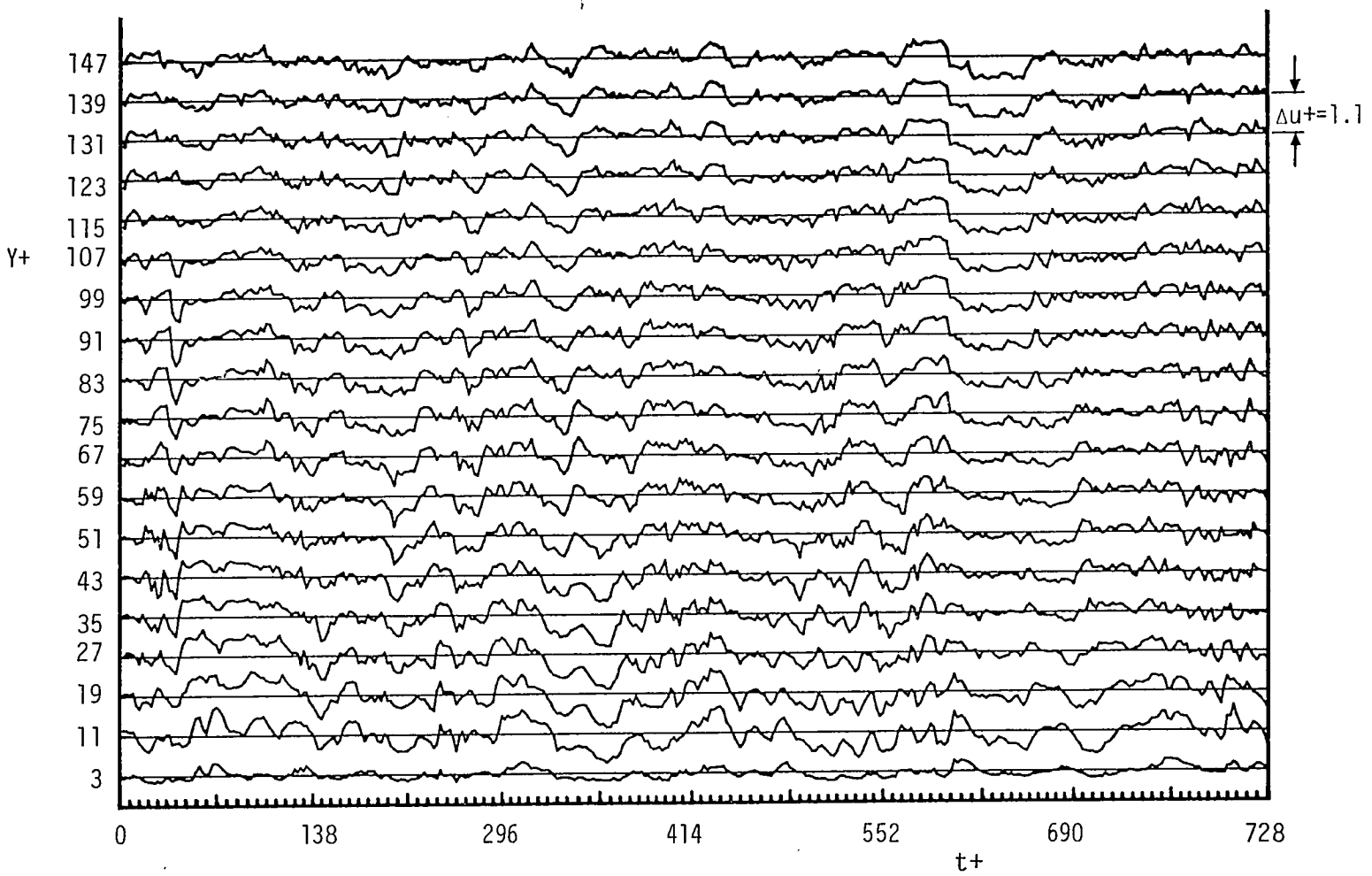

Figure C.2.1.(a). Instantaneous streamwise velocity behavior for the first bubble-line data record.

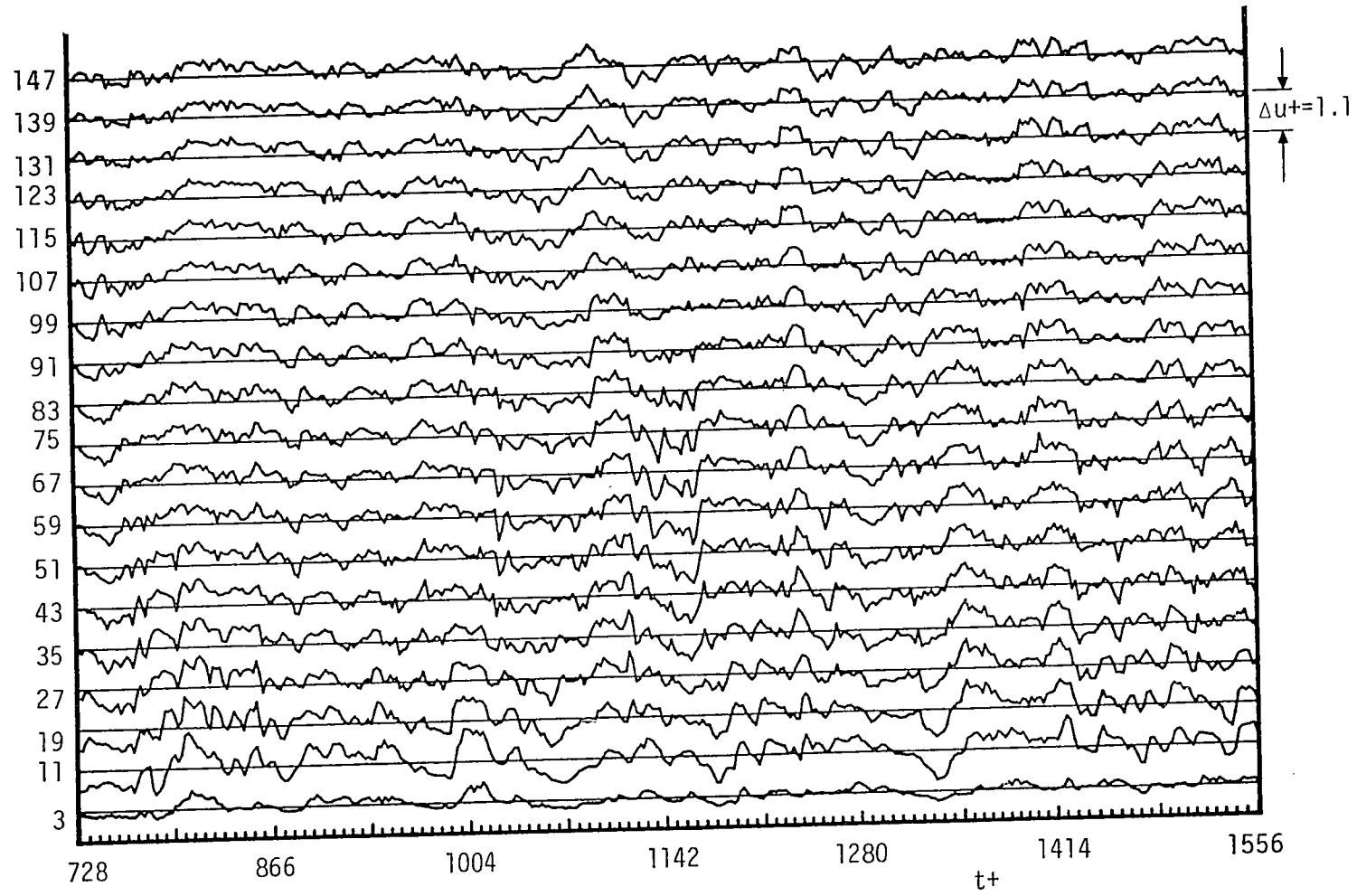

Figure C.2.1.(b). Continued.

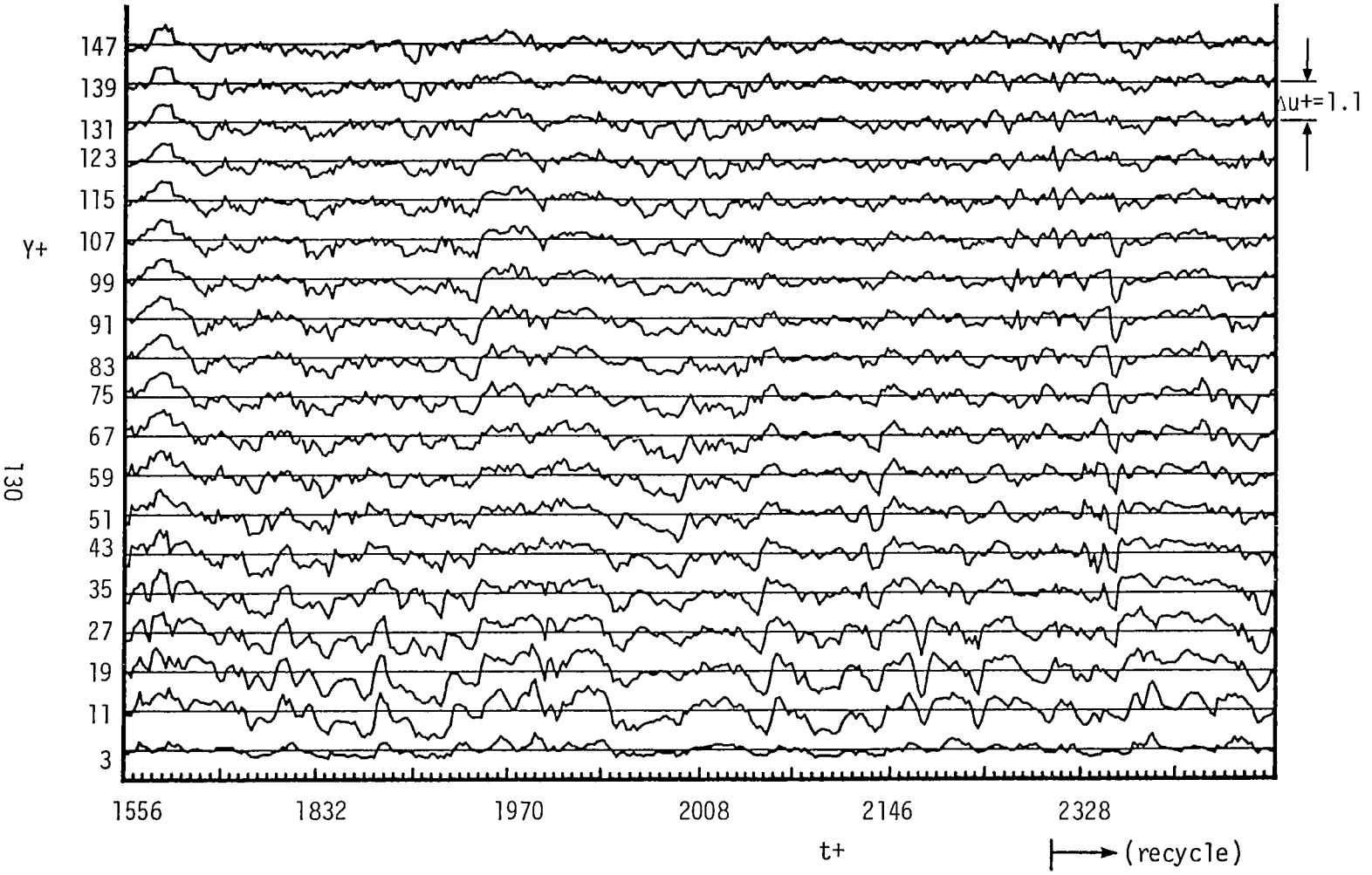

Figure C.2.1.(c) Continued.

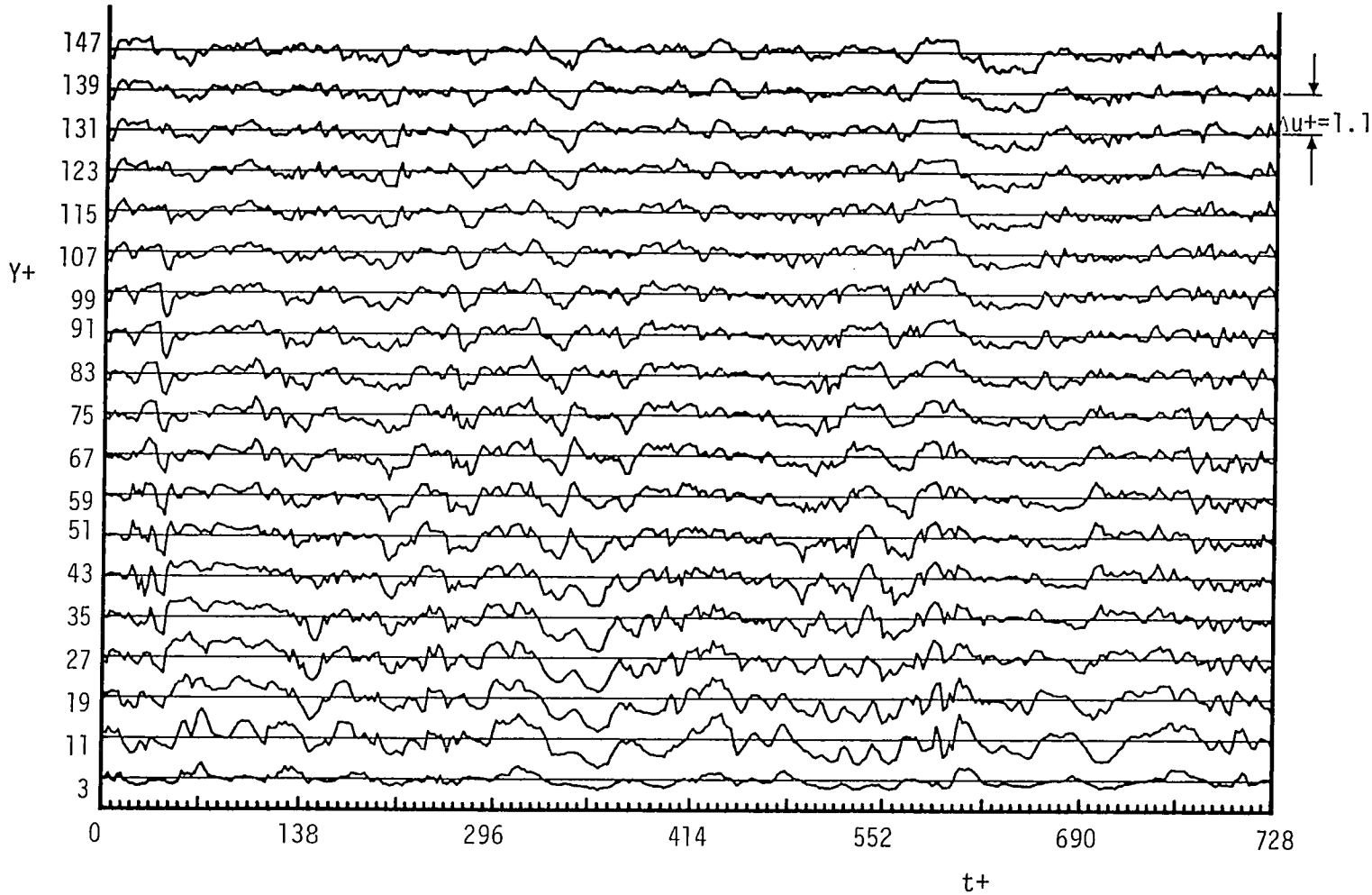

Figure C.2.2.(a) Instantaneous streamwise velocity behavior for the second bubble-line data record.

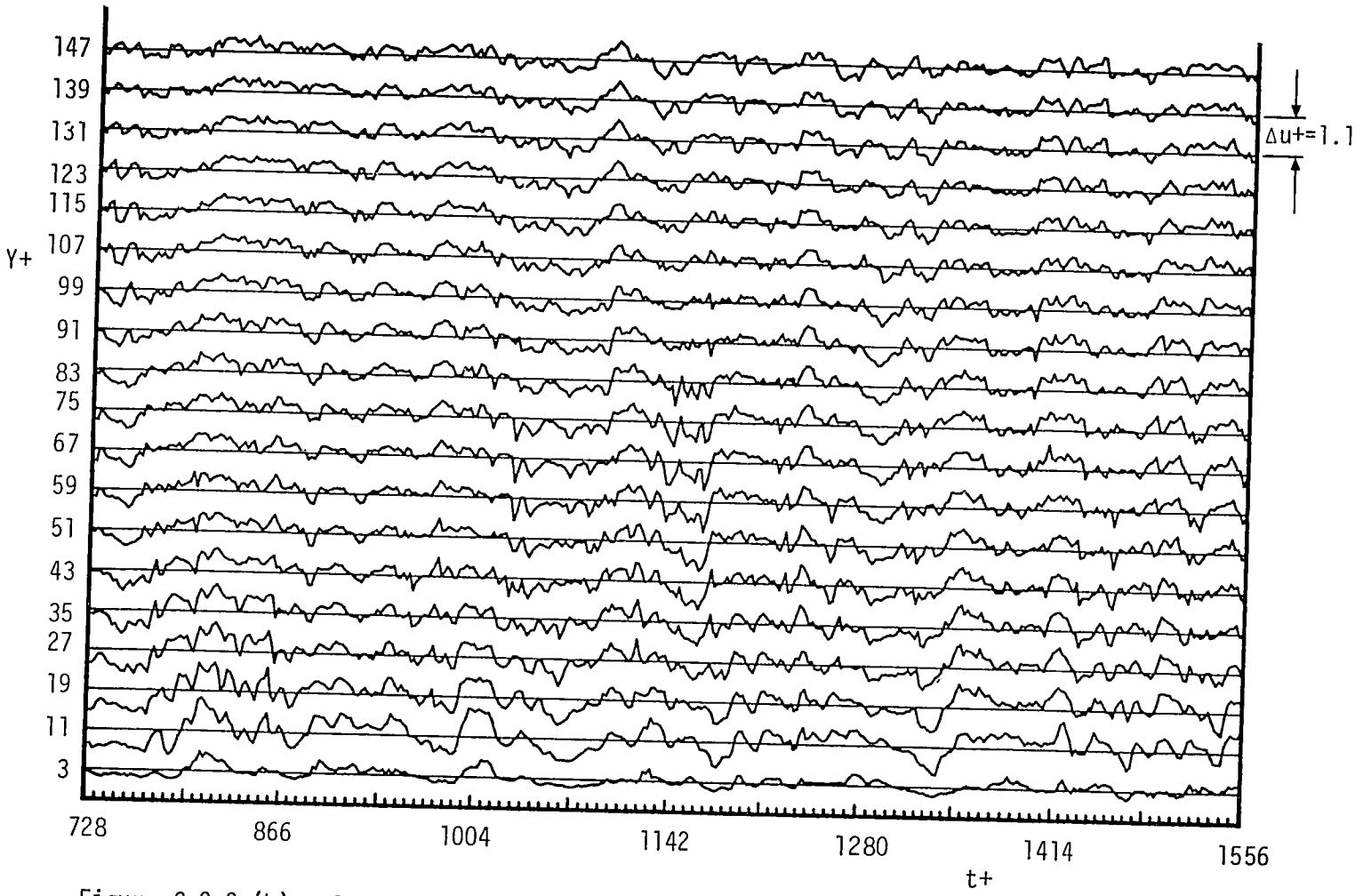

Figure C.2.2.(b). Continued.

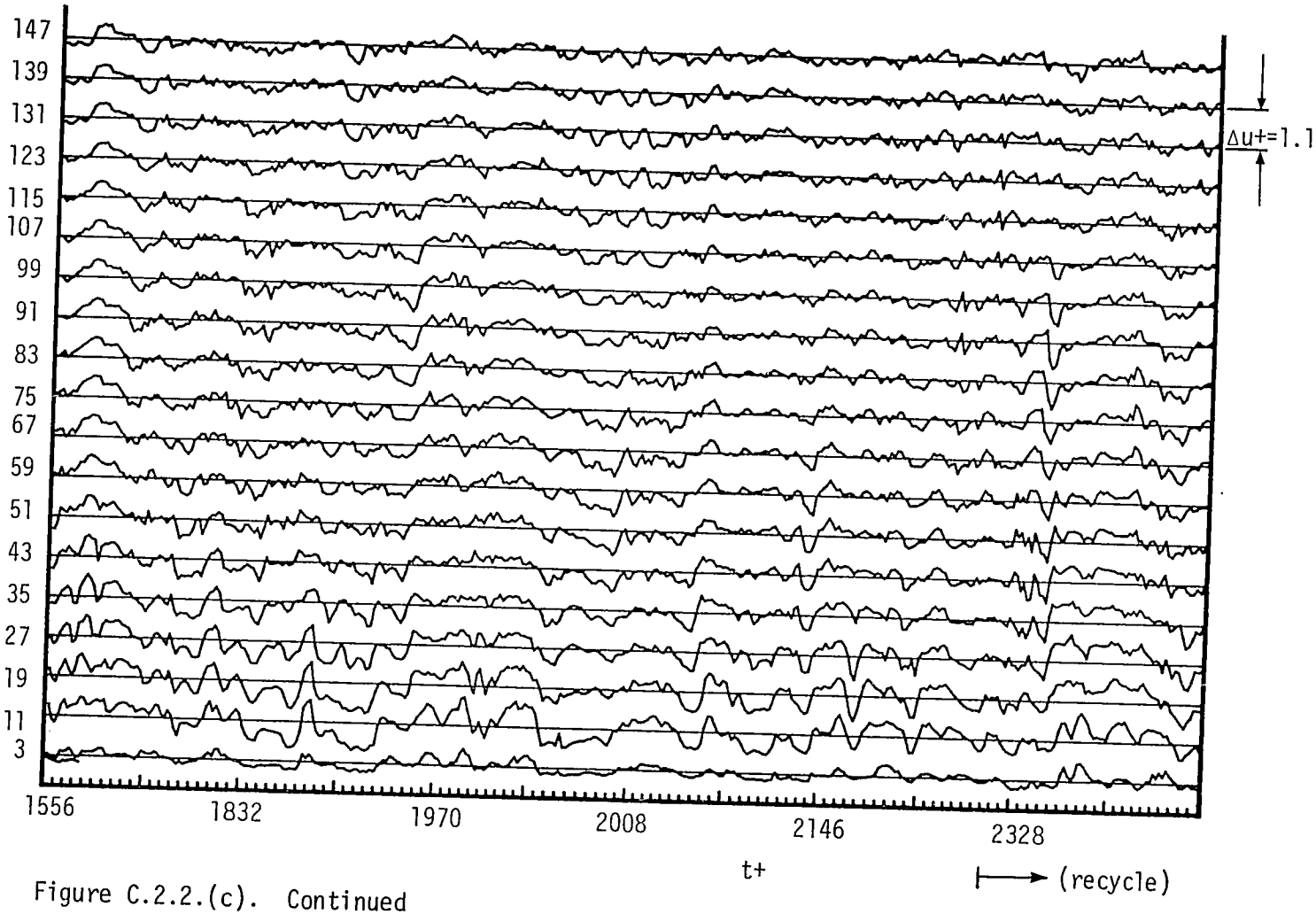

Figure C.2.2.(c). Continued

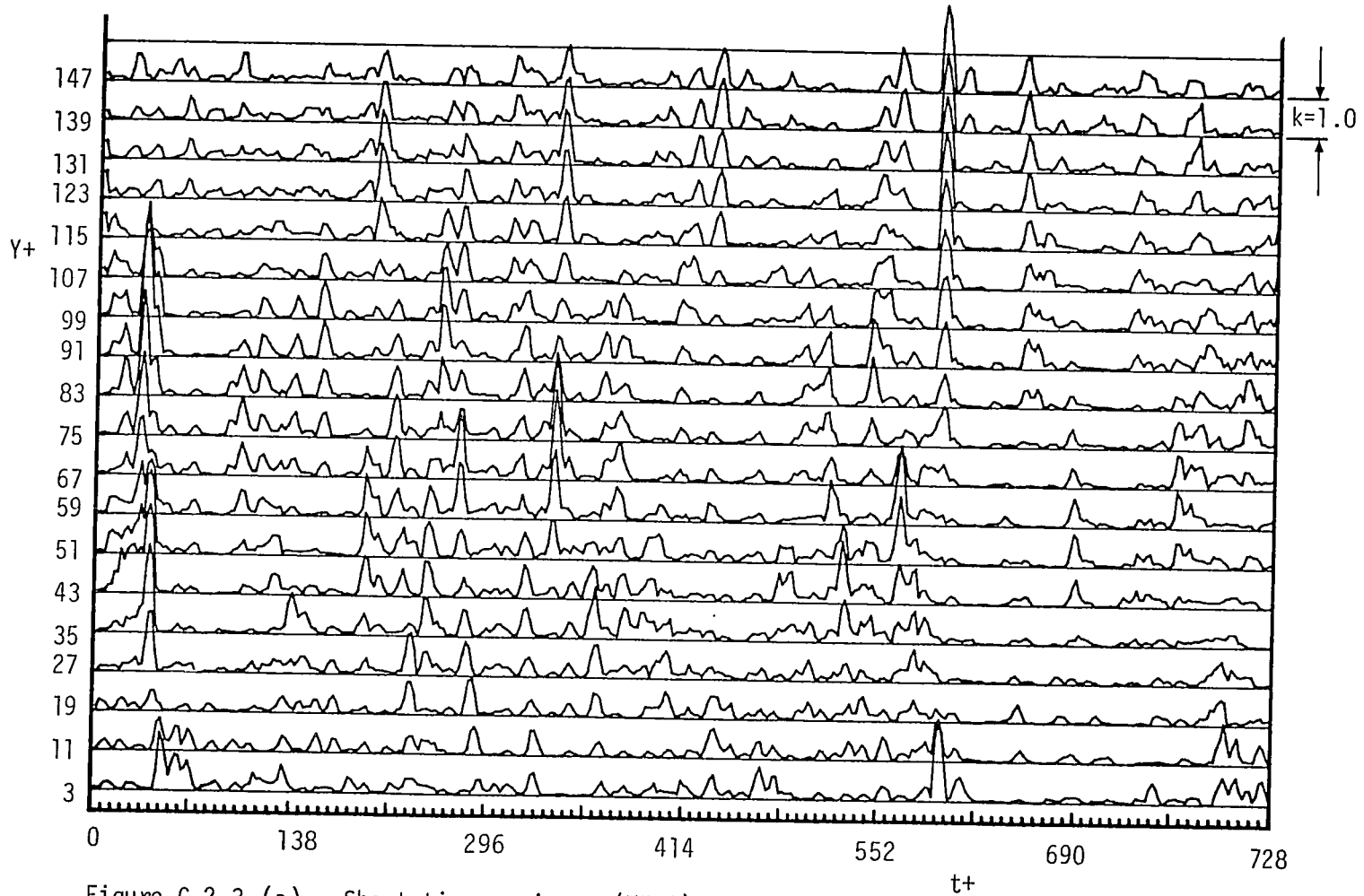

Figure C.2.3.(a). Short-time variance (VITA) of velocity signals shown in figure C.2.1.(a). Amplitude of curve represents $k=Var(t,T)/\overline{u'^2}$.

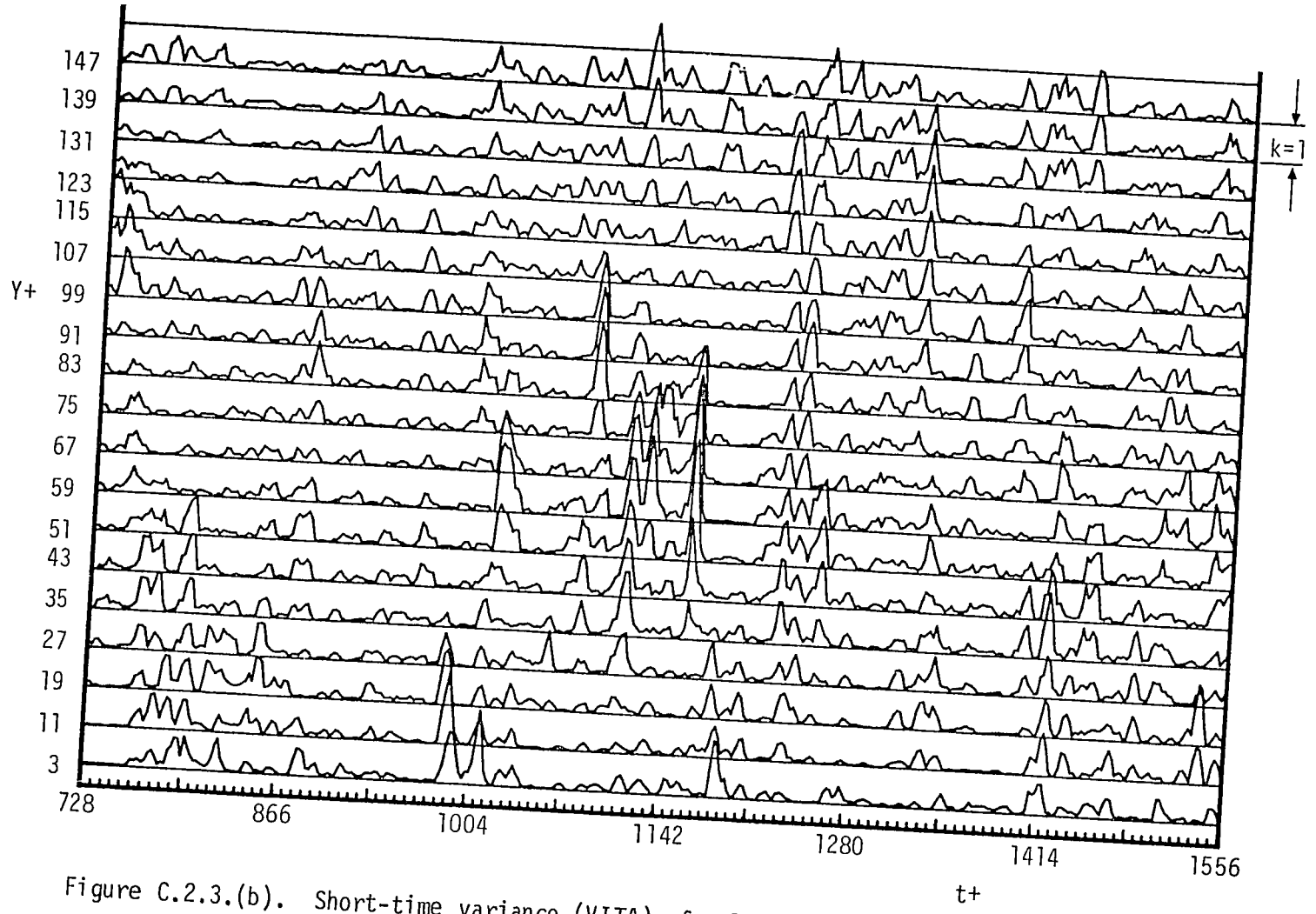

Figure C.2.3.(b). Short-time variance (VITA) of velocity signals shown in figure C.2.1.(b).

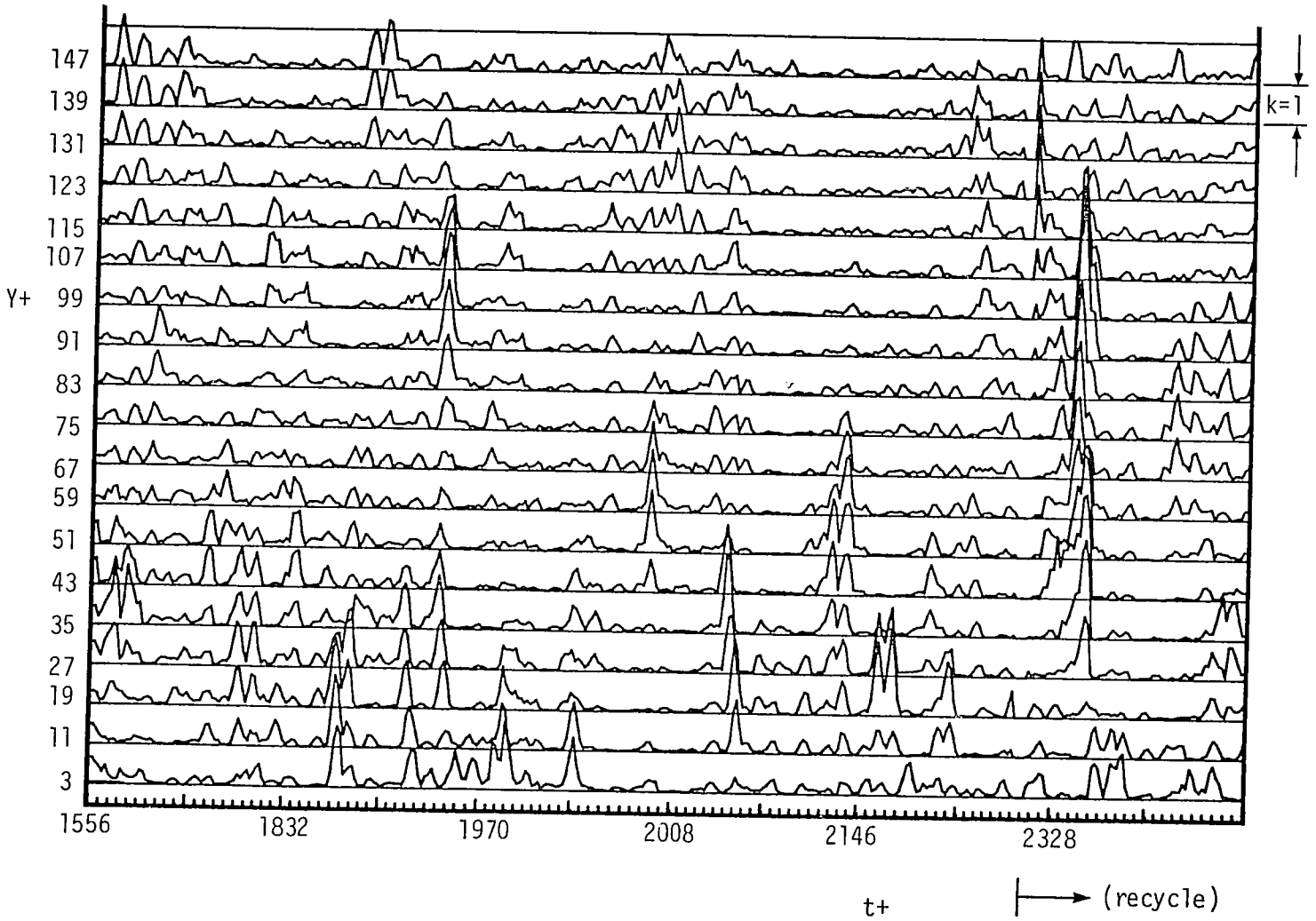

Figure C.2.3.(c). Short-time variance (VITA) of velocity signal shown in Figure C.2.1.(c).

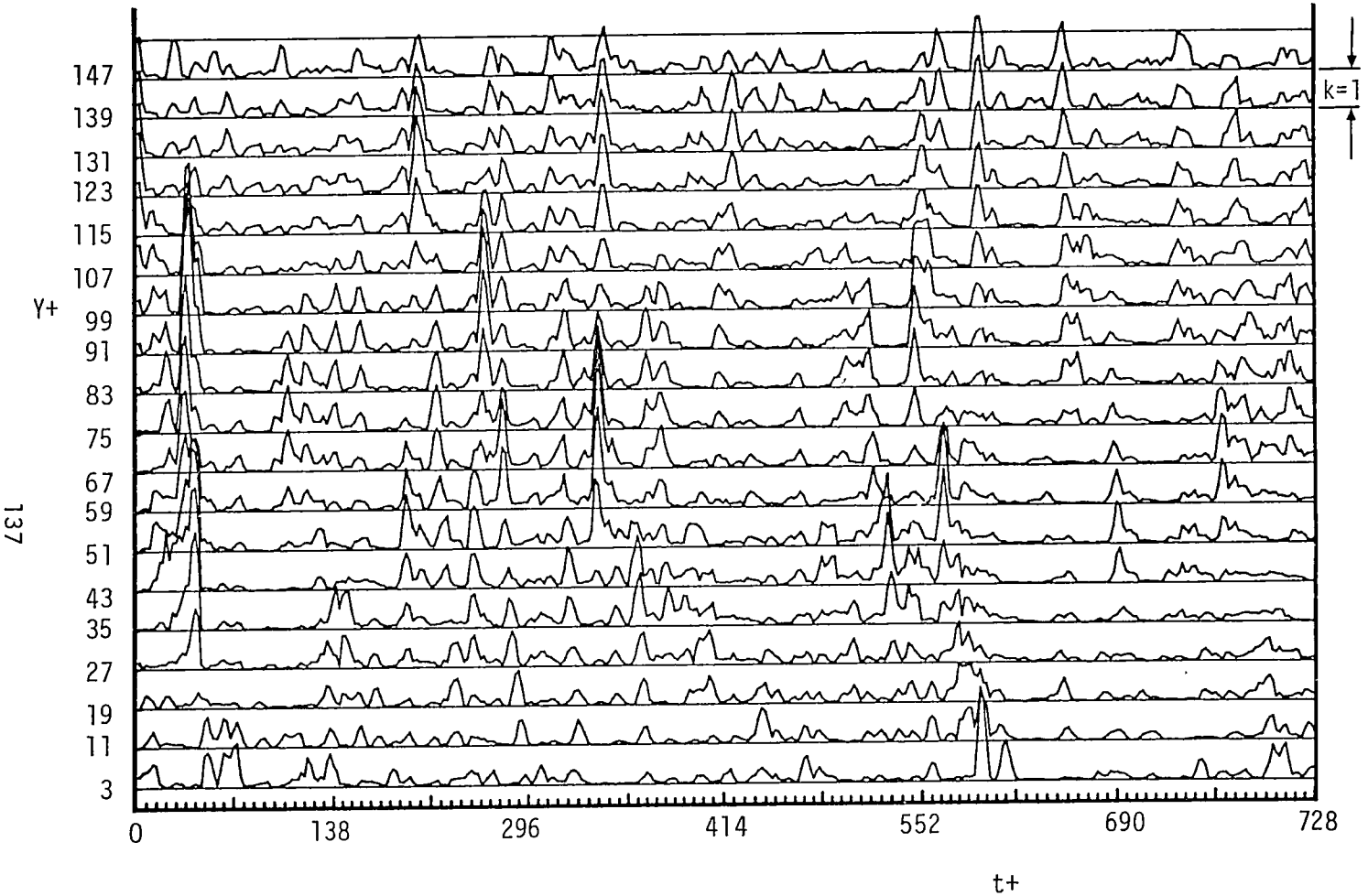

Figure C.2.4.(a). Short-time variance (VITA) of velocity signal shown in figure C.2.2.(a). Amplitude of curve represents $K=Var(t,T)/\overline{u'^2}$.

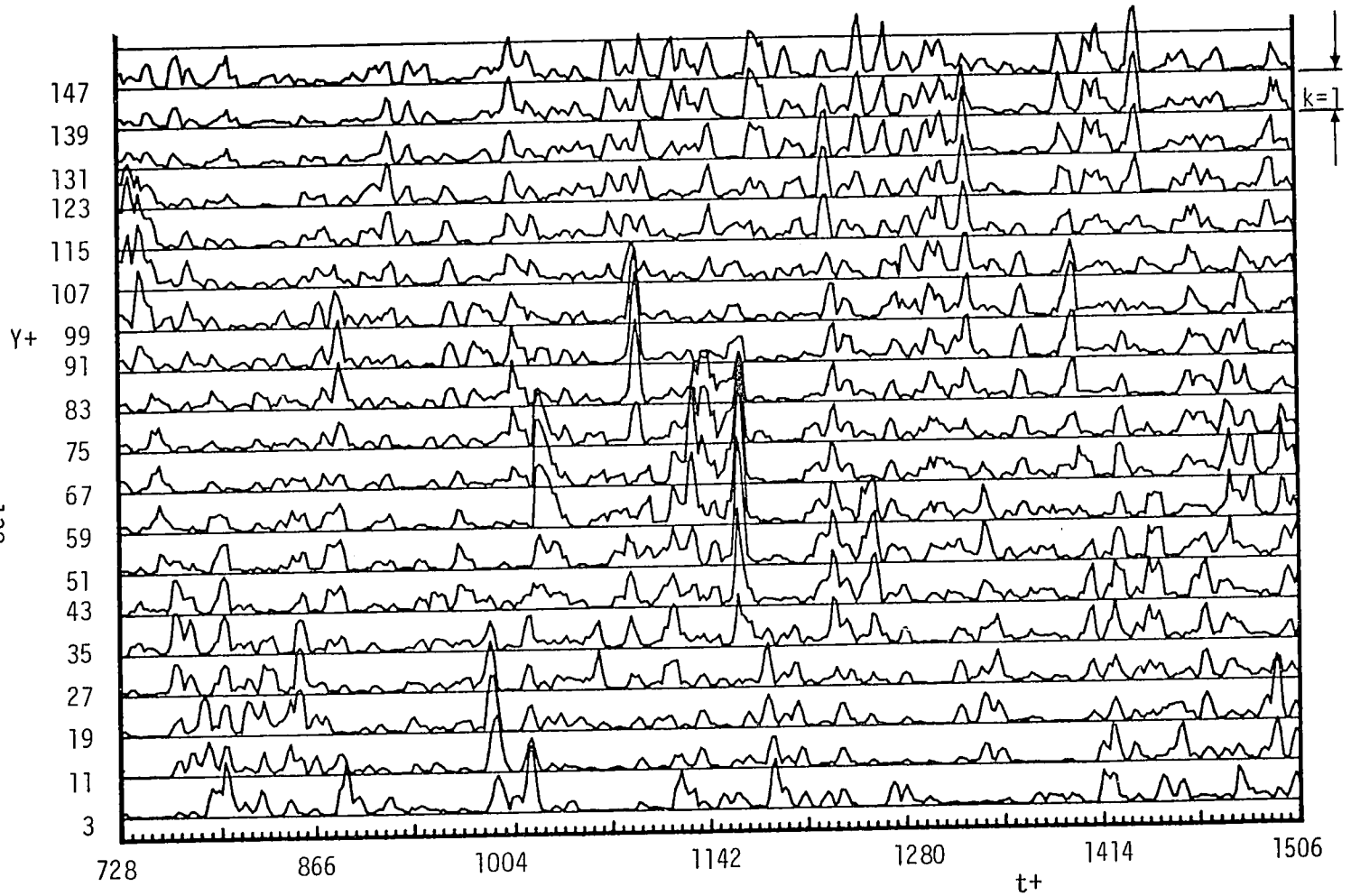

Figure C.2.4.(b). Short-time variance (VITA) of velocity signals shown in figure C.2.2.(b).

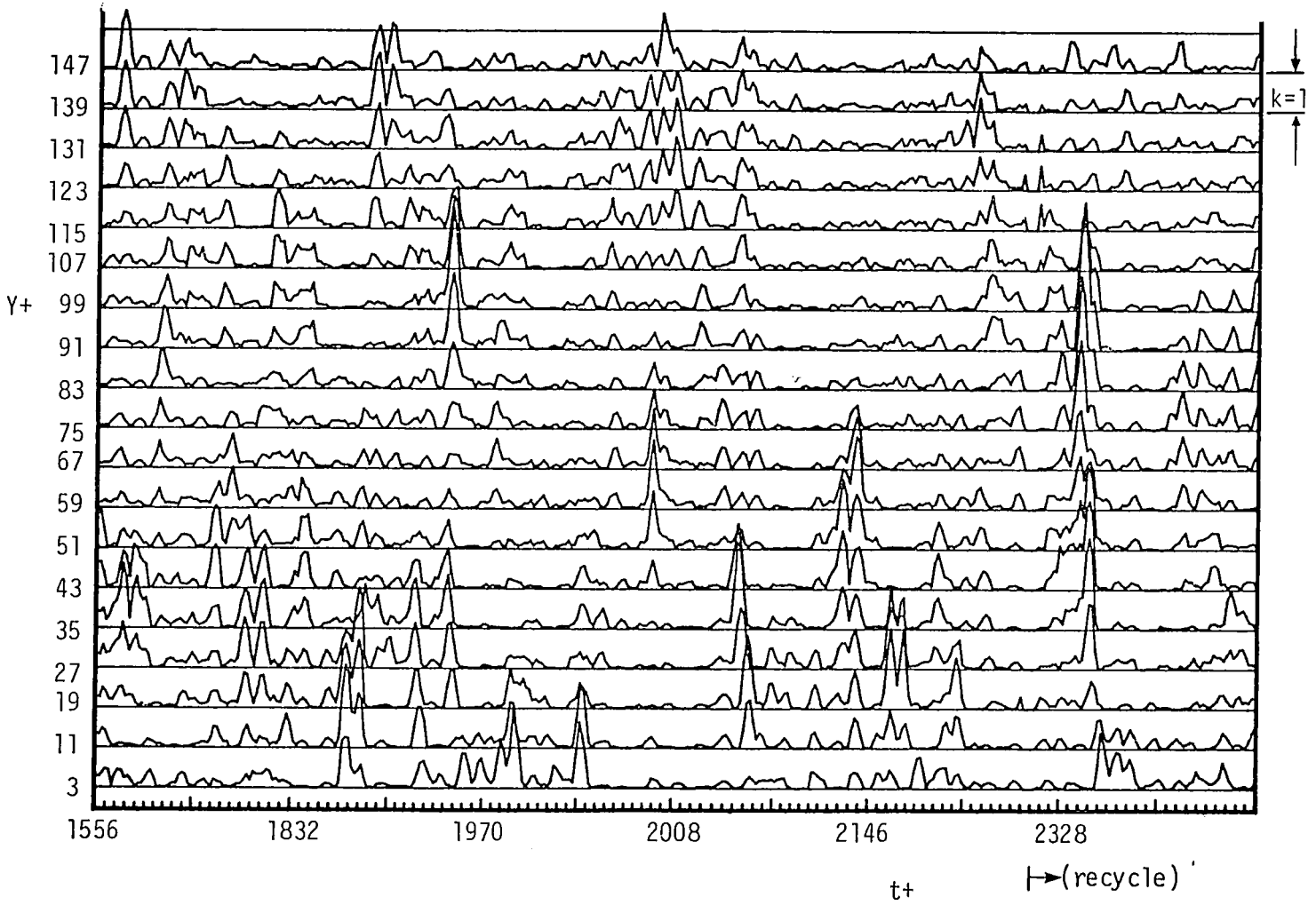

Figure C.2.4.(c). Short-time variance (VITA) of velocity signals shown in figure C.2.2.(c).

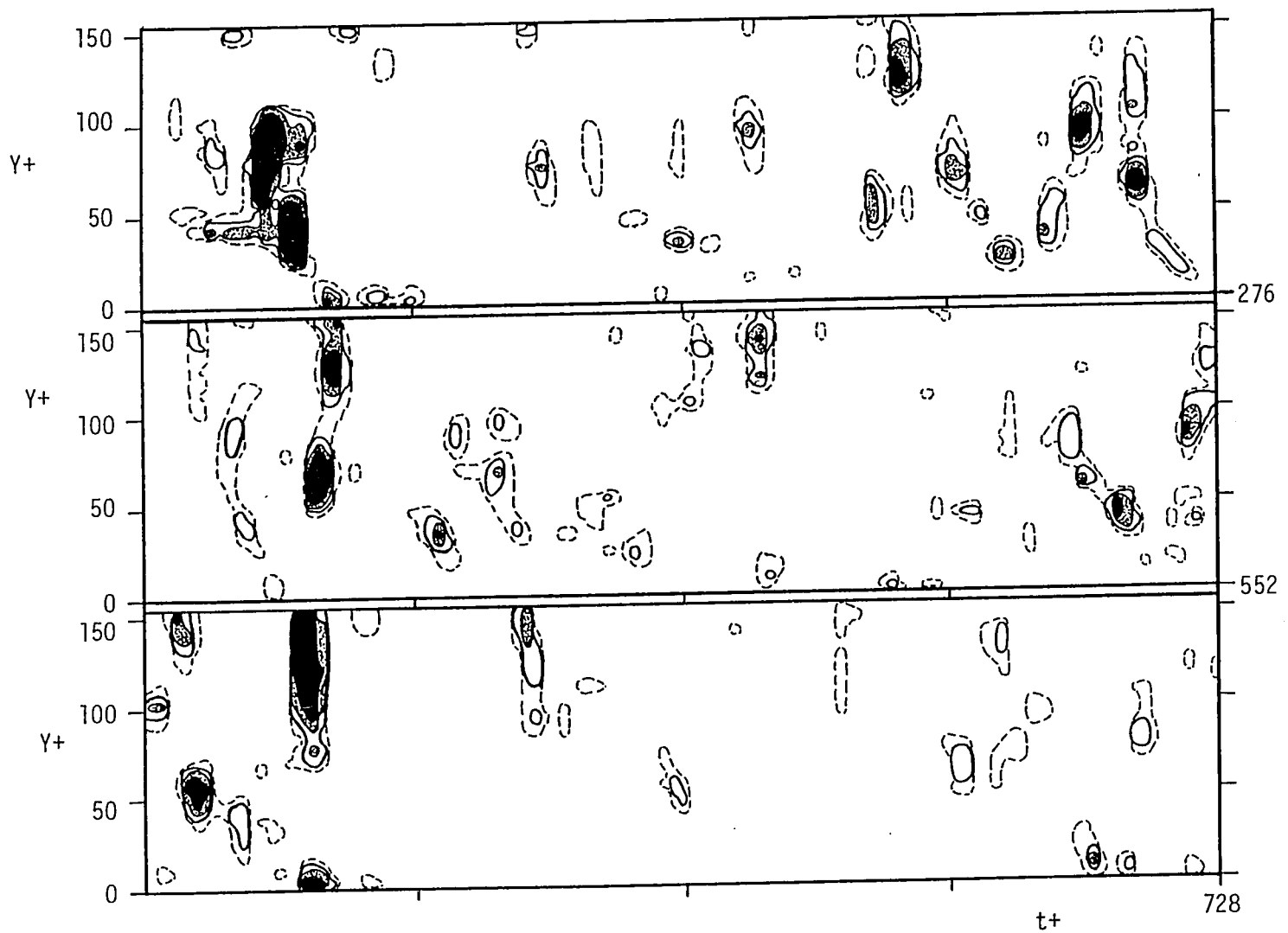

Figure C.3.1(a) Contours of K=Var(t,T)/$\overline{u'^2}$ for the first bubble-line data record, See legend, figure C.3.1(c).

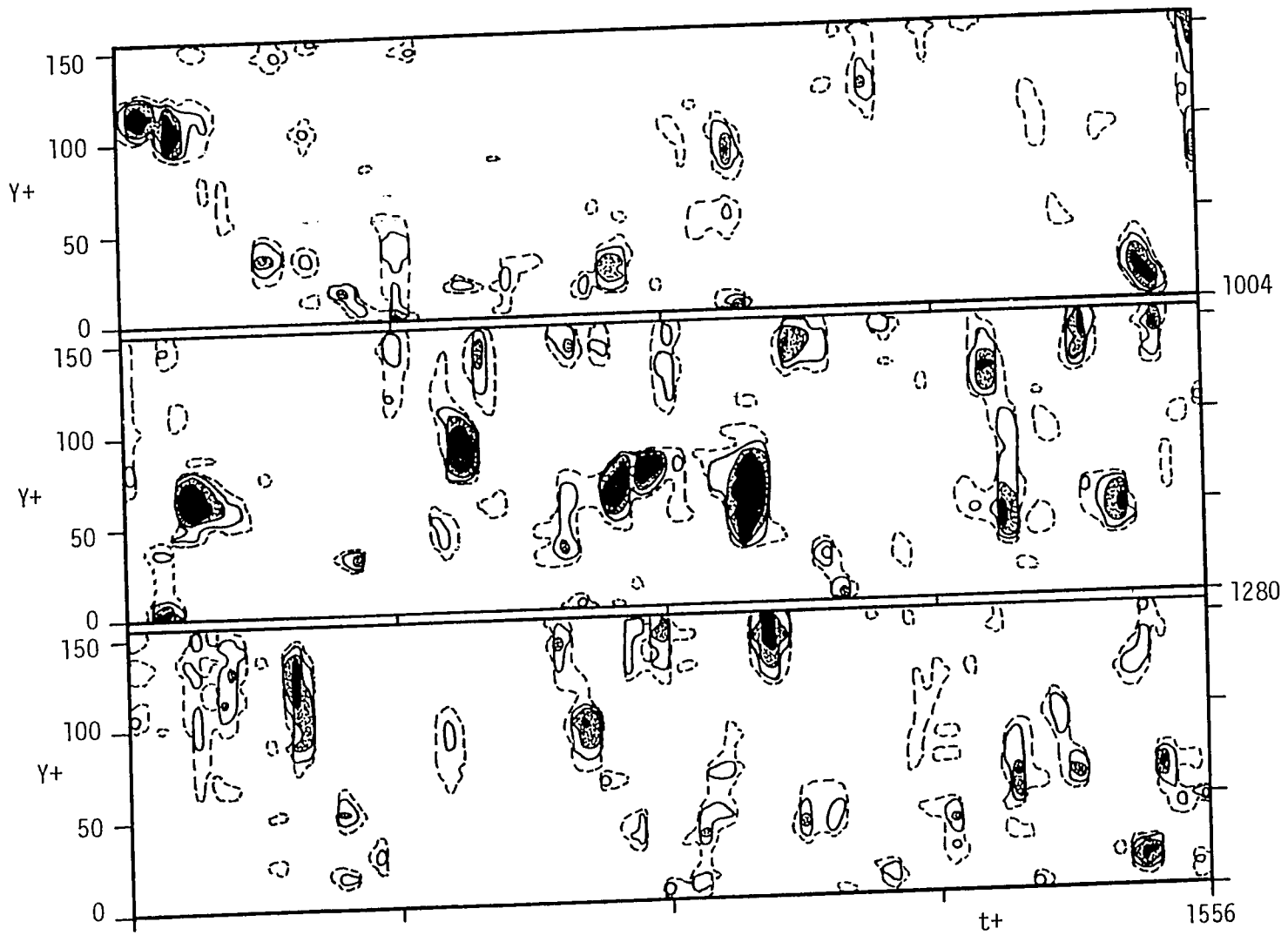

Figure C.3.1(b) Continued.

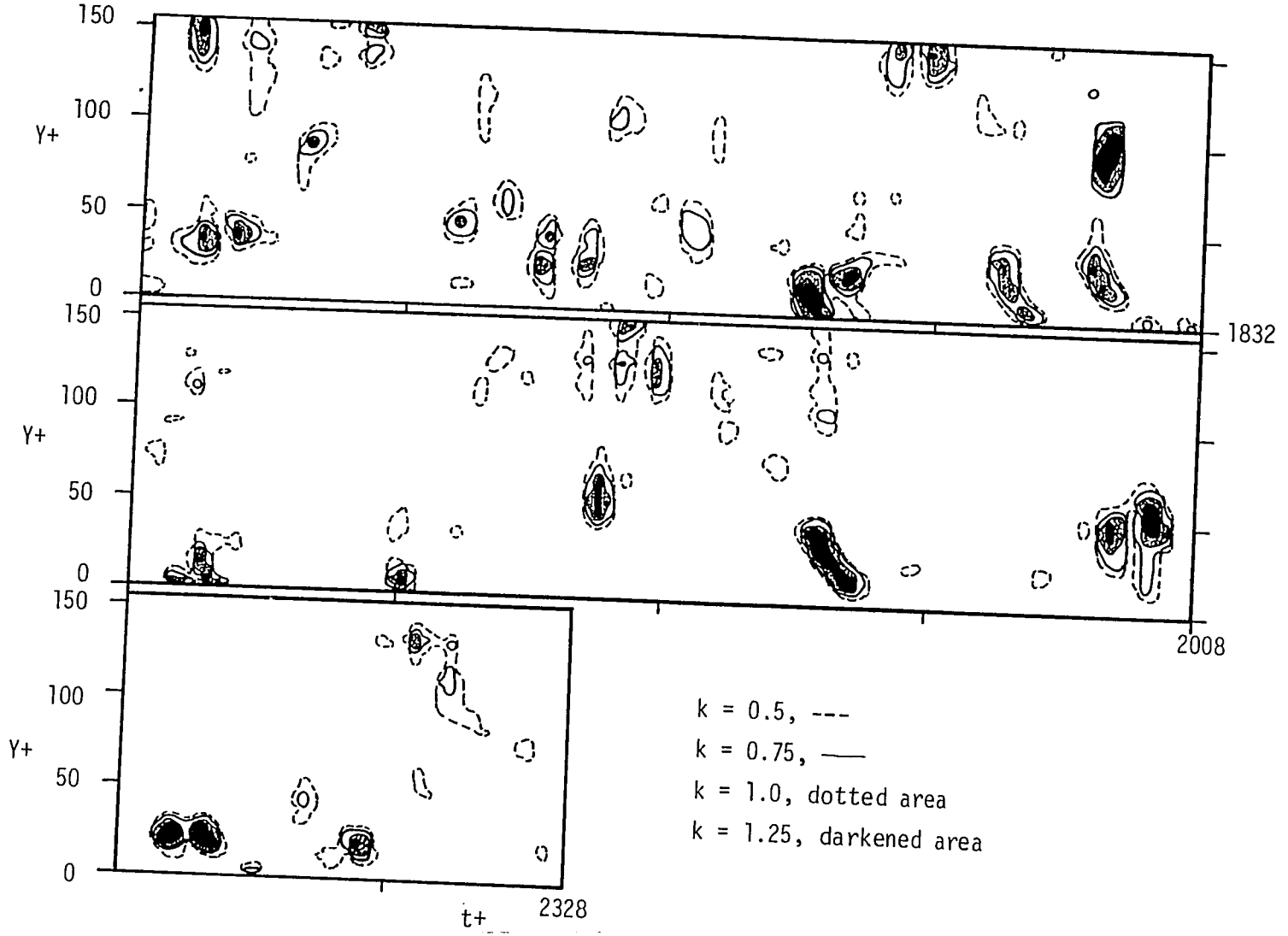

Figure C.3.1.(c) Continued.

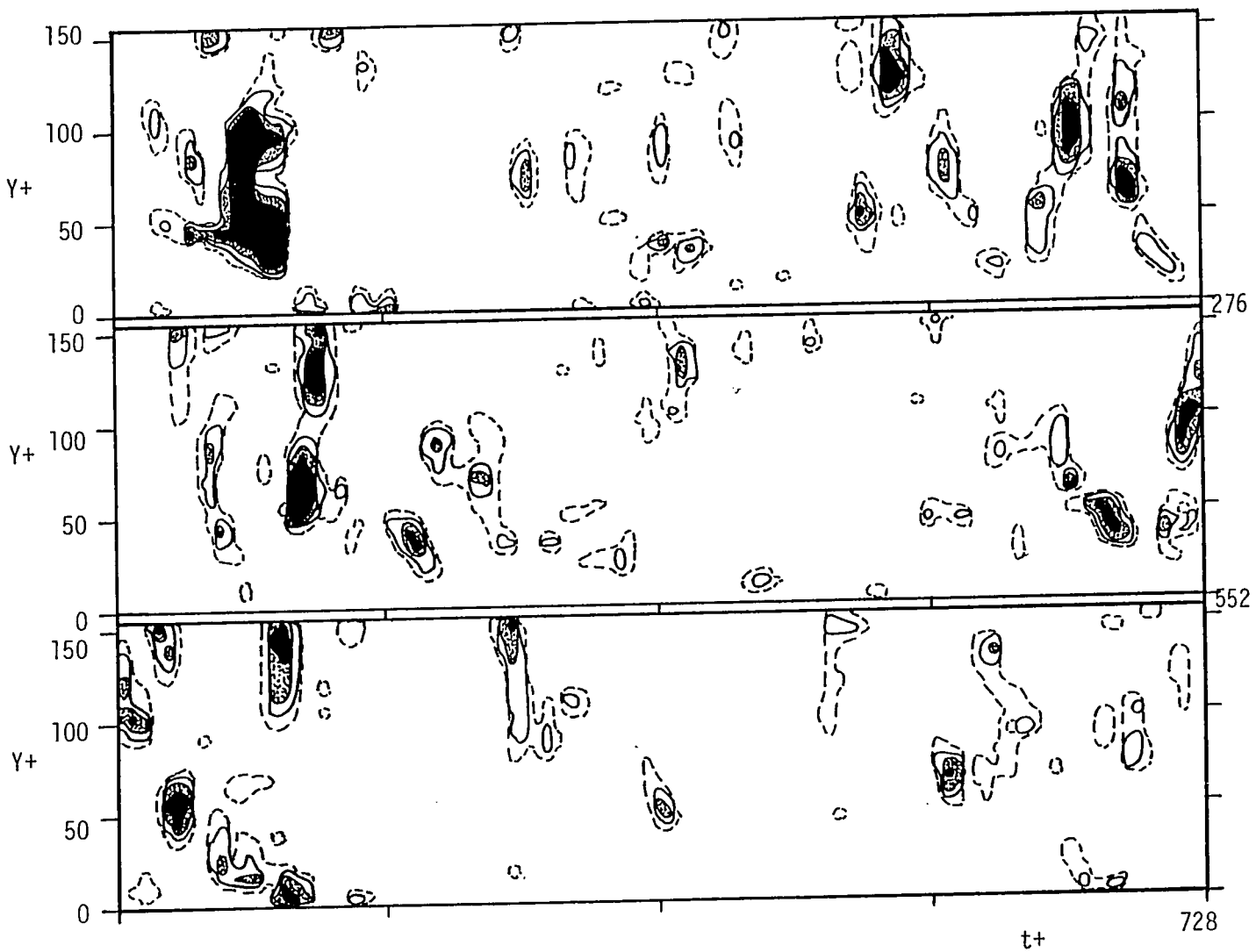

Figure C.3.2(a) Contours of $k=\mathrm{Var}(t,T)/\overline{u'^2}$ for the second bubble-line data record. See legend figure C.3.2(c).

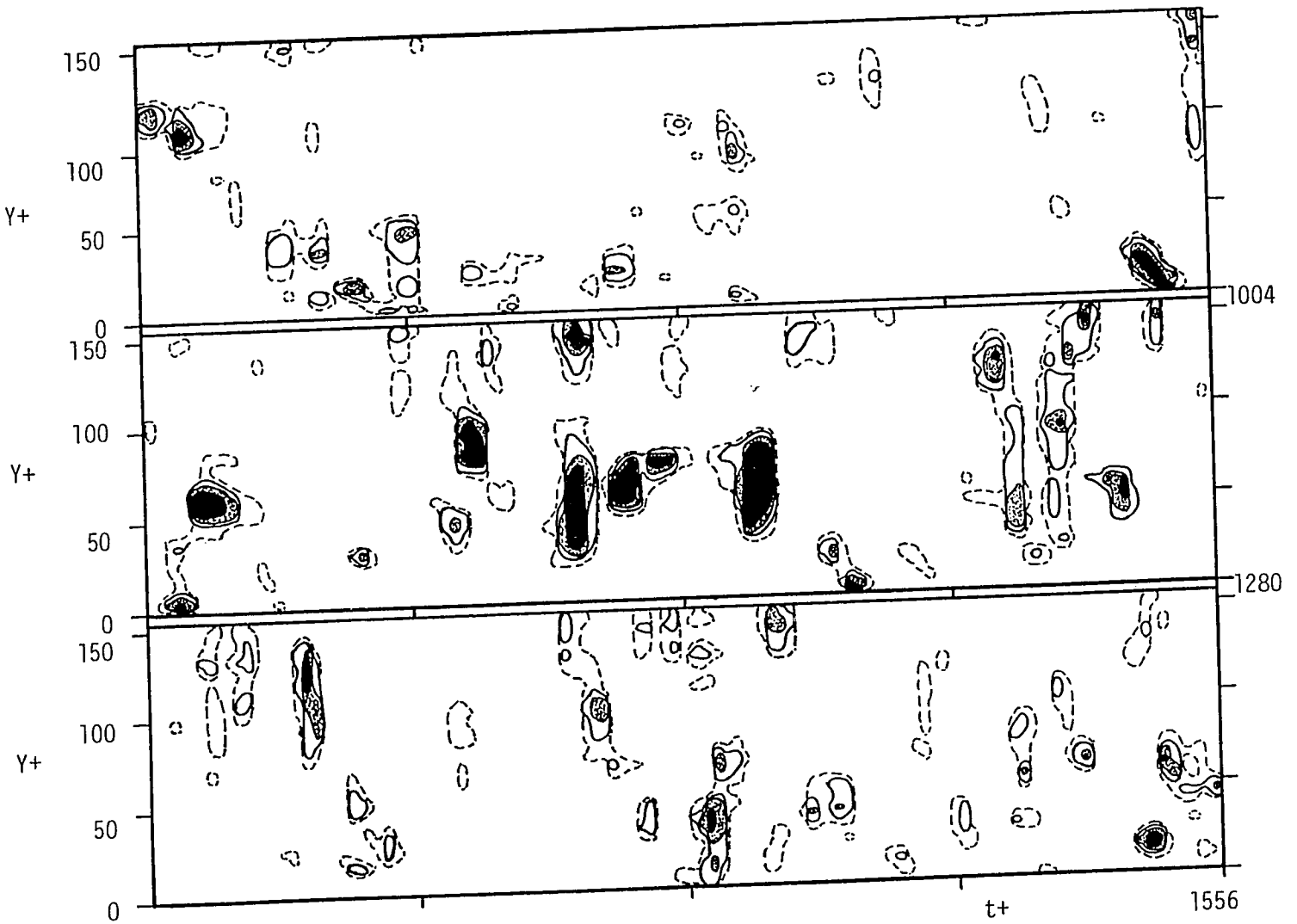

Figure C.3.2.(b) (Cont.)

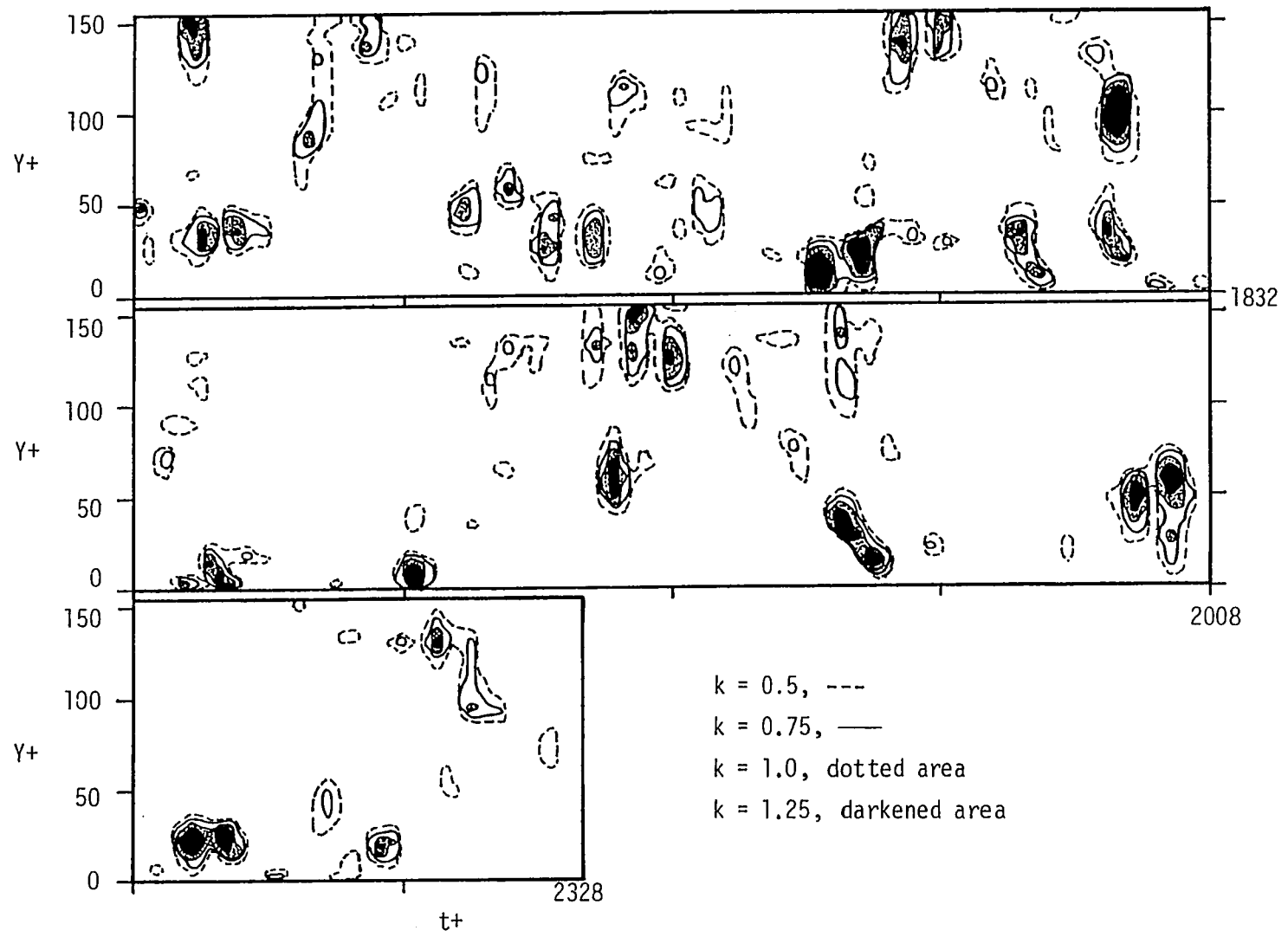

Figure C.3.2.(c) Cont.

VITA

Lih-Ju Lu was born in Tainan, Taiwan, Republic of China. She received a Bachelors degree in Mechanical Engineering from National Central University, Chung-Li, Taiwn, R.O.C.. In August of 1982, Lih-Ju enrolled as a graduate student at Lehigh University. In January of 1985, she passed the Ph.D. qualifying examination and is continuing her work with Dr. Smith in the field of turbulence and image processing at Lehigh University.